



A thesis submitted
in fulfilment of the requirements for the degree of
Doctor por Mondragon Unibertsitatea

**Optimization of superplastic forming
production of Al-5083-SPF parts via
finite element analysis**

NAGORE OTEGI MARTINEZ

Supervised by Lander Galdos

October 2012

Mechanical and Manufacturing Department

Mondragon Goi Eskola Politeknikoa

Mondragon Unibertsitatea

PREFACE

Declaration

I hereby declare that this thesis is the result of my own work and that, to the best of my knowledge and belief, no part of this dissertation has previously been submitted for any similar qualification or degree.

Nagore Otegi

(October 2012)

Copyright and reproduction

© 2012 Nagore Otegi

I authorize Mondragon Unibertsitatea to reproduce this thesis, in part or in whole, at the request of other institutions or individuals for the purpose of academic research.

Amari

ABSTRACT

For the aerospace industry, improving the fuel efficiency and emissions profile of aircraft is a major area of focus. Thereby, research is centred in the study and development of lightweight materials and in fabrication processes for obtaining parts with these materials.

Superplastic Forming (SPF) is a manufacturing process that takes advantage of certain materials' ability to undergo large strains before failure. Therefore, the main benefit associated with SPF is the capability of obtaining complex geometries with materials that have limited room and warm temperature formability. The relationship between materials testing and finite element modelling is a key to the development and optimisation of superplastic forming (SPF) processes.

Numerical models provide solutions for exploiting the maximum superplastic capabilities of the material. Therefore, an important aspect of such models is the development of constitutive equations that accurately represent the materials superplastic behaviour. Inaccurate prediction of the material path may result in premature fracture of the sheet or suboptimal exploitation of the superplastic capabilities of the material. The following dissertation studies the Al-5083-SPF aluminium alloy's mechanical behaviour at superplastic state and proposes a strategy to optimize the SPF production of this alloy.

In the first part of this research work, the mechanical behaviour of the Al-5083-SPF is characterized using uniaxial tensile tests, likewise some microstructural behaviour i.e. grain size and cavitation evolution is identified too. These tests' mechanical and microstructural data is used as reference for the constitutive equations parameter identification. This identification is by using an inverse engineering technique.

In the second section of this work, a finite element implementation of the identified constitutive equations is developed in Abaqus Standard to predict the pressure-time curves that should be used in the experimental SPF. Similarly, a new strategy for process time optimization is presented using the aforementioned constitutive equation as reference.

Finally, SPF experiments are conducted for two different geometries in SPF prototype developed during this research work. Comparing the numerical and experimental results, the

numerical model is validated for different material states. In addition, the new strategy presented in this work is successfully used for forming a semi industrial geometrical part reducing the process time.

LABURPENA

Aeronautika industrian, eraginkortasun energetikoa eta hegazkinen CP₂ isurtzea ikerketa munduko puntu garrantzitsu bilakatzen ari dira. Horregatik, ikerketa material arinen erabilpen eta garapenean zentratu da, baita material hauek erabilia pieza lortzeko behar diren prozesuetan.

Konformaketa Superplastikoa (*Superplastic forming* edo SPF) fabrikazio prozesu berezia da, eta zenbait materialek deformazio handiak jasateko duten gaitasuna erabiltzen du. Hala ere, material hauek egoera egokian deformatu behar dira, temperatura altuan eta deformazio-abiadura baxuan alegia. Konformaketa Superplastikoarekin lotu daitekeen onura nagusia, geometria konplexuak lortzea da. Prozesu honek, ordea, baditu hainbat desabantaila deformazio-abiadura baxuei lotuak, izan ere, gainontzeko konformaketa prozesu tradizionalekin konparatuta, ekoizpen-denbora altuak behar dira. Beste desabantaila bat material superplastiko batzuek jasaten duten kabitazio efektua da, materialaren propietate mekanikoak murrizten ditu eta. Prozesuaren muga hauei aurre egiteko, zenbakizko erremintak erabili ohi dira, materialen propietate superplastikoen erabilera maximoa egiteko behar diren prozesu-parametroak lortzeko, hau da, presio-denbora kurbak. Baina zenbakizko erreminta hauek ez dira erabilgarriak materialaren portaera deskribatzen duten ekuazio fidagarririk gabe. Presio-denbora kurben aurreikuspen okerra egin ezkerro, materialaren ahalmen superplastikoen aprobetxamendu eza edota hauste goiztiarra gerta daiteke. Dokumentu honetan, Al-5083-SPF aluminio aleazioaren portaera mekanikoa aztertuko da eta prozesu optimizazio estrategia berri bat proposatuko da.

Lan honen lehengo zatian, Al-5083-SPF aleazioaren portaera mekanikoa karakterizatu da entsegu uniaxialak erabilia. Gainera, portaera mikroestruturala ere karakterizatu da, ale tamaina eta kabitazioaren bilakaera definituz. Datu hauek erreferentzia bezala erabili dira ekuazio konstitutiboan parametroak identifikatzeko. Identifikazio hau egiteko alderantzizko ingeniari teknika erabili da.

Bigarren zatian, elementu finitu bidezko inplementazioa egin da Abaqus Standard softwarea erabiliz presio-denbora kurben aurreikuspen zehatza egiteko. Gainera, aurretik aipaturiko ekuazio konstitutiboak erabilia garatzen den optimizazio estrategia aurkeztu da.

Azkenik, esperimentuak egin dira konformaketa superplastiko erabilia bi geometria ezberdinentzako, lan honekin batera diseinatu eta ekoizturiko SPF prototipo bat erabiliz. Datu esperimental eta zenbakizkoak konparaturik modelo numerikoa balioztatu da, zenbait material egoera kontuan harturik. Beste alde batetik, lan honetan aurkezturiko estrategia berria erabiliz pieza semi industrialak ekoiztu dira prozesu denbora gutxituz.

RESUMEN

La eficiencia energética se está convirtiendo en uno de los aspectos más importantes de mejora, para la industria aeroespacial. Por ello, la investigación se ha encaminado principalmente hacia el uso y desarrollo de materiales ligeros así como de procesos de transformación, con el fin de obtener piezas de estos materiales.

El conformado superplástico (SPF) es un proceso de fabricación que utiliza la capacidad que tienen ciertos materiales de sufrir grandes deformaciones antes de llegar a fallo. Por ello, el mayor beneficio relacionado con el conformado superplástico es la capacidad de obtener piezas complejas, con materiales que exhiben una conformabilidad muy limitada a temperatura ambiente o templada. La relación entre los ensayos de material y el modelizado por elementos finitos, es clave a la hora de desarrollar y optimizar procesos de conformado superplástico. Los modelos numéricos ayudan a utilizar al máximo la capacidad de las propiedades superplásticas de los materiales. Por ello, uno de los aspectos más importantes de estos modelos, es el desarrollo de ecuaciones constitutivas que representen de forma fiel el comportamiento mecánico de las aleaciones. Una predicción imprecisa puede resultar en la fractura prematura del material o en su explotación no óptima. El siguiente documento estudia el comportamiento mecánico de la aleación de aluminio Al-5083-SPF en estado superplástico y propone una estrategia de optimización para conformar piezas, mejorando el tiempo de proceso.

En la primera parte de este trabajo de investigación, el comportamiento mecánico del Al-5083-SPF es caracterizado, utilizando ensayos uniaxiales. Además se analiza la microestructura modificada por este comportamiento mecánico. Los datos mecánicos y microestructurales obtenidos mediante estos ensayos, son utilizados para identificar los parámetros de las ecuaciones constitutivas anteriormente mencionadas.

En la segunda parte de este trabajo, la implementación de las ecuaciones constitutivas en el programa de elementos finitos Abaqus Standard es llevada a cabo para predecir las curvas de presión-tiempo necesarias para alimentar el proceso SPF. Asimismo se presenta una nueva estrategia de optimización del tiempo de proceso, basada en las ecuaciones constitutivas mencionadas anteriormente.

Finalmente, se realizan experimentos de conformado superplástico para dos geometrías diferentes. Comparando los resultados experimentales y numéricos, el modelo numérico es validado para diferentes estados de material. Además, la nueva estrategia planteada en este trabajo, es utilizada con éxito para conformar una geometría semi-industrial, reduciendo su tiempo de proceso.

*“Education is an admirable thing,
but it is well to remember from time to time that
nothing that is worth knowing can be taught”*

Oscar Wilde

ACKNOWLEDGMENTS

Lehenik eta behin, lan hau aurrera eramateko ezinbestekoa izan den nire tesi zuzendariari, Lander Galdosi, eskerrak eman nahi nizkioke. Batik bat hamaika gauzarekin ibilita ere, eskainitako gidaritza eta lanerako gogoagatik, eskerrik asko. Baita ere konformaketa supeplastikoaren ikerkuntzari bultzada ematen saiatzeagatik, ni unibertsitatetik banoan momentu honetan.

I would like to thank Sean Leen, who accepted a PhD student from a university that hardly had knowledge about superplasticity and superplastic forming. I will be always grateful for his help, as he was a great advisor and teach me a lot about this fascinating process.

Asimismo, quisiera dar las gracias a Koldo Ostolaza e Iker Unanue de ITP, gracias a quienes empezamos a trabajar en este campo y tuve una beca asociada a la misma empresa. Especialmente quiero dar las gracias a David Serra, quien me ayudó en incontables ocasiones cuando diseñaba el prototipo SPF (aun cuando no tenía por qué hacerlo), y siempre ha sido un gran apoyo en congresos y conferencias varias.

Eskerrak eman nahi dizkiet ere konformadoko ikerketa taldeari, Rafa, Iñaki eta Enekor bereziki nire lanari egin dizkieten ekarpenengatik. Baita bost urte hauetan nirekin lan egin duten Oier eta Matori.

Azkenik, eskerrak ere doktoradutza egiten igarotako urte hauetan ezagutu ditudan lagun eta lankide guztiei. Pasa ditugun momentu, janari eta kafe guztietan izandako une on, barre, euro eta elkarrizketengatik. Eskerrik asko Haritz, Jokin, Javi, Alaitz, Ione, Joanes, Alain, David, Miriam, Ireneo, Nuria, Jon, Kintana, Ainara, Manex, Iñigo, Iosu, Erik, Elena eta 3115 gelako beste lankideei, batez ere jasan duzuenagatik.

CONTENT

PREFACE	III
ABSTRACT	VII
LABURPENA	IX
RESUMEN	XI
ACKNOWLEDGMENTS	XV
CONTENT	XVII
LIST OF FIGURES	XXIII
LIST OF TABLES	XXIX
NOMENCLATURE	XXXI
Symbols	xxxI
Abbreviations	xxxii
1 INTRODUCTION	1
1.1 Motivation and background	1
1.2 Scope of the present thesis	3
2 SUPERPLASICITY AND SUPERPLASTIC FORMING	5
2.1 Introduction	6
2.2 Superplasticity	6

2.2.1	History	6
2.2.2	Requirements for Superplasticity	8
2.3	Physical mechanism of superplasticity	9
2.3.1	Grain boundary sliding	9
2.3.2	Accommodation mechanisms	10
2.3.3	Grain growth	10
2.3.4	Cavity formation	11
2.4	Mechanical behaviour of superplastic materials	13
2.4.1	Physical material constitutive equations	15
2.4.2	Mechanical material constitutive equations.....	16
2.5	Superplastic materials in industry	17
2.5.1	Aluminium-based materials.....	18
2.5.2	Titanium-based alloys	19
2.5.3	Production of superplastic materials.....	19
2.6	Superplastic forming technique variants	20
2.6.1	Current Applications of SPF.....	23
2.7	Finite element method in SPF	25
2.7.1	Optimization of SPF via FEM.....	26
2.8	Closure	28
3	SPF MATERIAL CHARACTERIZATION	29
3.1	Introduction	30
3.2	Uniaxial tensile test methodology	30
3.2.1	Tested material	31
3.2.2	Tensile test procedures.....	31
3.2.3	Specimen and clamps geometry	35
3.2.4	Heating of the specimens.....	36
3.3	Post -tensile test characterization methodology	38
3.3.1	Geometrical measurement of the strain values	38
3.3.2	Grain size measurement	40
3.3.3	Void area fraction measurement.....	41
3.4	Tensile test results	41
3.4.1	Controlled strain rate tests	41

3.4.2	Jump tests.....	43
3.4.3	Interrupted tests.....	44
3.5	Closure	50
4	CONSTITUTIVE MODELLING OF SPF MATERIALS	53
4.1	Introduction	54
4.2	Viscoplasticity model	54
4.2.1	Viscoplastic model for matrix material.....	55
4.2.2	Mechanism based constitutive equation	55
4.2.3	Damage mechanics.....	56
4.2.4	Viscoplastic model for voided material with fixed density	61
4.2.5	Viscoplastic model for voided material with density variation	62
4.3	Uniaxial model fitting	65
4.3.1	Inverse method development for stress – strain curve fitting.....	65
4.3.2	Initial parameter determination.....	66
4.3.3	Viscoplastic model for voided material with density variation parameter determination.....	71
4.4	Closure	75
5	SPF NUMERICAL MODEL IMPLEMENTATION.....	77
5.1	Introduction	78
5.2	Mechanical analysis.....	78
5.3	Body discretization.....	79
5.3.1	Sheet mesh.....	80
5.3.2	Die mesh.....	81
5.3.3	Fluid mesh	81
5.4	Contact and friction.....	82
5.5	Material model implementation	83
5.5.1	Cavitation volume growth and triaxiality dependence	84
5.6	Loading and pressure curves	85
5.6.1	Control strategy	85
5.6.2	Target integration point number selection	87

5.6.3	New approach: m max strategy by material constitutive equation.....	87
5.6.4	Implementatin of control strategies into abaqus.....	90
5.6.5	Implementation of the backpressure into Abaqus.....	91
5.7	General results	93
5.7.1	Backpressure effect.....	93
5.7.2	Simulation control approaches effect.....	94
5.8	Closure	104
6	SPF EXPERIMENTAL TESTS	105
6.1	Introduction	106
6.2	SPF facility	106
6.2.1	Specifications of the facility.....	106
6.2.2	Design of a superplastic forming prototype.....	107
6.2.3	Design and manufacture of a die for superplastic forming.....	110
6.3	Gas forming test methodology	111
6.4	Material model validation by bulge-test s	113
6.4.1	Dome pole height.....	113
6.4.2	Dome pole thickness.....	116
6.4.3	Cavitation behaviour.....	118
6.4.4	Grain size behaviour.....	120
6.4.5	Simulation results: strain rate of the experiments.....	122
6.5	New strategy validation	123
6.5.1	Experimental results of toroid-shape part.....	123
6.5.2	Numerical results and comparison with experimental data.....	126
6.6	Closure	129
7	CONCLUSION AND FUTURE WORK	131
6.7	Conclusions	131
6.8	Future work	133
APPENDIX A	135
International journals	135

International congresses	135
National congresses	136
REFERENCES.....	137

LIST OF FIGURES

<i>Figure 1.1.: Historical evolution of the publication number related to Superplastic Forming (source: Web of Knowledge).</i>	2
<i>Figure 1.2.: Summarized structure of the information presented in this document.</i>	4
<i>Figure 2.1.: Tensile specimens in superplastic state for polycrystalline materials: (a) Pearson’s famous test of a Bi-Sn alloy that undergone 1950 % [Pea34] and Kim et al. tests for superplastic ceramics [Kim01].</i>	7
<i>Figure 2.2.: The first published superplastically formed bubble [Bac64].</i>	8
<i>Figure 2.3.: 2D section of the 5083 aluminium alloy strained up to $\epsilon = 1.65$. The cavities in white are in fact connected in 3D [Sal03].</i>	13
<i>Figure 2.4.: A typical sigmoidal-shaped logarithmic stress/strain rate curve (a) and the corresponding bell-shaped sensitivity curve (b) for a superplastic material.</i>	14
<i>Figure 2.5.: Schematic view of Equal Channel Angular Pressing.</i>	20
<i>Figure 2.6.: Schematic of the superplastic simple female blow forming technique.</i>	20
<i>Figure 2.7.: Schematic of the superplastic male forming technique.</i>	21
<i>Figure 2.8.: Schematic of the superplastic diaphragm forming technique.</i>	21
<i>Figure 2.9.: Schematic of the superplastic blow forming technique with back pressure.</i>	22
<i>Figure 2.10.: Scheme of the pressure-time curve of the two channel of the superplastic blow forming technique with back pressure [Usp95].</i>	22
<i>Figure 2.11.: Superplastic forming used for aeroplane applications [Sup10] (a) Eclipse 500 Jet (b) Boeing 777 (c) Boeing 737 using Al5083 aluminium alloy.</i>	23
<i>Figure 2.12.: Superplastic forming used for automotive applications (a) Aston Martin Vanquish (b) Mercedes-Benz SLS AMG.</i>	24
<i>Figure 2.13.: Superplastic forming used for medical applications, superplastically formed part and the final palate [Cur01].</i>	24
<i>Figure 2.14.: Superplastic forming used for designing furniture [Ara12].</i>	25
<i>Figure 2.15.: Different pressure distribution profiles and pressure-time curves for three forming control strategies [Naz04].</i>	27
<i>Figure 3.1.: Example of a jump tests and the obtaining of the different stress values.</i>	34
<i>Figure 3.2.: Interrupted test for three different strain values at the same strain rate.</i>	34
<i>Figure 3.3.: Tensile specimen geometry used for the high temperature tensile tests.</i>	35

<i>Figure 3.4: Geometry of the clamps with the cavity for the insertion of the test specimen.</i>	36
<i>Figure 3.5: Specimens illustration before (a) and after (b) the tensile test and the measured lengths.</i>	40
<i>Figure 3.6: Superplastic elongation of Alnovi-1 alloy at different temperatures and strain rates.</i>	42
<i>Figure 3.7: Tensile force – displacement curves for various strain rates at 500 °C.</i>	43
<i>Figure 3.8: Specimens obtained at different controlled strain rates at 500 °C until fracture.</i>	43
<i>Figure 3.9: Tensile force – displacement curves for three different jump tests between 2×10^{-4}, 5×10^{-4}, 1×10^{-3} and $2 \times 10^{-3} \text{ s}^{-1}$ strain rates.</i>	44
<i>Figure 3.10: Comparison of the different strains. (a) measured longitudinal strain ϵ_m against cross-head longitudinal strain and (b) measured longitudinal strain ϵ_m against section strain ϵ_s.</i>	45
<i>Figure 3.11: Average grain size evolution obtained from micrographs of the interrupted tests for Al-5083-SPF.</i>	47
<i>Figure 3.12: Comparison of cavitation volume fraction and the section strain obtained from micrographs of the interrupted tests.</i>	49
<i>Figure 3.13.: Schematic representation of the final geometry of a superplastic alloy specimen after being stretched in a tensile test machine.</i>	50
<i>Figure 4.1.: Physical damage and mathematical continuous damage, modified from [Lem05].</i>	57
<i>Figure 4.2.: Representation of the volume change in a uniaxially tensiled RVE body that suffers from cavitation and the approximation of this damaged body using CDM.</i>	58
<i>Figure 4.3.: Void grow on grain boundary for GBS [Coc80].</i>	60
<i>Figure 4.4.: Basic chart flow of data and actions from the start of an iterative curve fitting.</i>	65
<i>Figure 4.5.: Average grain size evolution for different interrupted tensile tests and fitted model curves.</i>	67
<i>Figure 4.6.: Void area fraction evolution for different interrupted tensile tests and fitted model.</i>	68
<i>Figure 4.7.: “True” stress – “true” strain obtained in the traditional way and the fitted model curves for the initial parameter determination.</i>	69
<i>Figure 4.8.: Gauge section versus distance change between clamps for experimental data and initial model.</i>	69
<i>Figure 4.9.: Comparison between the curves obtained from the model using ideal situation and the simulated with the same equation parameters.</i>	70
<i>Figure 4.10.: Initial and formed simulated tensile test specimen geometries.</i>	70
<i>Figure 4.11.: Force – displacement experimental data versus simulated results for initial model parameters.</i>	71
<i>Figure 4.12.: True stress vs. true strain and viscoplastic strain rate values for simulated tensile tests for viscoplastic model for voided material with density variation equations.</i>	72

<i>Figure 4.13.: Simulated strain rate pattern for the gauge section of a quarter specimen at strain value of 0.3 and 0.9</i>	72
<i>Figure 4.14.: Force – displacement experimental data versus simulated results for iterated model parameters.</i>	73
<i>Figure 4.15.: Section area versus distance between clamps for model an experimental results.</i>	74
<i>Figure 4.16.: Constitutive model versus experimental data for average grain size and cavitation area fraction evolution.</i>	74
<i>Figure 4.17.: Strain rate values calculated theoretically and by inverse modelling.</i>	75
<i>Figure 5.1.: Mesh for tensile specimen representation with a clamp.</i>	79
<i>Figure 5.2.: Bulge-test model discretization with axisimetric element.</i>	80
<i>Figure 5.3.: Toroid-shape model discretization with axisimetric element.</i>	80
<i>Figure 5.4.: Fluid-filled cavity in a toroid shape geometry with the hydrostatic fluid elements nodes in blue and the cavity reference node in red.</i>	82
<i>Figure 5.5.: Curves at different triaxial states according to viscoplastic model for voided materials with density variation.</i>	84
<i>Figure 5.6.: Schematic (a) sigmoidal variation of the logarithmic flow stress vs. logarithmic strain rate and (b) strain rate sensitivity vs. logarithmic strain rate.</i>	88
<i>Figure 5.7.: Strain rate sensitivity versus strain rate at different strain values.</i>	88
<i>Figure 5.8.: Jump test carried out by Bae and Ghosh where the a variance of strain rate sensitivity values can be seen [Bae02a].</i>	89
<i>Figure 5.9.: Strain rate sensitivity versus strain rate at different strain values.</i>	90
<i>Figure 5.10.: Optimal strain rate path for a tensile test.</i>	90
<i>Figure 5.11.: shows the basic flow of data and actions from the start of an ABAQUS analysis to the end of a step.</i>	91
<i>Figure 5.12.: Difference in the surface where the backpressure (in blue) should be applied in different increments of the process.</i>	92
<i>Figure 5.13.: shows the basic flow of data and actions from the start of an ABAQUS analysis to the end of a step.</i>	92
<i>Figure 5.14.: Evolution of effective strain rate (a) and cavity area fraction (b) at the dome pole for Al5083 at 773 K at different stress states.</i>	94
<i>Figure 5.15.: Pressure time curves obtained using different control schemes and strain rate ratios for different control schemes.</i>	95
<i>Figure 5.16.: Pressure time curves achieved using smoothed pressure control strategy using different integration point numbers for obtaining the effective strain rate</i>	96
<i>Figure 5.17.: Pressure time curves achieved using smoothed fluid control strategy using different integration point numbers for obtaining the effective strain rate</i>	97
<i>Figure 5.18.: Final geometry and triaxiality map of bulge-test simulation for $2 \times 10^{-4} \text{ s}^{-1}$ control strain rate and 18 bar backpressure results.</i>	98
<i>Figure 5.19.: Pressure-time curves for controlled constant strain rate of $2 \times 10^{-4} \text{ s}^{-1}$.</i>	98

<i>Figure 5.20.: Pressure-time curves for controlled constant strain rate of $5 \times 10^{-4} \text{ s}^{-1}$.</i>	99
<i>Figure 5.21.: Pressure-time curves for controlled constant strain rate of $1 \times 10^{-3} \text{ s}^{-1}$.</i>	99
<i>Figure 5.22.: Pressure difference-time curves for toroid shape part with four different strategies: 2×10^{-4} constant strain rate, 2×10^{-4} constant strain rate with backpressure, 6×10^{-4} constant strain rate with backpressure and variable strain rate with backpressure.</i>	100
<i>Figure 5.23.: Cavitation fraction last increment maps for toroid-shape simulations, for: (a) target $2 \times 10^{-4} \text{ s}^{-1}$ constant strain rate. (b) target $2 \times 10^{-4} \text{ s}^{-1}$ constant strain rate with backpressure of 18 bar. (c) target $6 \times 10^{-4} \text{ s}^{-1}$ constant strain rate with backpressure of 18 bar. (d) m max strategy with backpressure of 18 bar.</i>	101
<i>Figure 5.24.: Fraction of cavitation in A area (Figure 5.23 a) of the toroid shape for four simulations.</i>	101
<i>Figure 5.25.: Triaxiality coefficient value maps (a) during the forming and (b) last increment for toroid-shape simulation the pressure-time curves obtained in the experiments for target $2 \times 10^{-4} \text{ s}^{-1}$ constant strain rate.</i>	102
<i>Figure 5.26.: Triaxiality coefficient value maps (a) during the forming and (b) last increment for toroid-shape simulation the pressure-time curves obtained in the experiments for target $2 \times 10^{-4} \text{ s}^{-1}$ constant strain rate with backpressure of 18 bar.</i>	103
<i>Figure 6.1.: Schematic representation of the SPF prototype</i>	107
<i>Figure 6.2.: Set of the SPF prototype in the servomechanical press.</i>	108
<i>Figure 6.3.: Schematic representation of the SPF oven.</i>	108
<i>Figure 6.4.: Movement of side doors for temperature sealing.</i>	109
<i>Figure 6.5.: "Sandwich" structure that shows a eating plane this electric heaters and thermocouples, insulation panels and cooling plate</i>	109
<i>Figure 6.6.: "Sandwich" structure of (1) cooling plate, (2) insulation panels and (3) heated plate</i>	110
<i>Figure 6.7.: Bulge-test die designed for this work.</i>	111
<i>Figure 6.8.: Concrete die production (a) silicone pattern and (b) final tooling.</i>	111
<i>Figure 6.9.: Set of tests made at different backpressure and strain values for $2 \times 10^{-4} \text{ s}^{-1}$ strain rate.</i>	112
<i>Figure 6.10.: Section of different interrupted bulge-test ed at $5 \times 10^{-4} \text{ s}^{-1}$ target strain rate and 18 bar backpressure.</i>	113
<i>Figure 6.11.: Comparison between simulated (red) and experimentaly measured (squared points) height of the pole of the dome for different strain rates applied 0.4 bar backpressue.</i>	114
<i>Figure 6.12.: Comparison between simulated (red) and experimentaly measured (squared points) heigth of the pole of the dome for different strain rates applied 14 bar backpressue.</i>	115
<i>Figure 6.13.: Comparison between simulated (red) and experimentaly measured (squared points) heigth of the pole of the dome for different strain rates applied 18 bar backpressue.</i>	116
<i>Figure 6.14.: Comparison of simulated and experimental thickness for 0.4 bar bulge-tests.</i>	117
<i>Figure 6.15.: Comparison of simulated and experimental thickness for 14 bar bulge-tests.</i>	117
<i>Figure 6.16.: Comparison of simulated and experimental thickness for 18 bar bakcpressure.</i>	118

<i>Figure 6.17.: Comparison of simulated and experimental cavitation for 0.4 bar tests</i>	<i>119</i>
<i>Figure 6.18.: Comparison of simulated and experimental cavitation for 18 bar tests</i>	<i>119</i>
<i>Figure 6.19.: Different bulge-test s obtained at backpressure of 0.4, 14 and 18 bar from the left to the right using the same $2 \times 10^{-4} \text{ s}^{-1}$ target strain rate forming history.</i>	<i>120</i>
<i>Figure 6.20.: . Comparison of simulated and experimental grain size for 0.4 bar tests</i>	<i>121</i>
<i>Figure 6.21.: . Comparison of simulated and experimental grain size for 18 bar tests.....</i>	<i>121</i>
<i>Figure 6.22.: Numerically obatined “true” strain rate values for theoretical $2 \times 10^{-4} \text{ s}^{-1}$ strain value in the pole of the dome.</i>	<i>122</i>
<i>Figure 6.23.: Numerically obatined “true” strain rate values for theoretical $5 \times 10^{-4} \text{ s}^{-1}$ strain value in the pole of the dome.</i>	<i>122</i>
<i>Figure 6.24.: Numerically obatined “true” strain rate values for theoretical $5 \times 10^{-4} \text{ s}^{-1}$ strain value in the pole of the dome.</i>	<i>123</i>
<i>Figure 6.25.: Four different tests carried out at different conditions of (a) at constant strain rate of 2×10^{-4} (b) at constant strain rate of 2×10^{-4} and a backpressure of 1.8 MPa, (c) at variable strain rate value that follows the maximum m value curve presented before and a backpressure of 1.8 MPa and (d) at constant strain rate of 6×10^{-4} and a backpressure of 1.8 MPa.</i>	<i>124</i>
<i>Figure 6.26.: Results of the thickness profile of the toroid-shape test for different conditions of at constant strain rate of 2×10^{-4} at constant strain rate of 2×10^{-4} and a backpressure of 1.8 MPa, 6×10^{-4} and a backpressure of 1.8 MPa and variable strain rate value that follows the maximum m value curve presented before and a backpressure of 1.8 MPa.</i>	<i>125</i>
<i>Figure 6.27.: Comparison of experimental and numerical results of the thickness profile of the toroid-shape test at target constant strain rate of $2 \times 10^{-4} \text{ s}^{-1}$.....</i>	<i>126</i>
<i>Figure 6.28.: Comparison of experimental and numerical results of the thickness profile of the toroid-shape test at target constant strain rate of $2 \times 10^{-4} \text{ s}^{-1}$ and backpressure of 18 bar.</i>	<i>127</i>
<i>Figure 6.29.: Comparison of experimental and numerical results of the thickness profile of the toroid-shape test at target constant strain rate of $6 \times 10^{-4} \text{ s}^{-1}$ and backpressure of 18 bar.</i>	<i>127</i>
<i>Figure 6.30.: Comparison of experimental and numerical results of the thickness profile of the toroid-shape test at target constant strain rate of maximum m strategy and backpressure of 18 bar.....</i>	<i>127</i>

LIST OF TABLES

<i>Table 2.1. Constitutive equations based on deformation mechanisms and physical behaviour.</i>	15
<i>Table 3.1. Chemical composition of Al 5083 alloy (wt. %)</i>	31
<i>Table 3.2. Interrupted tests carried out at different theoretical strain rates and theoretical strain values.</i>	44
<i>Table 3.3. Micrographs of the tensile test specimens at different conditions, electro-etched using Barker's etching reagent.</i>	46
<i>Table 3.4. Micrographs of the polished tensile-test specimens at different conditions of strain at $2 \times 10^{-4} \text{ s}^{-1}$ strain rate.</i>	48
<i>Table 4.1. Summary of the equations used for the viscoplastic model for voided material with density variation.</i>	64
<i>Table 4.2. Initial parameters for average grain size growth equation.</i>	67
<i>Table 4.3. Initial parameters for cavitation area fraction evolution equations.</i>	68
<i>Table 4.4. Fitted parameters for the initial model equation for viscoplastic voided material with fixed density.</i>	69
<i>Table 4.5. Fitted parameters for viscoplastic model for voided material with density variation equations</i>	71
<i>Table 6.1. Results of the four toroid-shape tests.</i>	125

NOMENCLATURE

Symbols

b	Burger's vector
d, d_0	current grain size, initial grain size
$D_{gb}, D_L, D_{IPB}, D_{eff}$	grain boundary lattice
$\mathbf{D}, \mathbf{D}^e, \mathbf{D}^p$	strain rate tensor, elastic strain rate tensor, plastic strain rate tensor
$\mathbf{D}^{vp}, \mathbf{D}_{dev}^{vp}, \mathbf{D}_{vol}^{vp}$	viscoplastic strain rate tensor, deviatoric viscoplastic strain rate tensor, volumetric viscoplastic strain rate tensor
e	engineering strain
E	Young's modulus
f_a	cavity area fraction
f_v	cavity volume fraction
F_t, F_n	friction force, normal force
\mathbf{I}	second-order identity tensor
K	is the strength coefficient
k_s	stress concentration factor
l, l_0, l_w, l_m, l_c	gauge length, initial gauge length, final gauge length, measured length, parallel length
m	strain rate sensitivity
M	grain boundary mobility
n	strain hardening exponent
P	pressure
Q	activation energy
r_{max}	strain rate ratio
R	universal gas constant
R	isotropic hardening variable
$s, s_0, S_f, S_t, \hat{S}$	sectional area, initial area, void area, total area, effective section area
S	engineering stress
t, t_0	thickness, initial thickness

t	time
t_r	rupture process time
T	temperature
V	volume
V_{cross}	cross-head velocity
w, w_0	sheet width, initial sheet width
$\varepsilon, \varepsilon_m, \varepsilon_c, \varepsilon_s$	uniaxial strain, measured uniaxial strain, parallel uniaxial strain, sectional uniaxial strain
$\bar{\varepsilon}^{cr}, \bar{\varepsilon}^{sw}$	Abaqus' creep strain, Abaqus' swelling strain
$\dot{\varepsilon}, \dot{\varepsilon}^p$	uniaxial strain rate, equivalent plastic strain rate
$\dot{\varepsilon}^{vp}$	equivalent viscoplastic strain rate
$\dot{\varepsilon}_{max}, \dot{\varepsilon}_{opt}$	maximum strain rate, target optimum strain rate
$\boldsymbol{\varepsilon}, \boldsymbol{\varepsilon}^{vp}$	strain rate tensor, viscoplastic strain rate tensor
λ	plastic multiplier
$\sigma, \sigma_e, \sigma_f, \hat{\sigma}$	stress, equivalent von Mises stress, uniaxial yield stress, effective stress
σ_m^μ	mean stress in grain boundaries
$\sigma_m^\infty, \sigma_1^\infty$	remotely applied mean stress, remotely applied maximum principal stress
$\boldsymbol{\sigma}, \boldsymbol{\sigma}'$	Cauchy stress tensor, deviatoric stress tensor
σ_0	threshold stress
$\sigma_m, \sigma_h, \sigma_1$	von Mises equivalent stress, mean stress, hydrostatic stress,
ω	damage variable
ϕ	yield function
ψ	cavity volume fraction growth parameter
μ	friction coefficient
χ_{GBS}	fraction of GBS strain

Abbreviations

GBS	Grain boundary sliding
CGBS	Cooperative grain boundary sliding
ECAP	Equal channel angular pressing
FEM	Finite element method
SPF	Superplastic forming

INTRODUCTION

1.1 Motivation and background

Environmental and economical issues, intensified by the increasing prices of fossil fuels, lack of viable alternative fuel sources, pollution and global warming, have been the source of a continuously growing pressure on the transportation industry to cut fuel consumption and limit emission levels. Among the different proposed options to achieve such cuts, reduction of mass remains the most influential and least costly one, provided that large cuts of 20-40% are realised [Col95].

Leading automotive manufacturers have shown in separate studies that more than 50% of fuel consumption is mass dependant [Jam97]. Similarly, for the aerospace industry, improving the fuel efficiency and emissions profile of aircraft is a major area of focus [San99]. In these areas, significant weight reduction would not be feasible without the extensive use of light materials with good mechanical properties and the possibility of manufacturing components with complex geometries using them.

Several titanium and aluminium alloys exhibit extraordinarily enhanced tensile ductility at elevated temperatures, a phenomenon known as superplasticity. This phenomenon has gained a lot of interest over the past few decades and was put into practice to form several titanium and aluminium alloys by means of the superplastic forming (SPF) technique [Osa97, San99, Bar99, San01, Bar07]. The technique offers several advantages over conventional forming practices; the ability to produce complicated shapes from metals difficult to form at room-temperature in one single step, is definitely the most interesting. Since the SPF technique was developed in the early 70s, it has had a growing interest in researching. Figure 1.1 shows the evolution of the number of papers related to SPF.

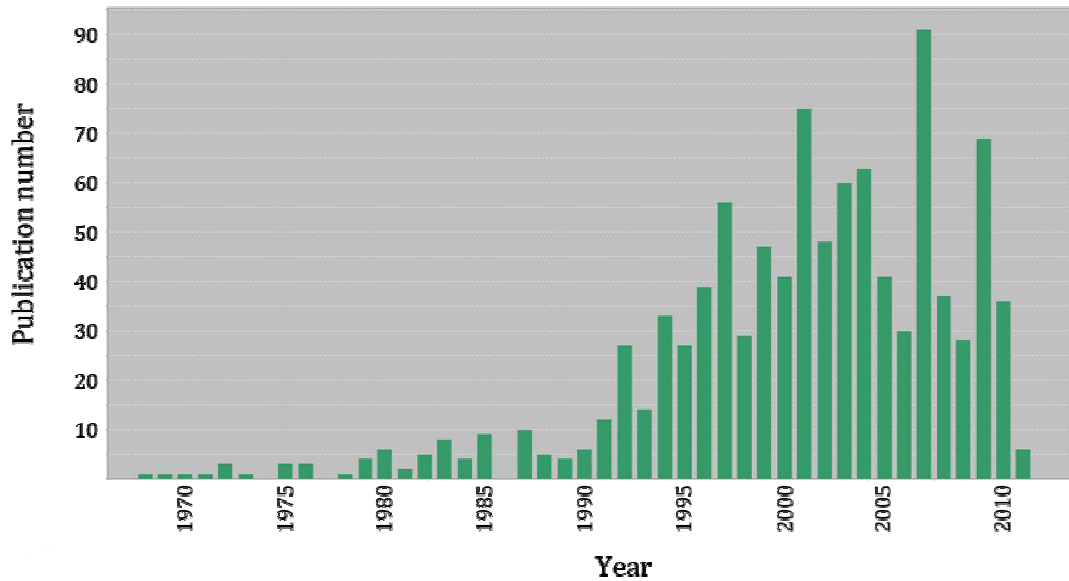


Figure 1.1.: Historical evolution of the publication number related to Superplastic Forming (source: Web of Knowledge).

A number of obstacles and issues that prevented its generalized use on a larger scale have inhibited the comprehensive application of this technique. The most critical issues are the inherent high process times and the limited predictive capabilities of deformation and failure. Actually, there is a need of accurate models that can describe the damage behaviour of superplastic materials and consequently predict its failure. The lack of precise material models has been reflected in the industry by the need of modifications in the pressure-time curves employed as input in the experimental equipments, where most SPF operations are carried out by trial and error routines.

In addition, since superplastic deformation is rate dependent, it is a common practice to avoid premature failure by forming at lower rates, which consequently, makes the SPF technique a rather slow forming process. Furthermore, it is necessary to avoid void growth in the superplastic alloys that suffer from cavitation damage to maintain the mechanical properties of the parts, a behaviour that can be inhibited using lower rates.

The SPF technique has proven to be an efficient process in forming various components for aerospace and medical applications [San99, Cur01, Bar07]. However, nowadays, when the global competitiveness is of a prior factor and there is a need to offer products with high added value, issues related to SPF need to be tackled. Solving these problems, we will be mainly able to reduce forming times of this process and to obtain more a more complex components that can reduce fuel consumption by means of transport.

1.2 Scope of the present thesis

The main objective of the present dissertation is to acquire knowledge on the superplasticity and superplastic forming of aluminium alloys, in order to optimize process-forming times and final parts characteristics for complex geometries.

For this aim, this research work is divided into next sections:

1. Characterize the superplastic behaviour of the Al-5083-SPF aluminium alloy, by establishing an accurate data, mainly when damage is present. Such characterization requires mechanical testing followed by microstructural examination, covering wide ranges of forming strain rates.

2. Develop a multi-axial constitutive model that has the ability to accurately capture the behaviour of superplastic materials during deformation in a wide range of strain rates. The model is based on the continuum theory of viscoplasticity, employs a volumetric strain rate, and accounts for microstructural changes within the material; i.e. grain growth and cavitation. In addition, continuum damage behaviour is implemented. This damage is assumed to be due to the cavitation behaviour, which is susceptible to reflect changes due to the loading state. Furthermore, an inverse analysis with the use of numerical models is used to have comprehensive and precise data when the tests exhibit a non-ideal uniaxial behaviour.

3. Design an appropriate SPF prototype that is able to form Al-5083-SPF aluminium alloy and Ti-6Al-4V titanium alloy. This prototype should be able to maintain an homogenous temperature and apply backpressure in a precise way.

4. Employ the superplastic bulge forming technique to form Al-5083-SPF aluminium alloy sheets into different geometries, at various operating conditions, based on specific optimization forming schemes.

5. Establish new forming strategies to optimize the process time as well as the thickness profile and cavitation value of the parts using numerical modelling. These optimum-forming schemes will be generated by using the developed constitutive model as basis applying a new concept presented in this work in a finite element code, followed by actual forming practices in order to validate the optimization approach.

A summarized structure of the thesis can be seen in Figure 1.2.

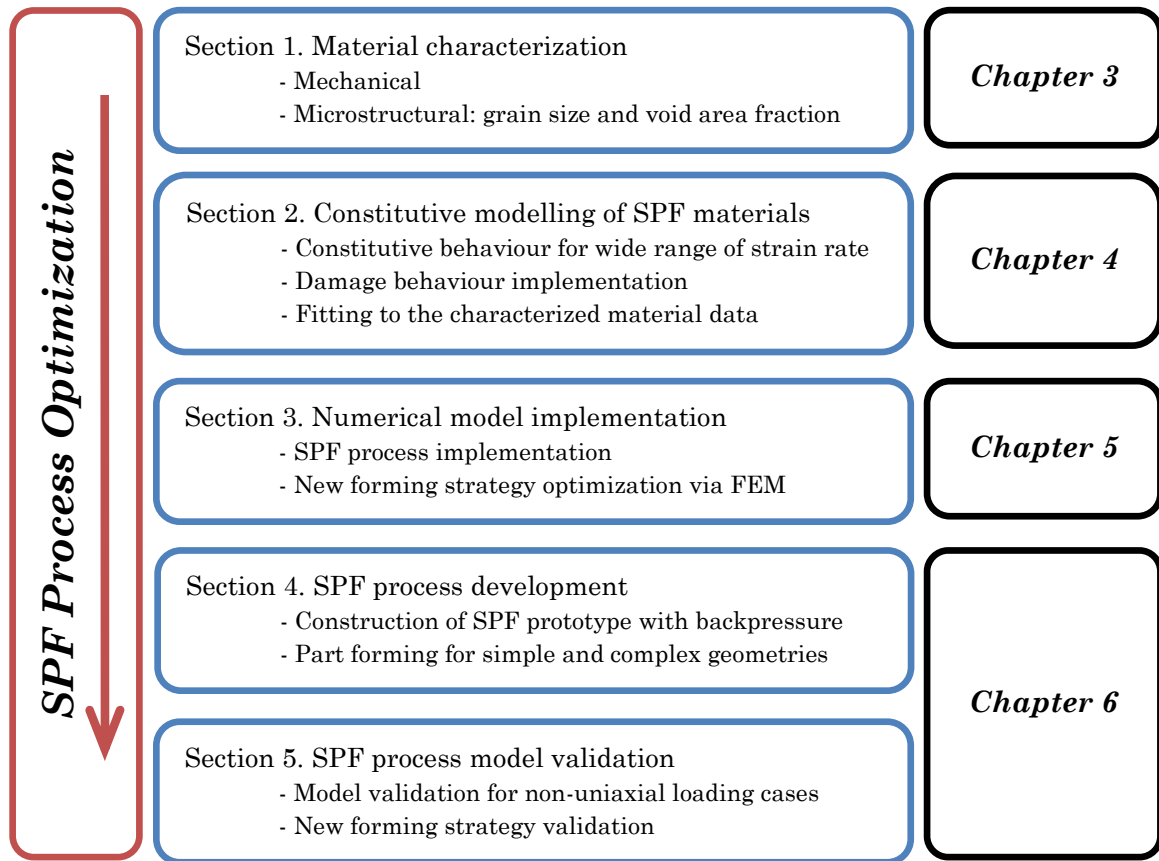


Figure 1.2.: Summarized structure of the information presented in this document.

CHAPTER 2

SUPERPLASTICITY AND SUPERPLASTIC FORMING

Synopsis

In this chapter, a bibliographical review and a general explanation of superplasticity and superplastic forming (SPF) is presented. On one hand, some general physical and mechanical aspects of superplasticity is explained. On the other hand, the blow SPF technique, commercial superplastic alloys and the finite element method (FEM) for SPF process optimization is presented.

As main concepts of this chapter have been the importance of the low strain rate and the high temperature in superplasticity, which is one of the main drawbacks of the SPF technique from a point of view competitiveness.

Other important concept is the use of FEM for the gas forming SPF optimization, a technique that has been improved the last years implementing mechanism-based strategies for process pressure-time curve optimum achievement.

2.1 Introduction

In this chapter, some background information about the main topics of this work is presented; superplasticity and the superplastic forming technique.

Firstly, a brief description of the superplastic behaviour and the basic requirements is done. Furthermore, a review of the history is fulfilled about the superplastic materials and superplastic forming technique and their research from the last hundred years.

Because of this different deformation mechanism, the mechanical properties of superplastic materials differ from conventional plasticity in terms of very low flow stresses and a very high strain rate dependency of these flow stresses. The physical mechanism of superplasticity is described in the second section of this chapter.

The third part of this chapter focuses on some superplastic materials, which are mostly used in industry nowadays. This section also describes the chosen material in this work, Alnovi-1.

The fourth part describes the mechanical behaviour of the superplastic materials, presenting different constitutive equation types that exist present in the current literature. Moreover, the equations of different mechanistic behaviours, which are valuable for describing the behaviour of the Alnovi-1 material, are presented.

The description of multiaxial behaviour is a very important issue in sheet forming simulations, so the fifth is dedicated to multiaxial mechanical behaviour of materials in different types of plasticity: the common von Mises yield criteria and the Gurson criteria for porous plasticity.

Finally, the superplastic forming technique is schematically explained, with a brief description of different variants and current applications of the aluminium Al5083 alloy.

2.2 Superplasticity

2.2.1 History

Superplastic materials are unique class of polycrystalline solids that have the ability to undergo extraordinarily uniform strains prior to failure. For deformations in uniaxial tension, an elongation higher than 200% is usually indicative of superplasticity. Several materials of this class can attain extensions greater than 1000%; Nich et al. reached the spectacular elongation of 20.000% as shown shown in Figure 2.1 [Pil89].

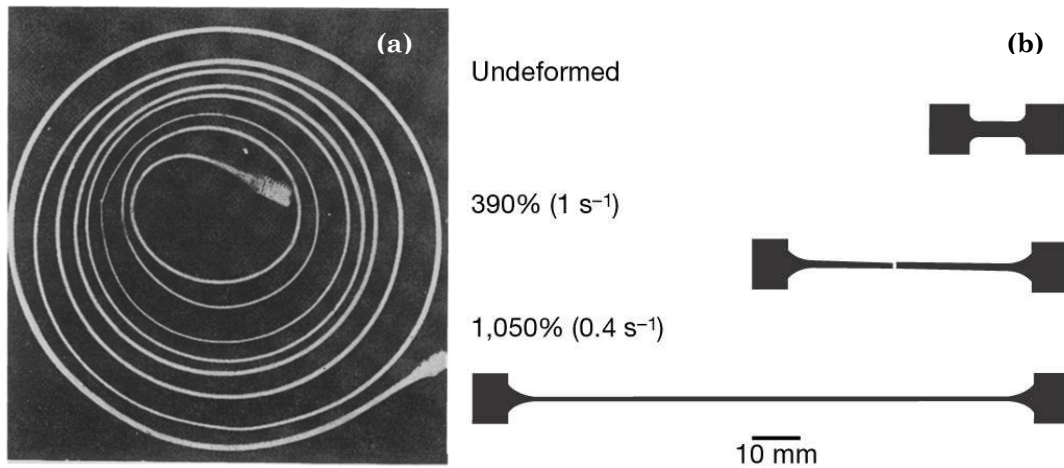


Figure 2.1.: Tensile specimens in superplastic state for polycrystalline materials: (a) Pearson's famous test of a Bi-Sn alloy that underwent 1950 % [Pea34] and Kim *et al.* tests for superplastic ceramics [Kim01].

Historically, it is not clear where the first observation of superplasticity was made. Some presume that superplasticity was first observed in USSR and others say that it was in the UK. Anyway it is believed that those early observations of this phenomenon were made in the early 1920's. The most remarkable of the earlier observations was that made by Pearson in 1934, where he reported a tensile elongation of 1950% without failure in a Bi-Sn eutectic alloy [Pea34]. After those early observations, there was little interest in this phenomenon, and the whole issue of superplasticity was consigned to a laboratory research level. Nevertheless, studies were carried out in the USSR, and the term superplasticity was given by Bochvar and Sviderskaya in 1945, when they were studying the extended ductility observed in Zn-Al alloys [Pil89].

After the Second World War, superplasticity was revived, and extensive studies started to take place on different scales in different periods of time. A high percentage of the basic research work was done in the late 60's and early 70's. In 1964, laboratory experiments were undertaken by Backofen *et al.*, demonstrating biaxial forming of ZnAl eutectoid sheet, bubbling a superplastic sheet (see Figure 2.2) [Bac64].

Many years later, superplasticity started to gain the interest in industry, and parts in different applications started to be produced by the superplastic forming (SPF) technique. Consequently, applied research started developing in order to satisfy industrial needs.



Figure 2.2.: The first published superplastically formed bubble [Bac64].

Nowadays, superplastic forming technique continues having its niche in the industry and having a high potential. Large amount of literature is available and research activities are expanding more to cover the various aspects of superplasticity. In addition, the superplastic forming technique is producing larger numbers of different parts. However, and despite the advances that have been achieved so far, there is plenty researching work to do in order to accomplish a wide commercial use of this forming technique.

2.2.2 Requirements for Superplasticity

As explained before, the high elongation attributed to superplasticity (ranging from a few hundred to several thousand percent) can only be obtained in a narrow range of operating temperature and strain rate. Within this range, superplastically deformed materials show a very high resistance against necking, so the material gets thinner in a uniform manner. Moreover, stresses to establish superplastic flow are low compared to conventional plastic flow. The main requirement for a material to behave superplastically is a fine grain size, which can vary from material to material between 1 and 10 μm . The grains should be randomly oriented in the material, so it behaves isotropically, and may not grow during plastic deformation, in order to maintain the superplastic properties throughout the entire forming process.

Three main requirements are generally needed to achieve superplastic behaviour in the material:

Fine and Stable Grain Structure

Generally speaking, grain structure with average grain size of less than 10 μm is usually required to attain superplasticity. As it will be shown later, the dominant deformation mechanism in superplasticity is the accommodated grain boundary sliding. Therefore, the smaller the grains are, the easier for them to rotate and slide over each other and accommodate larger strains before failure.

It should be emphasised that 10 μm is not a critical limit above which superplasticity is not feasibly achieved, as diverse superplastic materials behave differently. In fact, superplasticity in some coarse-grained aluminium and magnesium alloys has been reported

[Che05, Soe06]. Yet, it can be generalised that the smaller the grain size is the larger the deformation that can be attained before failure.

High Forming Temperature

In a similar manner and as it is the case with grain size, different alloys behave differently in terms of forming temperature. In general, superplasticity takes place at relatively elevated temperatures, usually above 50% the absolute melting point of the material. Some magnesium alloys, for instance, exhibit superplasticity at temperatures around that limit [Wat02], but on the contrary, the most common aluminium alloys (like Al5083 and Al7475) show a superplastic behaviour at near the down melting point. As a rule, the higher the forming temperature the larger the deformation can be attained before failure.

By combining the effects of both the grain size and temperature, it is known that the smaller the grain size, the lower the temperature that can be used to achieve superplasticity and vice versa [Pil89, Sal01].

Controlled Rate of Deformation

Superplasticity is often confined within a certain range of strain rates, typically between 1×10^{-5} and $1 \times 10^{-1} \text{ s}^{-1}$ [Pad01]. To explain this, it is necessary to address some of the mechanical aspects of superplastic deformation, which are covered in the section 2.5.

2.3 Physical mechanism of superplasticity

The exact micromechanical mechanism of superplasticity is still not understood completely [Nie05]. What is clear is that it is very different from the conventional behaviours of materials like elastoplasticity, viscoplasticity or creep.

At the moment it is believed (and also proved up to some extent) that superplastic flow is dominated by a process which is called Grain Boundary Sliding (GBS) [Moh01]. As the name suggests, boundary grains slide and this sliding is accommodated by means of some other mechanisms. These mechanisms are not completely understood yet, but the grain boundaries are known to play some important roles in superplasticity.

2.3.1 Grain boundary sliding

Grain boundary sliding is a process in which the grains slide past each other along their common boundary. At the optimal temperature for superplasticity, the boundary is weaker than the grains themselves, so sliding along this boundary seems a more efficient way for the material to deform plastically under the conditions of a high temperature and a low strain rate. Micromechanically, this is a very heterogeneous process. It has been observed that superplastic flow occurs because of the simultaneous sliding of groups of grains along each

other, which is denoted as cooperative grain boundary sliding (CGBS) [Kai02, Val83]. If during deformation grain growth is observed, then the formation of slide surfaces along which CGBS can act is restrained and the superplastic flow will stop. This means that grain growth has to be prevented as much as possible in order to achieve superplastic behaviour.

2.3.2 Accommodation mechanisms

If GBS was the only mechanism to occur in superplastic flow, then either the grains would have an ideal shape, such as a square, or huge cavities would occur in the material just before sliding takes place. Neither is the case. This means that in between the two grain boundary sliding steps another mechanism is responsible for this happening; it is called an accommodation mechanism [Nie05]. Two mechanisms will be discussed in this section, the diffusion creep and the intragranular slip. The mechanisms described are still under discussion, and it is also believed that grain boundary diffusion can be accommodated by partial melting in the boundary zone because of the elevated temperature. The effect of all accommodation mechanisms is maintaining a coherent shape between the sliding grain boundaries without introducing large cavities. The accommodation mechanism builds up until a certain threshold stress. If this stress is reached, then cooperative grain boundary sliding will take place in a fraction of the time of the build-up period.

Diffusion Creep

Diffusion Creep [Lan02] is a creep process, acting at very low stresses. Along the grain boundaries where a tensile stress acts there is an excess of vacancies. These vacancies can flow to areas where there is a shortage of vacancies, especially in areas where a tensile stress acts. These vacancies can travel through the grain (Nabarro-Herring diffusion creep) or along the grain boundary (Coble diffusion creep) [Moh02]. In superplastic flow, this can lead to a mechanism called grain switching, proposed by Ashby and Verrall [Ash73].

Intragranular Slip

If a slip plane arises inside a grain, then this is called intragranular slip. An extra boundary can grow inside this grain due to a collective movement of dislocations, which can assist in the mechanism of cooperative grain boundary sliding. Such a dislocation line inside a grain will then be collinear with the favourable sliding path. Intragranular slip is not seen in every superplastic material, this is especially seen in materials based on Al-Mg.

2.3.3 Grain growth

Since at a high enough temperature the grain boundaries in a superplastic material are weaker than the material in the grains itself, the superplastic properties of a material are very dependent on the grain size. There is a strong relationship between the grain size and the strain rate sensitivity parameter m [Bae00]. This parameter determines the superplastic

flow behaviour, as shall be shown in section 2.5. Because every grain boundary is an imperfection, the free energy of the material is higher at these places. Therefore, there is a tendency to grain growth to reduce this free energy. This process is temperature dependent and can be expressed as [Bae00]:

$$B' - B'' = d^{-\mu} \exp(-Q/RT) \quad (2.1)$$

in which d is the grain size, B' and B'' are constants, μ is grain size exponent, Q is the activation energy, R is the universal gas constant and T is the temperature and.

For normal grain growth, (also called static grain growth) where the strain rate is zero, g is equal to 2. This is a diffusion-controlled process, hence dependent on the temperature. Grain growth must be prevented as much as possible, because the fracture strain decreases as the grain size increases. This reduction of free energy can also be achieved by adding mechanical energy instead of thermal energy, which means that deforming the material also leads to grain growth, which is called dynamic grain growth.

Superplastic alloys have generally very good resistance to both types of grain growth, which is a result of the constituents (alloying elements).

2.3.4 Cavity formation

Most superplastic alloys develop internal cavitation during deformation [Nie05]. Cavitation is the phenomenon of internal void formation, which generally occurs within metallic materials during superplastic deformation. Excessive cavitation not only causes premature failure, but also imposes significant limitations on the industrial use of superplastically formed parts. Cavity growth is a result of diffusion-controlled mechanism or plasticity controlled mechanism. Diffusional cavity growth rate is stress-dependent and drops sharply after a rapid growth rate. Eventually, void growth rate during superplastic deformation is dominated by plastic flow of the surrounding matrix [Cho86, Sto84]. Because of the large deformation associated with superplasticity, in this work will be only considered void growth that is dominated by plasticity-controlled mechanism.

In the first stage of superplastic behaviour, cavities do not arise, and they are normally seen during the last stage of superplastic flow. The cavitation process consists of three stages, which can occur simultaneously.

Cavity nucleation

Some authors have suggested that there is no cavity nucleation for some superplastic materials like Al5083 aluminium alloy and cavity evolution is developed due to pre-existing cavities that exist in the as received material [Cha05]. On the contrary, other authors have claimed there is a nucleation of the cavities, and this was sustained by results of in-situ X-ray

tomography [Sal03] where the number of cavities shows a growing tendency in 3D measurements during the forming. The cavity nucleation is believed to take place at irregularities, where for instance the accommodation mechanism cannot completely compensate for the no coherence of the shape of adjacent grains. Most irregularities are at places where the grain boundary switches orientation (at triple junctions), or at places where second-phase particles are present [Sal03].

Cavity growth

Increasing strain, cavities can become larger. They act as large vacancies where minor vacancies in the structure can diffuse called stress directed vacancy diffusion. Cavity growth is one of the causes of unstable plastic flow.

Cavitation in superplastic materials is frequently quantified by the equation of variation with strain of the cavity volume fraction f_v according to:

$$f_v = f_{v0} \exp(\psi \epsilon) \quad (2.2)$$

where ψ is a cavity growth parameter and f_{v0} is a fitting constant which may be defined as an initial cavity volume fraction or a propensity of cavity nucleation depending on the strain rate, under the assumption that nucleation takes place in the early steps of strain.

An equation to describe the cavity volume fraction growth parameter was proposed by Pilling and Ridley [Pil89] base on the work of Cocks and Ashby [Coc82]:

$$\psi = \frac{3}{2} \left(\frac{m+1}{m} \right) \sinh \left[2 \left(\frac{2-m}{2+m} \right) \left(\frac{k_s}{3} - \frac{\sigma_m}{\sigma_e} \right) \right] \quad (2.3)$$

where m is the strain rate sensitivity, k_s is a stress concentration factor depending on the amount of grain boundary sliding, σ_m is the mean stress and σ_e is the equivalent stress.

One of the mayor benefits of this equation is that the triaxial factor σ_m/σ_e is implemented in it. Consequently, the effect of the load state of the material will vary the response of the equation. It must be noted that from earlier researchers [Bam83, Pil86, Ver96,] it follows that a hydrostatic pressure inhibits the formation and growth of cavities and thereby increases the maximum attainable plastic strain before mechanical failure of the material occurs.

Cavity coalescence

The internal voids start to interlink with each other to create a crack in the material. Despite its crucial effect on the elongation to fracture of the alloy, the coalescence process between cavities remains poorly documented [Sto83, Sto84, Pil85]. Modelling of this process is generally based on severe assumptions: coalescence occurs when cavities impinge, the

cavities are randomly distributed through the microstructure, and they have a spherical shape and have the same size. Moreover, it must be kept in mind that the models of cavitation in superplasticity are deduced from creeping materials [Coc82] and consequently do not take into account movements of the grains, which is the main mechanism of superplastic deformation. These movements result in a very complex cavity shapes and complex connections because of the coalescence of the cavities that cannot be seen only using 2D analysis technologies (Figure 2.3).

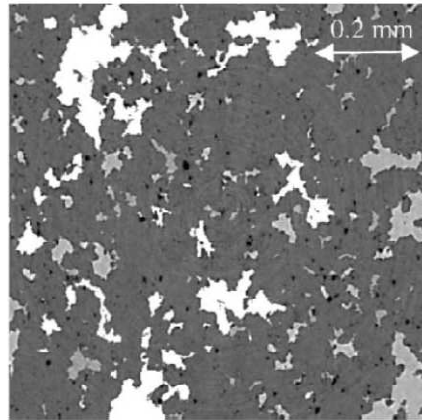


Figure 2.3.: 2D section of the 5083 aluminium alloy strained up to $\varepsilon = 1.65$. The cavities in white are in fact connected in 3D [Sal03].

As said earlier, cavity forming only arises during the last stage of superplastic forming and is an indication of fracture initiation, and therefore can lead to unrecoverable damage to the material. It is interesting to note that, in contrast to plasticity, cavities in superplastically formed materials are much more rounded but complex [Sal03].

2.4 Mechanical behaviour of superplastic materials

Superplastic materials show a very high sensitivity in mechanical properties, especially the flow stress, with respect to the strain rate. Temperature is an important aspect too. At the optimal superplastic temperature, the stress-strain behaviour looks like the graphs plotted in Figure 2.4 [Rid05], from which the conclusion can be drawn that the flow stress is very low at this optimal temperature.

The following simple relation gives the general expression for flow stress in a rate-dependent material in terms of the strain rate:

$$\sigma = K\dot{\varepsilon}^m \quad (2.4)$$

where σ is the flow stress, $\dot{\varepsilon}$ is the strain rate, K is the strength coefficient, and m is the strain rate sensitivity index.

The most important mechanical characteristic of superplasticity is the high strain rate sensitivity of the flow stress. For superplastic materials, the value of m ranges between 0.3 and 0.7. The larger the value of this index the more resistance the material has to necking, and so the higher the capability of the material to undergo large plastic deformation prior to failure. A typical logarithmic stress/strain rate curve for a superplastic material is shown in Figure 2.4. The slope of this sigmoidal-shaped curve at any point represents the value of the strain rate sensitivity index m at that point.

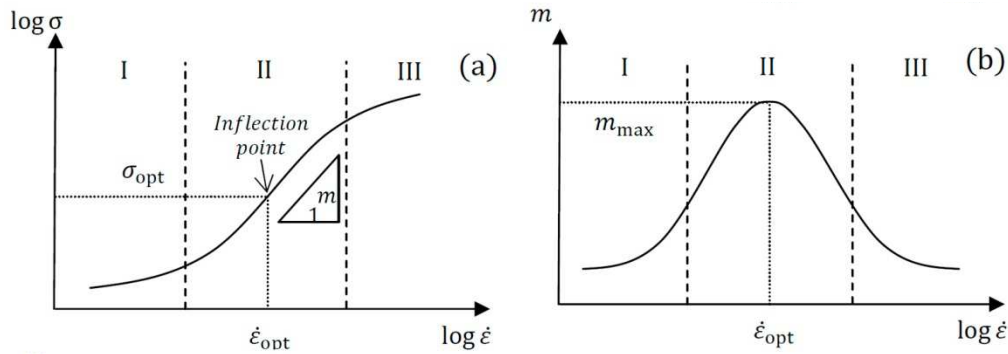


Figure 2.4.: A typical sigmoidal-shaped logarithmic stress/strain rate curve (a) and the corresponding bell-shaped sensitivity curve (b) for a superplastic material.

Accordingly, the curve can be divided into three main regions where different microstructural mechanisms are believed to dominate the deformation behaviour [Pil89]. Superplasticity occurs only in region II, where the strain rate sensitivity index m has high values at moderate strain rates, which is accompanied by very large elongation. And unlike conventional materials, which rely on work hardening to develop neck resistance, superplastic materials achieve neck resistance because of the high strain rate sensitivity of flow stress. Although the deformation process in this region is not very well understood, it is believed that grain boundary sliding accompanied by diffusion or dislocation glide and climb is the dominant mechanism, as explained before.

Based on the sigmoidal curve shown in Figure 2.4, and in order to stay inside the superplastic region, the rate of deformation (strain rate) used to deform a superplastic material shall be kept within the limits of the superplastic region-II. More specifically, it should be as close as possible to the peak value of m . As mentioned before, the superplastic region usually falls between the 1×10^{-5} and $1 \times 10^{-1} \text{ s}^{-1}$, although this is more often between 2×10^{-3} and $2 \times 10^{-4} \text{ s}^{-1}$ [Pil89]. These strain rates are much lower than typical hot forming rates. Consequently, it is always desirable to have region-II shifted to the right (towards the higher strain rates) as possible; this can be attained by increasing the forming temperature, and/or refining the grain structure of the superplastic material prior to the forming process. Anyway, the effect of some damage mechanism should be taken into account too.

2.4.1 Physical material constitutive equations

During the last decades, several laws based on predominating superplastic deformation mechanisms have been formulated for different kind of materials [Rua88]. Several examples of such laws are presented in Table 2.1. In this table, K_1 - K_8 are materials constants, σ_0 is the threshold stress, T is the absolute temperature, d is the grain size, b is the Burger's vector, E is Young's modulus, Q is the activation energy, k is the Boltzmann constant, D_{gb} , D_L , D_{IPB} and D_{eff} , are grain boundary, lattice, interphase boundary and effective diffusion coefficient, respectively.

Table 2.1. Constitutive equations based on deformation mechanisms and physical behaviour.

Name	Equation	Comments
Asbhy-Verral	$\dot{\epsilon} = K_1(b/d)^2 D_{eff}(\sigma - \sigma_0)/E$	Diffusional accomodation
Ball-Hutchinson	$D_{eff} = D_L[1 + (3.3w/d)(D_{gb}/D_L)]$ $\dot{\epsilon} = K_2(b/d)^2 D_{gb}(\sigma/E)^2$	GBS accommodated by dislocation climb
Langdon	$\dot{\epsilon} = K_3(b/d)^2 D_L(\sigma/E)^2$	Movement of dislocation adjacent to GBs
Gifkins	$\dot{\epsilon} = K_4(b/d)^2 D_{gb}(\sigma/E)^2$	Pile-up at tripe points (core-mantle)
Gittus	$\dot{\epsilon} = K_5(b/d)^2 D_{gb}(\sigma - \sigma_0/E)^2$	Pile-up at interphase boundary
Arieli and Mukherjee	$\dot{\epsilon} = K_6(b/d)^2 D_{gb}(\sigma/E)^2$	Climb of individual dislocation near GBs
Ruano and Sherby	$\dot{\epsilon} = K_7(b/d)^p D_{eff}(Eb^3/K_8T)^q(\sigma/E)^n$ $D_{eff} = D_L f_L + D_p f_p + D_{gb} f_{gb}$	Diffusional flow, grain boundary sliding, slip creep
Kaibyshev <i>et al.</i>	$\dot{\epsilon} = K_9/K_{10} T(b/d)^p D_0 \exp(-Q/K_{11}T) (\sigma - \sigma_0/E)^2$	Hardening and recovery of dislocations at GBs
Padmanabhan	$\dot{\epsilon} = K_2(b/d)^2 D_{gb}(\sigma/E)^2$	Diffusional accommodation

$K_1 - K_{11}, A, n, q, p =$ material constants, $\sigma_0 =$ threshold stress, $w =$ grain boundary width,
 $b =$ burgers vector

The different expressions have almost the same form and are based on the Power law. Nevertheless, the number of parameters to be determined (from 2 to 15) differs. It can also be noticed that all the equation have a fixed value of the strain rate sensitivity coefficient: $m = 0.5$ or $1/m = 2$. The grain size d is never neglected and has an inverse proportionality with the flow stress. These models can give good correlation between experimental and calculated results. However, a part of this success must be attributed at the fitting of the different parameters. Fixing the strain rate sensitivity coefficient limits the model to a small domain of the strain rate – temperature space. Actually, m is strongly dependant of temperature and strain rate. Generally talking, the validity of these equations is limited to the superplastic domain and sometimes to more limited temperature and strain rate conditions.

Besides these models, more of modern theories have been established to describe superplastic flow in terms of physical constitutive equations, but the main drawback of these models is the fact that no standard test has been described to determine the necessary parameters. In addition, the range of applicability cannot be predicted and the models do not allow for transient regimes of loading.

2.4.2 Mechanical material constitutive equations

In general, the constitutive equations used for simulating SPF process in a macroscopic scale are phenomenological. There are plenty of phenomenological constitutive equations in the literature [Cha02], but in this work only two types will be described: the more general use power law equations and the sigmoidal form hyperbolic sine equations.

Power law equations

The power law is a well-accepted phenomenological model. This type of equation is based on the general expression for flow stress in a rate-dependent material is given in terms of the strain rate explained by the equation 2.5.

Based on the phenomenological form of superplastic behavior, the uniaxial flow stress σ is seen to be a strong function of inelastic strain-rate $\dot{\varepsilon}$ and a weak function of strain ε and grain size d . The material is assumed to be purely inelastic and incompressible. A functional form of the constitutive relationship is given by:

$$\sigma = f(\varepsilon, \dot{\varepsilon}, d) \quad (2.5)$$

Alternatively the function can also be expressed in terms of logarithmic quantities as:

$$\ln \sigma = f(\ln \varepsilon, \ln \dot{\varepsilon}, \ln d) \quad (2.6)$$

By expanding the above form in terms of Taylor's series at a given equilibrium state, and neglecting the higher order terms we can write as 2.8 [Cha02]:

$$\sigma = K_1 \varepsilon^n \dot{\varepsilon}^m d^p \quad (2.7)$$

where

$$m = \frac{\partial(\ln \sigma)}{\partial(\ln \dot{\varepsilon})}, \quad n = \frac{\partial(\ln \sigma)}{\partial(\ln \varepsilon)}, \quad p = \frac{\partial(\ln \sigma)}{\partial(\ln d)} \quad (2.8)$$

m , n , p are material constants. It can be seen that m is the strain-rate sensitivity, n is the strain hardening exponent, and p is the grain growth exponent. The above equation can further be simplified by neglecting the effect of grain growth, leading to extended power-law or double power law model given by:

$$\sigma = K_1 \varepsilon^n \dot{\varepsilon}^m \quad (2.9)$$

The above equation can further be simplified as

$$\sigma = K_1 \dot{\varepsilon}^m \quad (2.10)$$

This last equation is the most simple one that can be used for describing superplastic material.

Sigmoidal form equations

As it is shown in the Figure 2.4, typically, most superplastic materials show a sigmoidal variation of the flow stress with strain rate [Pil89]. The power law constitutive equations are not capable of describing this sigmoidal behaviour if a constant m value is picked.

Aiming to have equations that are applicable for a bigger range of strain rate, the sigmoidal equations usually based of sin and hyperbolic sin were developed [Kim97, Ave66, Pac67].

One of the most important set of equations of this type is the one developed by Zhou and Dunne [Zho96], which is given by:

$$\dot{\varepsilon}_p = \frac{\alpha}{d^\gamma} \sinh \beta (\bar{\sigma} - R - \sigma_y) \quad (2.11)$$

$$\dot{R} = (C_1 - \gamma_1 R) \dot{\varepsilon}_p \quad (2.12)$$

$$d = \frac{(\alpha_1 + \beta_1 \dot{\varepsilon}_p)}{d^\mu} \quad (2.13)$$

where ε and ε_p are total and plastic strain, d is average grain size, R is an isotropic hardening variable, f_{a0} is the initial void fraction area, m is the strain rate sensitivity, σ_h is the hydrostatic stress, $\bar{\sigma}$ is the effective von Mises stress, σ_y is the yield stress and E is Young's modulus. α , β , γ , C_1 , γ_1 , α_1 , β_1 and μ are constitutive constants.

2.5 Superplastic materials in industry

This section is focused on the most common materials that can be used in superplastic deformation processes. These materials are mostly aluminium or titanium based alloys, but some stainless steel or less common materials can show superplastic behaviour too. Superplastic materials contain generally dedicated alloying elements commonly with the purpose of inhibiting grain growth directly.

Despite the wide variety of methods available for obtaining fine-grained microstructures, only a limited number of distinct alloys showing extensive superplasticity are exploited on a commercial scale. These include:

2.5.1 Aluminium-based materials

Some of the most used alloys in SPF are aluminium-based materials. These materials belong to the category of pseudo-single phase materials, with relatively small amounts of second-phase elements. They have a high resistance to static grain growth, and typical superplastic forming temperatures are about 500 to 550 °C.

The first superplastic aluminium alloys were especially developed for having excellent superplastic properties. However, these alloys were difficult to implement in the industry due to the unfamiliarity of component designers with these new alloys, so material scientists and material producers started developing known aluminium alloys with superplastic properties. The most common ones are listed below:

SUPRAL 100 and 150

The commercial names for Al-2004-SPF aluminium SUPRAL 100 and SUPRAL 150. It is a medium-strength alloy with mechanical properties similar to AA6061 and AA2219 and is used in lightly loaded or nonstructural applications, e.g. in the aerospace industry. AA2004SPF is alloyed with 6% Cu and small amounts of Mg and Zr. It can reach a nominal plastic strain before fracture of more than 200% [Pye81].

Formall 545 and 700

Formall is the commercial name for superplastic aluminium alloys manufactured by Aluisse Swiss aluminum and comes in two alloy types, AA5083-SPF and AA7475-SPF, respectively. In AA5083, the main alloying element besides aluminium present in this alloy is magnesium; in AA7475 zinc and copper are the main alloying elements [Chen04]. For these materials, some superplastic material data was found in the literature. AA5083-SPF has a strain rate sensitivity parameter of 0.60 at a flow stress of 3 MPa, whereas AA7475-SPF has a strain rate sensitivity parameter of 0.70 at a flow stress of 3 MPa at the superplastic temperature. Applications are, for instance, car body panels in the automotive industry. The maximum nominal plastic strain before fracture is about 400 % [Ver95].

Alnovi-1

It is a relatively new material also based on AA5083, manufactured by Furukawa Sky Aluminum, Japan. It is designated a superplastic material, although it does not reach the extremely high plastic strains which can be reached by other superplastic materials. A grain growth inhibitor is added in its manufacturing (0.8% Mn). At room temperature, this material has a high strength (yield strength of 160 MPa and tensile strength of 297 MPa).

The optimal superplastic temperature is between 500 °C and 550 °C. At this temperature, a stretch of 300 to 500% can be reached according to the manufacturer [Fur12]. Alnovi-1 will be used during this research project.

2.5.2 Titanium-based alloys

Titanium has a much higher melting point in comparison with aluminium, the superplastic processing temperature of titanium-based alloys is about 900 °C. Below this temperature, pure titanium consists of a hexagonal close-packed structure, called the α -phase. Above this temperature, the structure is body-centred cubic, which is called the β -phase. The α -phase is particularly useful in cryogenic applications, where the material has its best strength properties, whereas at room temperature the strength is low. The β -phase has a much higher strength at room temperature, but this phase can only be contained at room temperature if the material is solution-treated with e.g. vanadium. Superplastic behaviour of titanium alloys can only be observed in a mix of the two phases, so stabilizers should be added to ensure that these two phases keep existing in the alloy. Aluminium, which can be added up to 8%, is an α -stabilizer, whereas molybdenum and vanadium are the best known β -stabilizers.

Ti-6Al-4V alloy

This is the most used superplastic titanium alloy, especially for the manufacturing of structural aircraft parts. It has a superior strength-to-weight ratio and corrosion resistance at high temperatures. Its optimum forming temperature with respect to superplasticity is about 900 °C, but the range of temperatures in which superplastic behaviour is active is quite broad (between 700 and 950 °C) [Sem98]. At room temperature, the maximum elongation is about 20%, but this value increases quickly starting at a temperature of about 500 °C to a value of over 300% at the optimal superplastic temperature [Jai91]. Above 800 °C, the material suffers from dynamic grain growth, which then will be more dominant with respect to dynamic recrystallization.

2.5.3 Production of superplastic materials

Adding energy, by deforming a material plastically, can result in a reduction of the grain size. A method to achieve superplastic bulk material is by torsion under pressure. A better known process is the so-called Equal Channel Angular Pressing (ECAP) [Zhu00,Sto01], see Figure 2.5. In the case of ECAP, a billet of material is pushed through a channel with a sharp bend in it, which results in simple shear. The two channels of the tool have the same cross section, so the cross-sectional area during this deformation process does not change. This process is repeated several times to obtain an ultra-fine grain size. This process is also used for materials to be used at room temperature, since according to the Hall-Petch relationship, the strength increases at decreasing grain size.

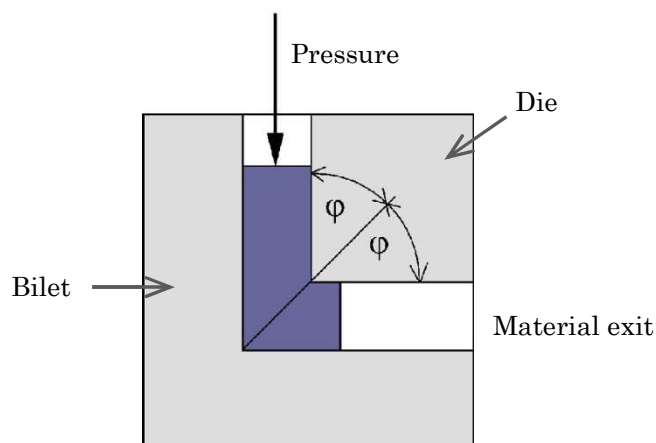


Figure 2.5.: Schematic view of Equal Channel Angular Pressing.

A process to produce sheets of superplastic material is by Accumulative Roll Bonding (ARB) [Kra04]. A sheet of material is rolled until half the thickness and twice the length, and then cut into two to obtain two sheets with the original dimensions but with half the thickness. Then these two new sheets are stacked and the rollbonding process of thinning and lengthening starts again.

2.6 Superplastic forming technique variants

The superplastic forming (SPF) technique is the process used to form superplastic materials. It is considered a near-net shape forming process, with tremendous cost and weight saving potentials over conventional forming operations. There are several SPF techniques. Here different variants of the blow forming technique will be explained [Bar99]:

Simple female blow forming

The first and most commonly used is cavity forming, in which a preheated superplastic sheet is clamped and forced into a die cavity by gas pressure. As the others blow forming variants, it uses a single die surface rather than the matched dies used in typical sheet metal forming operations. This is schematically illustrated by Figure 2.6. This method is ideal for producing more than one component from the same sheet, thus reducing unit costs

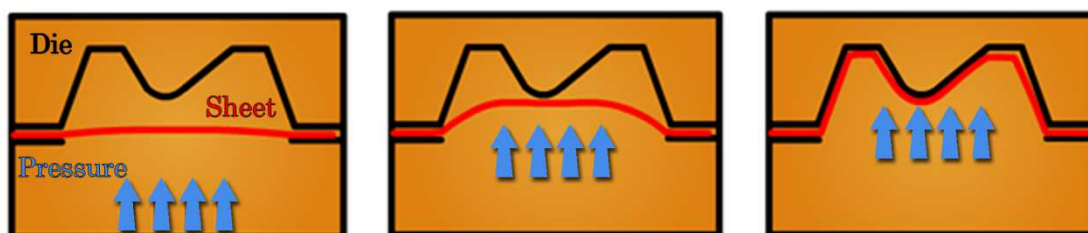


Figure 2.6.: Schematic of the superplastic simple female blow forming technique.

Male forming

Other variant of superplastic blow forming is illustrated in the Figure 2.7. The preheated alloy is clamped between a bubble plate and the tool plate, with air pressure being introduced from below to stretch the sheet into the bubble, Figure 2.6. The tool is then pushed up through the plane of the sheet's original position and into the bubble until the sheet is tensioned at the required height. Air pressure is then applied above the bubble, forcing the sheet into close contact with the tool, thus allowing the production of highly complex forms with increased aspect ratios and more uniform thickness distribution. It is ideally suited to deep complex components especially where wall thickness needs to remain relatively constant during and after forming.

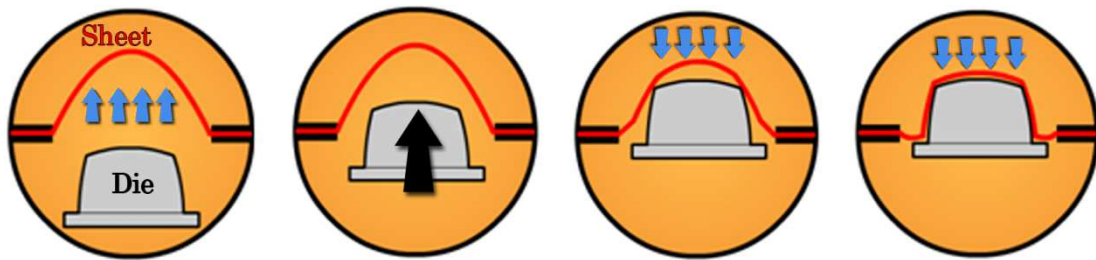


Figure 2.7.: Schematic of the superplastic male forming technique.

Diaphragm forming

Diaphragm forming allows non-superplastic alloys or composites to be formed successfully into complex 3D shapes or to obtain more homogeneous thickness distribution. The sheet is formed thanks to the force applied with a superplastic sheet, which is deformed by a gas pressure.

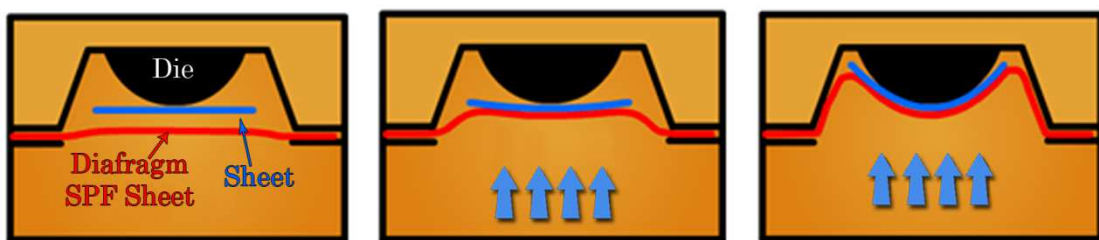


Figure 2.8.: Schematic of the superplastic diaphragm forming technique.

Backpressure forming

The backpressure forming is similar to cavity blow forming but the process differs by using gas pressure from both sides of the sheet and slowly forming the hot sheet using slight pressure differential (Figure 2.9). This maintains the integrity of the sheet and allows forming of structural components since the loading state of the material is different and the void growth is inhibited.

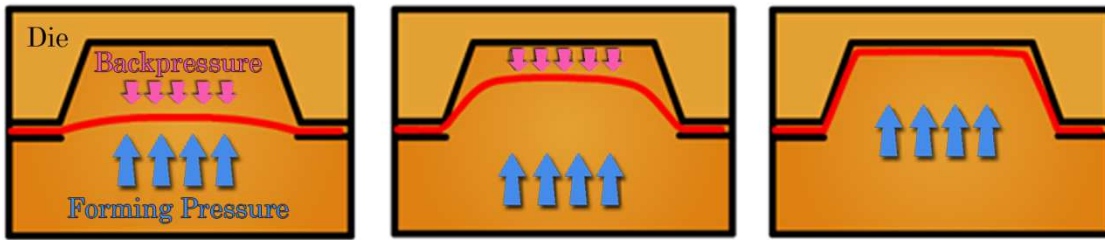


Figure 2.9.: Schematic of the superplastic blow forming technique with back pressure.

This technique uses two different channels for the gas pressure that must be synchronized. As can be seen in the Figure 2.10, both channels pressure is increased together to reach the same pressure value, where there is no sheet forming. The forming stage is the second one and the two channels present a pressure differential. In the last stage, the two pressures return to the same value and are decreased to the ambient pressure value for technical reasons.

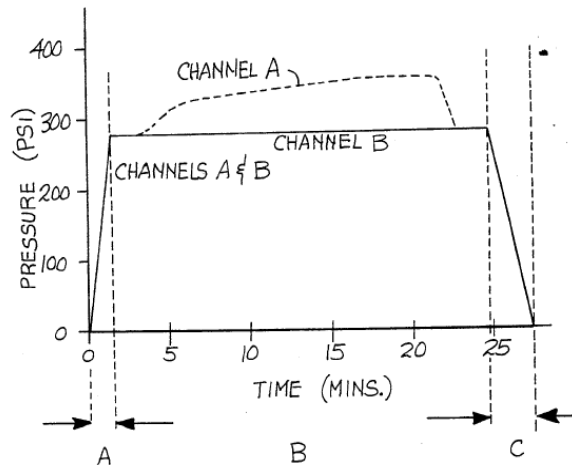


Figure 2.10.: Scheme of the pressure-time curve of the two channel of the superplastic blow forming technique with back pressure [Usp95].

The superplastic forming technique offers many advantages over conventional forming operations, such as:

- The ability to form very complex shapes, which cannot be formed by conventional methods, or can be accomplished by a larger number of parts and steps.
- The ability to form very hard materials, with relatively small flow stresses.
- Reduced number of forming steps, since SPF is usually carried out in one single step.
- Reduction of the total number of parts, and consequently the number of fasteners and joints, which leads to safety improvement in certain applications (aerospace for instance).
- Greater design flexibility and dimensional control.

However, the technique still faces some obstacles that limit its use on a large scale, such as:

- Slow and speed-limited forming process, which makes it unfavourable for mass-production applications.
- Expensive pre-forming steps, like the preparation of the fine grain-structured material, and heating to the desired forming temperature.
- Limited predictive capabilities of deformation and failure, mirrored by the trial and error practices in forming operations.
- Lack of comprehensive data regarding superplastic materials.

2.6.1 Current Applications of SPF

Despite the fact that superplastic forming technique is still considered non fully developed technique, and the number of obstacles hindering its widespread use, SPF has found its niche in many applications. The aerospace industry is the biggest market for SPF, yet automotive, medical, sports, cookware and architectural applications have their share too. The Al-5083-SPF superplastic aluminium alloy and other aluminium alloys can be used in the fabrication of airframe control surfaces and other small-scale structural elements, where lightweight and high stiffness are required. Figure 2.11 shows several aeroplane components formed from different aluminium alloys, produced by Superform Aluminium [Sup10].

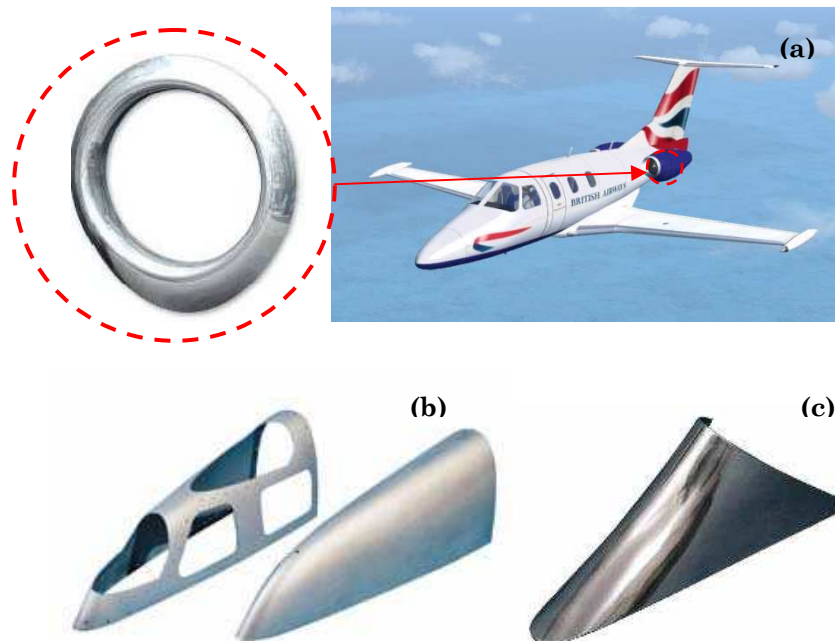


Figure 2.11.: Superplastic forming used for aeroplane applications [Sup10] (a) Eclipse 500 Jet (b) Boeing 777 (c) Boeing 737 using Al5083 aluminium alloy.

There are also manufacturers producing parts for automotive applications. Expectedly, such parts are not found in mass-produced cars, but rather in high tag price cars produced at much lower rates, as the two examples shown in Figure 2.12.

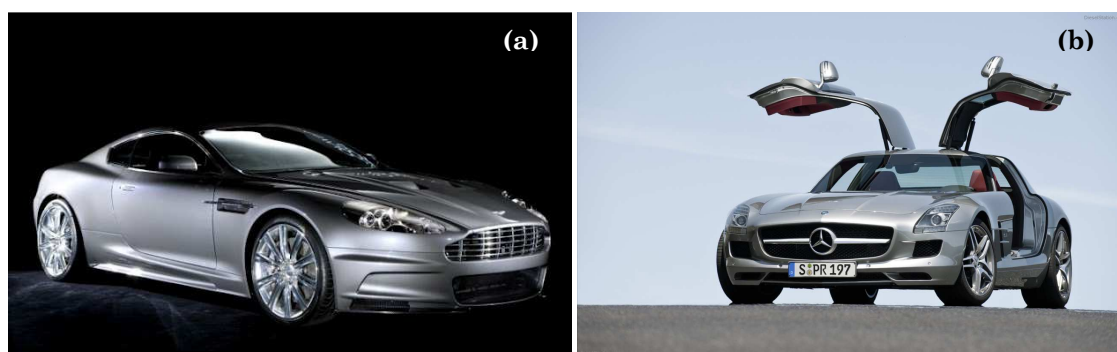


Figure 2.12.: Superplastic forming used for automotive applications (a) Aston Martin Vanquish (b) Mercedes-Benz SLS AMG.

All exterior body panels of the new Aston Martin Vanquish are superplastically formed using aluminium, with each panel hand tailored to the central structure to ensure a perfect fit. Likewise, the coupe Mercedes-Benz SLS AMG's "gullwing" doors are manufactured using SPF techniques [Mer10].

One of the areas of application where superplastic forming capabilities clearly surpass other forming processes is the medical field. The components shown in Figure 2.13, for example, are superplastically formed using titanium, a metal known for its bio-compatibility [Cur01, Bon06]. Any other forming process can hardly produce such highly detailed profiles efficiently.

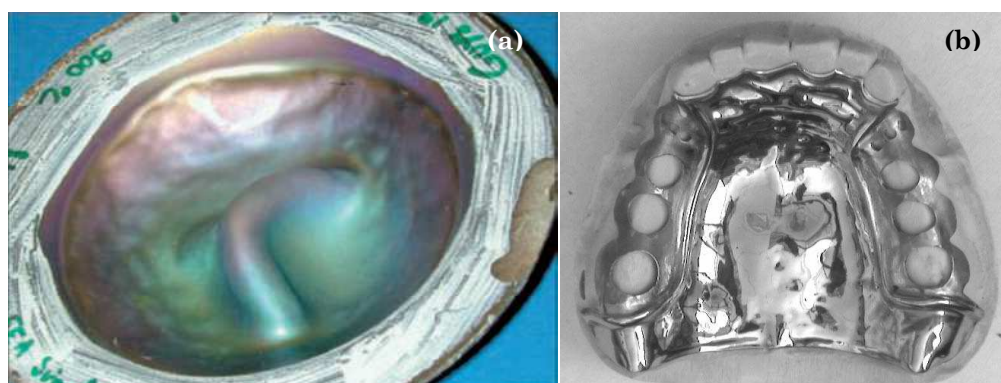


Figure 2.13.: Superplastic forming used for medical applications, superplastically formed part and the final palate [Cur01].

In sports, different titanium alloys (like SP700) have been used to produce some equipment by superplastic forming; a successful example is the golf-club head produced by Yamaha [Osa97]. Duplex stainless steel is superplastically formed into different cookware

equipments, and sink decks for passenger aircrafts. This superplastic material covers almost 30% of the Japanese market demand for such applications [Osa97].

Finally, even artists and architects sighted the capabilities of SPF in producing complex geometries, and used it in different occasions. This is the case of designer Ron Arad that has become known for his highly styled furniture and uses the superplastic forming technique to blow aluminium into biomorphic moulds.

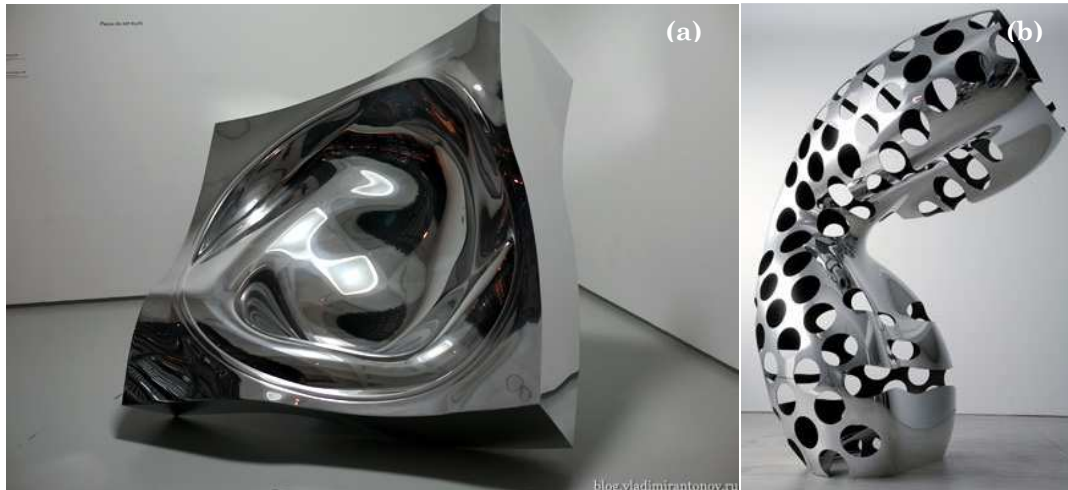


Figure 2.14.: Superplastic forming used for desing furniture [Ara12].

2.7 Finite element method in SPF

Traditionally SPF manufacturing processes are invariably designed a trial and error basis coupled with considerable experience and some simple calculations. However, if maximum benefit of SPF is to be gained then some form of numerical simulation of the forming process is essential. Different analytical numerical analyses have been developed [Ban05] but the finite element method can be considered as the most potent technique for modelling superplastic forming.

For the dominant thin sheet gas forming, the FE method can predict the progress of the shape and the development of diffusion bonding during forming, it can predict the final thickness distribution and most significantly, the optimum pressure-time cycle. The design of superplastic forming process is more difficult than the design of the conventional manufacturing operations [Ham01, Bon90, Woo96]. Successful production of components by superplastic forming requires a process design that guarantees optimal superplastic conditions.

It is essential to control the strain rate or another parameter that allows controlling the viscoplastic instabilities of the material. Strain rate deviating from superplastic regime can result in necking and rupture of the material.

2.7.1 Optimization of SPF via FEM

Different strategies have been used to avoid superplastic instabilities of the material and get optimum-loading curves. Some authors has presented studies using constant strain rate approaches that control algorithms to obtain a maximum constant strain rate during the process [Ham01]. Different control schemes for keeping track of the maximum strain rate to constant has been developed for some commercial software like Abaqus and Mark [Aba08, Mar10].

Different authors have reported variable strain rate strategies that provide solutions for obtaining pressure –time profiles maintaining the optimum SPF behaviour thorough the gas-forming process [Din95,Naz04,Khr06]. In general, they are based in Hart’s stability criterion [Har67].

Hart defined the conditions for stable deformation as:

$$(d\dot{A}/dA) \leq 0 \tag{2.14}$$

where A is the instantaneous cross-section of the sheet.

Ding et al. [Din95] analyzed superplastic blow forming process of thin sheet and obtained a stable deformation path that reduced production time. For this aim, the stability criterion presented by Hart [Hart67] is extended to superplastic forming with grain growth hardening and combined with an optimization approach. These authors made further extended his research from uniaxial state of stress to biaxial state of stress, which is a dominant stress state in superplastic sheet blow forming process [Din97].

Khraisheh et al. [Naz04, Khr06] carried out a study in order to determine an optimum pressure profile for superplastic forming in order to reduce the forming time and maintain the desired thickness distribution. In this case, Khraisheh *et al.* used an AZ31 magnesium alloy, and therefore, an instability criterion based on geometrical and microstructural (grain growth and cavitation behaviour) aspects was implemented for the pressure-time curves optimization (see Figure 2.15).

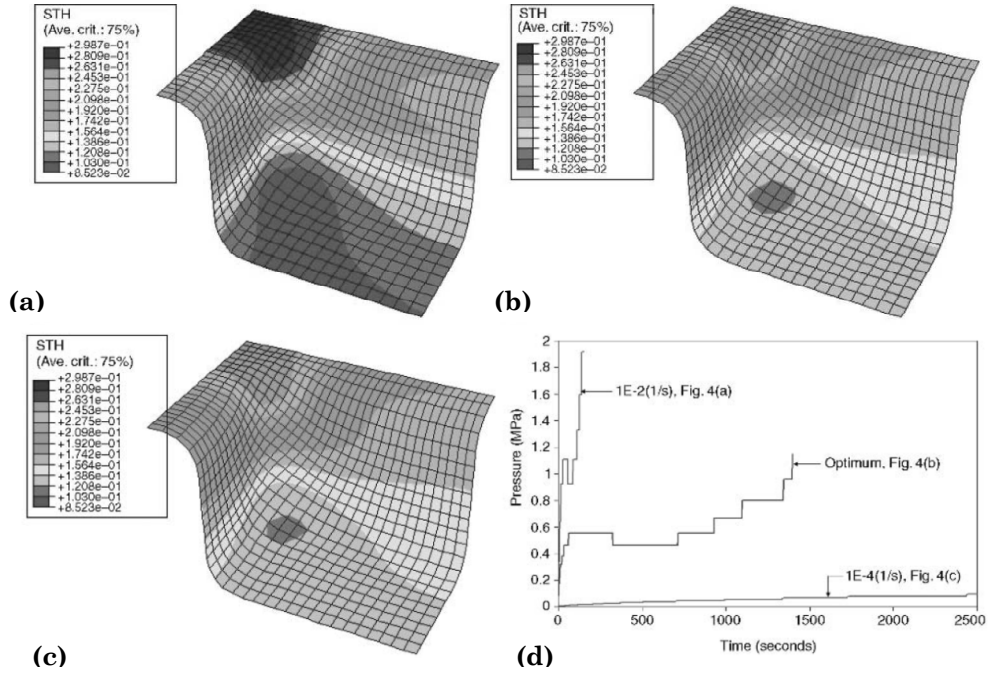


Figure 2.15.: Different pressure distribution profiles and pressure-time curves for three forming control strategies [Naz04]

2.8 Closure

In this chapter some background for understanding superplasticity and superplastic forming was explained. It was shown that superplasticity involves unique inelastic strain behaviour and allows to form geometrically complex parts in materials with low room and warm temperature formability.

Some main mechanisms were explained as general understanding of the phenomenon and the mechanical behaviour of superplastic materials. Low strain rate was shown as one of the most important characteristics the superplastic state. Similarly, these mechanisms show the importance of the grain growth and that some superplastic materials are expected to develop a void nucleation, growth and coalescence.

Furthermore, the mechanical behaviour of these materials was described, as the superplastic strain range can be very narrow and its positive determination was necessary for its full exploitation. Different constitutive equations were presented, which can be divided in physical and mechanical constitutive equations. The first ones contain more theoretical meaning, but the second ones are more efficient in order to simulate the full process and complex geometrical parts.

Different commercial superplastic alloys were presented, being titanium and aluminium alloys the most important ones in the industry. These materials were developed together with the different SPF variants to fulfil the requirements of the industrial needs of high value added, complex shaped parts. Some examples of current industrial applications have been presented, showing that this technique was categorized in productions involving expensive and exclusive products.

Finally, an almost indispensable use of finite element method in the development of SPF parts was highlighted. According to different researchers, the optimization of the SPF processes, where low strain rates are involved, can be tackled by using more efficient and dedicated FEM approaches.

CHAPTER 3

SPF MATERIAL CHARACTERIZATION

Synopsis

The accuracy of finite element analysis is directly involved with the precision of the material constitutive equations. In order to extract the proper values of the equations parameters, uniaxial tensile testing is the most common and simplest testing procedure for this aim.

One of the most valuable data of this chapter is a comprehensive characterization of the mechanical behaviour linked to the microstructure evolution of the Al-5083-SPF aluminium alloy.

Other important concept that has arisen in this chapter is the appearance of discrepancies of the different lengths obtained by the direct measurement of the specimens and the calculated ones by calculating from the cross-head position of the test machine. These inconsistencies reveal the need of other methods to obtain data for the achievement of the accurate constitutive model.

3.1 Introduction

The accuracy of finite element analysis is directly involved with the precision of the material constitutive equations. In order to extract the proper values of the equations parameters, non-complex experiments are necessary to characterize the mechanical response of the material. Uniaxial tensile testing is the most common and simplest testing procedure for this aim.

In the first part of this chapter, the methodology followed in the uniaxial tensile tests of the aluminium Al-5083 is explained. Three different tensile test procedures are explained, which are necessary to obtain the different data needed for superplastic characterization. The specimen and clamps geometry is defined and the thermal issues involving these procedures are analyzed.

The second part deals with the post-tensile tests specimen analysis of the material. This analysis is selected to have additional data for the development of constitutive equations with material mechanism information.

The results are displayed in the third part of the chapter. First of all an optimum temperature for superplastic forming is selected, and then the tensile superplastic behaviour of aforementioned material is characterized at four different strain rates. Moreover, the grain size and void fraction behaviours are observed at these strain rates.

Finally, a discussion about the inconsistencies due to assumptions used to calculate true stress – true strain curves are presented, and the used solution to avoid the subsequent errors is briefly explained.

3.2 Uniaxial tensile test methodology

Uniaxial tests for the characterization of superplastic materials are used to obtain a comprehensive data for identify SPF properties. In general, three different types of tensile tests can be carried out for the consecution of this work. The first tests are to obtain the basic mechanical superplastic properties, which are the stress – strain curves. The second ones are completed to achieve the derived superplastic properties, the so-called strain rate sensitivity m . The last tests are carried out to obtain the microstructural properties of the SPF materials.

Unfortunately, the simplicity of the tensile test becomes more complex when we are performing tests at elevated temperature, and several issues must be taken into account. Some of them are irrelevant at room temperature tests, but become inevitably significant at high temperature tests.

Although there are different standards related to uniaxial testing of superplastic alloys [Jis02, Ast06, Iso07], they do not provide enough guidelines on the selection of the best test procedures and on how to account for the aforementioned issues when testing superplastic materials. Some authors have tried to limit some of these concerns, but in general there is a lack of standardized methods for avoiding inconsistency in the published data by different authors, making them impossible to compare against other researchers data.

Other important problems of SPF tensile test standards are some assumptions related to strain and strain rate control. Actually, the most significant one is the supposition of thinking that it is possible to control the strain with the machines cross-head position, having this assumption a severe effect in the calculation of the strain rate, a particularly important parameter in SPF.

In this section, some procedures and issues of high temperature superplastic tensile testing are highlighted. These issues explain the tensile test procedure followed for the consecution of the work presented in this document, and the main issues that must be taken into account for the testing of superplastic alloys, apart from the ones explained by the previously mentioned standards. The discussed topics are:

- Tensile test procedures
- Specimen's and clamp's geometry issues
- Strain and strain rate measure and control issues
- Heating issues

3.2.1 Tested material

Al 5083-SPF is a relatively new solid solution strengthened alloy for superplastic forming application, and in this case, it was obtained from Sky Aluminum, in Japan, with the commercial name Alnovi-1. The nominal chemical compositions are shown in Table 3.1.

Table 3.1. Chemical composition of Al 5083 alloy (wt. %)

Mg	Mn	Cr	Fe	Si	Ti	Al
4.70	0.65	0.13	0.04	0.04	0.03	bal

3.2.2 Tensile test procedures

The equipment used to conduct the tensile tests presented in this document is the SERVOSIS ME 405/10 universal load frame equipped with an elliptical quartz lamp heating furnace. A 10 KN load cell INTERFACE 1210/10KN was used thorough this work for elevated temperature testing. For the acquisition and control of the clamps movement SERVOSIS PCD 1065-W program was used.

The tensile test presented in this document can be divided into three different groups:

- Controlled strain rate tests
- Jump tests
- Interrupted test

Firstly, tensile tests until fracture at different controlled strain rate provide information concerning the stress-strain behaviour at different strain rates. With jump tests, the strain rate sensitivity m value is intended to achieve for different strain rate and strain values. Finally, the interrupted tests provide information of the grain size and void volume fraction with respect to the plastic strain and strain rate.

Controlled strain rate tests

The controlled strain rate tests are mainly executed to obtain data to characterize the mechanical behaviour of the material and are used to fit the materials constitutive equations parameters. They are usually carried out at different temperature and different strain rates to characterize a wide range of superplastic behaviour of the material. Other important use of these kind of tests is the determination of the superplastic elongation of tensile tests up to fracture.

As explained before, one of the most important parameters in superplastic forming is the strain rate of the material. For applying different strain rates within the specimens, two different strategies can be followed. The first one is using a constant cross-head velocity, where the specimen will have a higher strain rate in the beginning of the test and the strain rate will decrease as test procedure continues. The second one is controlling the strain rate of the specimen by means of changing the cross-head velocity, attempting to maintain a constant strain rate during all the test.

The strategy of changing the cross-head velocity was followed in this work, as it is more intuitive for determining the most adequate forming conditions in industry. Moreover, the measurement of the strain cannot be made using extensometers because of the great strains achieved in this state, and consequently it is made using the cross-head movement as reference.

The cross-head velocity used in the tensile tests that appear in this work was calculated using the next equation, as it is used in ASTM E2448 [Ast06]:

$$V_{cross} = \dot{\epsilon}(l_0(1 + e)) \quad (3.1)$$

$$e = \left(\frac{l-l_0}{l_0}\right) \quad (3.2)$$

The movement of the clamps was governed using these equations for each tensile test presented in this document, the controlled strain rate tests, the jump tests and the interrupted tests. Subsequently it was observed that the assumptions made for defining the cross-head velocity V_{cross} induces to some errors that are no negligible. This is going to be analyzed more carefully in this chapter in the section 3.5 Discussion.

Jump tests

Jump tests are a special form of controlled strain rate tensile tests, specifically developed for obtaining the strain rate sensitivity index m of the material. There are different ways for obtaining m strain rate sensitivity value, as the one proposed by the standards BS ISO 20032:2007 [Iso07] and JIS H7501 [Jis02], but the jump test method provides a solution for the measurement having the same microstructure of the material at different strain values [AST06].

The test is conducted maintaining an initial controlled strain rate $\dot{\epsilon}_1$ up to a certain strain value, and then the strain rate is suddenly increased to $\dot{\epsilon}_2$, to go back to strain rate $\dot{\epsilon}_1$ to start the cycle again (Figure 3.1). Using this method the stress will change from σ_{i1} to σ_{i2} . By definition, the strain rate sensitivity index reflects the sensitivity of flow stress to strain rate and for jump-tests it is calculated using the next equation:

$$m_i = \frac{\log \sigma_{i2} - \log \sigma_{i1}}{\log \dot{\epsilon}_2 - \log \dot{\epsilon}_1} \quad (3.3)$$

Since m is evaluated between two strain rates, its value is assigned to the slower strain rate in some cases and the average of the two strain rate took place in others. The smaller the strain rate jump, the more precise m value is, although the size of the jump is limited by the accuracy of the load cell.

Using this kind of tests, it is possible to determine how the value of m varies for different strain values (the value where the jump is made) and strain rates.

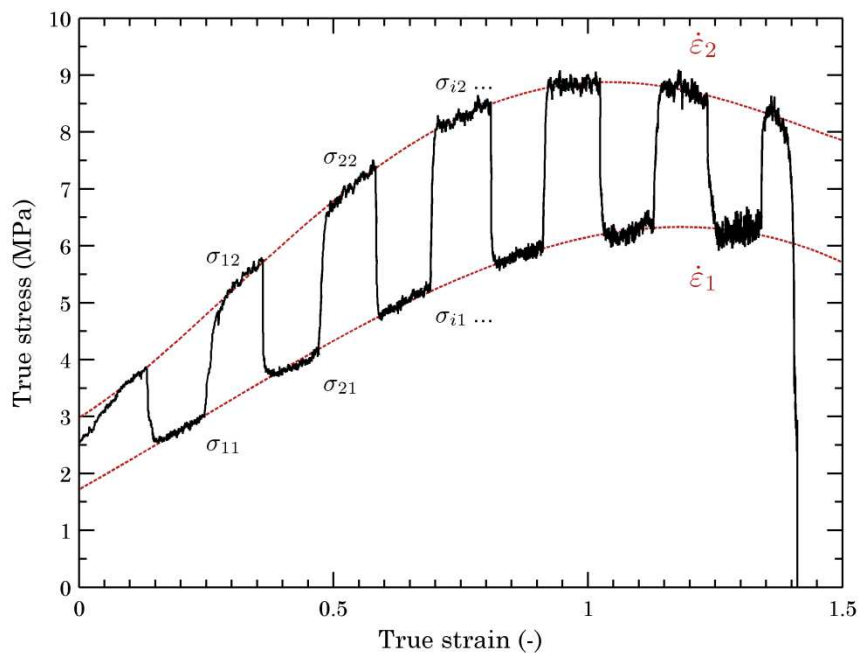


Figure 3.1.: Example of a jump tests and the obtaining of the different stress values.

Interrupted tests

The interrupted tests are usually conducted for obtaining different data of the specimen geometry and material at certain values of strain rate. This procedure is adopted due to the impossibility of an *in-situ* measuring of strain and strain rate, grain size evolution and void fraction evolution. Therefore, different tests were carried out at diverse strain rates like the controlled strain rate test, but interrupting then at some strain values (Figure 3.2). Later, this specimens will be analysed with different microscopes and measuring techniques.

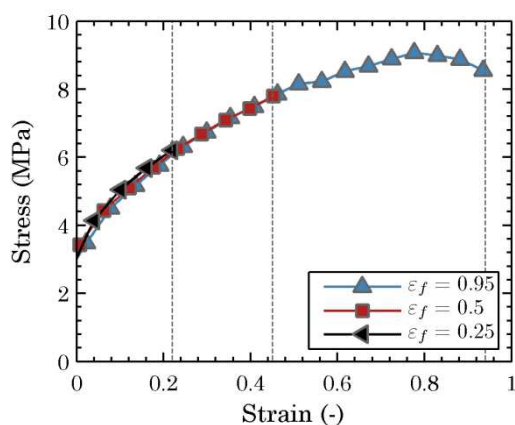


Figure 3.2: Interrupted test for three different strain values at the same strain rate.

The post-tensile test characterization methodology conducted in this work was focused in three main areas:

- Geometrical measurement of the strain values, to determine the validity of the strain measurements by the use of cross-head position and the validity of the constant strain rate equation 3.1
- Grain size measurement, to establish the evolution of the grain size depending on the strain, strain rate and time.
- Void fraction measurement, to determine the evolution of the cavitation within the material depending on strain and strain rate (equation 3.1).

3.2.3 Specimen and clamps geometry

Specimen geometry

The most relevant dimensions that should be taken into account for the design of a high temperature superplastic tensile test are the gauge length l_0 , the gauge wide w_0 , the sheet thickness t_0 and the fillet radius r_0 .

The gauge length of the specimen is largely dependent on the furnace and the temperature homogeneity needed in the test. The length of the effective zone must be determined taking into account a compromise between the dimensions of the furnace and the maximum reachable elongation. Furthermore, the gauge length of the specimen is important for the calculation of the movement of the clamps of the tensile test machine. The effective length of the employed test specimen is 6 mm (see Figure 3.3).

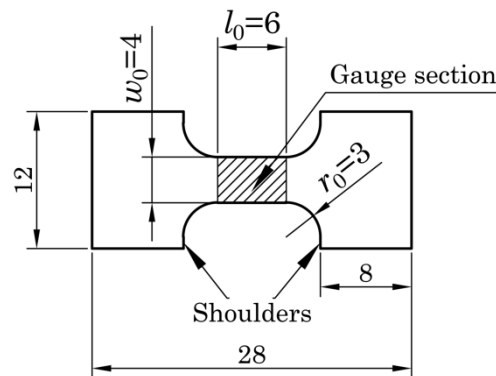


Figure 3.3.: Tensile specimen geometry used for the high temperature tensile tests.

As mentioned before, other important dimensions are the gauge wide and the sheet thickness, which in this case are 4 mm and 1.5 mm respectively. The gauge wide and the sheet thickness determine the initial cross-sectional area of the test piece and those two are essential to establish the load cell used in the test.

The last important characteristic dimension is the fillet radius, which is copied from the fillet radius of the clamps, which is 3 mm. Having a fillet radius as small as possible could be

interesting for high temperature superplastic tests, but this modification should be made in the fillet radius of the clamps too.

Clamps geometry

The clamps configuration and geometry is as important as the specimen geometry in high temperature superplastic forming tests. The high strains and the low resistance of the superplastic materials lead to a deformation and flow of the material in the test specimen heads at high temperatures.

This effect influences the accuracy of using the equation (1.1) for determining the clamps cross-head velocity, so should be avoided as much as possible. The standard clamps use two sliding wedge-shaped grip inserts that apply pressure on the surface of the specimen heads. This method of gripping is valid for cold and warm temperature tests, but leads to several errors for strain rate calculation, like the slippage of the specimen and the material flow of the shoulders of the specimen heads.

Instead of using standard clamps for elevated temperature, cavity clamps were selected to try to avoid the slippage and the deformation and flow of the head's material. The cavity clamps used for this work have a groove with the geometry of the specimen heads as can be seen in Figure 3.4. Using this kind of clamps, the deformation and flow of the specimen heads is restricted, and the force is imposed from the shoulders of the heads.

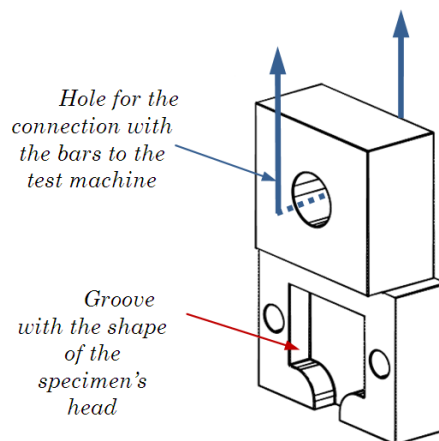


Figure 3.4: Geometry of the clamps with the cavity for the insertion of the test specimen.

3.2.4 Heating of the specimens

As was mentioned in Chapter 2, superplastic state is only observable at certain temperature in the superplastic alloys. In most of the cases, the required temperature is higher than a half of the melting temperature of the superplastic alloy [Pil89]. This circumstance leads to high testing and forming temperature, being around 500 °C for Al-

5083-SPF [Kul05,Kha98] aluminium alloy and around 925 °C for Ti6Al4V titanium alloy [Pil89, Zho96, Kim97].

Moreover, the superplastic temperature range is narrow and little variations of temperature from one point of the material to another can induce considerable disparities in the material behaviour of the same test piece.

The issues related to the heating of the specimen are linked mainly to problems because of the thermal expansion of the clamps and the specimen, and the microstructural changes in the specimen material.

Thermal expansion

The thermal expansion can be a major problem in a high temperature tensile test, since materials with different expansion coefficient are involved in this procedure. One of the most important issues to take into consideration is the expansion of the specimen. Few investigators heat the set up (clamps and bars inside the chamber of the furnace) first, and then insert and clamp the specimen when the required test temperature is achieved in the chamber. However, this method is impractical because of the manipulation of the clamps and bars at high temperature.

The most common method is clamping the specimen before heating all the set up. This leads to a risk of preload or tensile the specimen because dimension change can impose a force during the heating and cooling stages. Therefore, the specimen should be protected from this effect, to avoid a non-desired pre-strain, moving the cross-head when the temperature of the set up is varying.

In an approach to tackle this issue for the current work, a manual control of the movement of the cross-head was made maintaining the load cell response to less than ± 0.2 N value. Some tensile test machines have a “protect specimen” control option for doing it automatically, but there is no need to do so since the halogen furnace allows reaching the required temperature of the specimen, the clamps and the bars in less than 5 minutes.

Microstructural changes in the material

As just mentioned, it is expected to achieve good temperature homogeneity in the test specimen because of the differences of the material behaviour in a narrow variation of the temperature. This is obtained maintaining the temperature of the furnace a period after the heating of the chamber, called holding time. The larger is the holding time, the more homogenous is the temperature difference in the specimen.

On the contrary, there is a non-desirable effect in maintaining the holding time. This happens due to the microstructural changes that the material suffers from. As it was mentioned in the Chapter 2, one of the main microstructural parameters, the grain size,

grows statically in a environment of high temperature. The growth of the grain size is undesirable, as the superplastic properties of the material are lowered.

Consequently, some compromise should be tried to reach between the temperature homogeneity and the microstructural changes of the material in order to decide the holding time amount of the test. The different standards propose diverse solutions for this holding time. The ASTM E2448 [Ast06] points to the more general standard ASTM E21 [Ast03] for high temperature testing. According to the E21, a holding time of no less than 20 minutes is required for thermal equilibrium, without any reference to the material, the testing temperature or the type of furnace. The standard JIS H7501 [Jis02] left the selection of the heating and holding times for the interested parties to agree on. On the contrary, the standard BS ISO 20032:2007 [Iso07] does not suggest any holding time. Instead of that, maximum temperature ranges are proposed for different temperatures: for example between 200 °C and 500 °C, this range is ± 3 °C.

In conclusion, and based on the differences between the resistance and halogen furnaces, the necessary holding time to reach thermal equilibrium was defined as the time needed for the load cell perceive any signal changes. According to this definition, the heating time and holding time for Al-5083-SPF aluminium alloy specimens was measured and was imposed to 5 minutes and 10 minutes respectively.

3.3 Post -tensile test characterization methodology

The interrupted test mentioned in the previous sections should be analyzed in a laboratory in order to acquire the needed data for their characterization. Three different post-tensile test analysis were carried out during this work: a geometrical measurement, a grain size measurement and void area fraction measurement,

3.3.1 Geometrical measurement of the strain values

The measurement of the specimens was conducted using a WILD M-420 microscope with a Kappa colour camera CS-11 DSP.

Although the first purpose was to define the each strain value using the clamps position, the geometries of the tested specimen were made to contrast if this value could be accepted. With this aim different measurements of the nine strained specimens were fulfilled.

Strain and strain rate measurement according to different standards

The available standards for superplastic tensile tests procedures do not provide extensive information for the accomplishment of the test. The standards BS ISO 20032:2007 and JIS H7501 do not specifically talk about true stress – true strain curves, and the proposed test are conducted at constant cross-head velocity. The only reference of strain

measurement of these standards is the superplastic elongation A , which is named as the elongation at fracture in a superplastic state. The superplastic elongation is determined by the following equation:

$$A = \frac{l_u - l_0}{l_0} \cdot 100 \quad (3.4)$$

where l_u is the final gauge length at fracture and l_0 is the original gauge length. To determine the lengths, each end of the original gauge length is marked by means of fine marks or scribed lines, and the distance between the lines is measurement before and after the test. Observe that the obtained superplastic elongation value is an engineering strain and not a logarithmic strain value.

On the other hand the standard ASTM E2448 uses the movement of the cross-head to force a constant strain rate (equation 3.1), and the true stress – true strain curves are acquired using the equations of logarithmic strain:

$$\varepsilon = \ln (l/l_0) \quad (3.5)$$

$$\sigma = S (1 + e) \quad (3.6)$$

where l is instantaneous crosshead extension in each moment of the test, l_0 is the original gauge length and S and e are the engineering stress and strain. This standard remarks two basic issues about the measurement of the strain in superplastic equations [Ast06]. The equations (3.5) and (3.6) are only valid up to the point of necking or instability of cross section. Nevertheless, the standard assumes that the specimen overcomes a uniform and constant neck along its length for superplastic deformation. It is also mentioned that as there is an absence of available extensometers that could be operate in the high temperature environment of a superplastic test, there is no other approach to conclude the strain and stress apart from using the cross-head extension.

However, according to the standard, at the junction of the clamp section of the specimen to the gauge cross section (a radius of 1.5 mm for this standard) there is a reduction of 4 % at each end. This contributes to an error in the calculated values of strain and stress.

Measured lengths

Different lengths were measured to verify the validity of the assumptions made to convert the force – distance curves to true stress – true strain curves. The Figure 3.5 schematically illustrates the different distances measured using the microscope.

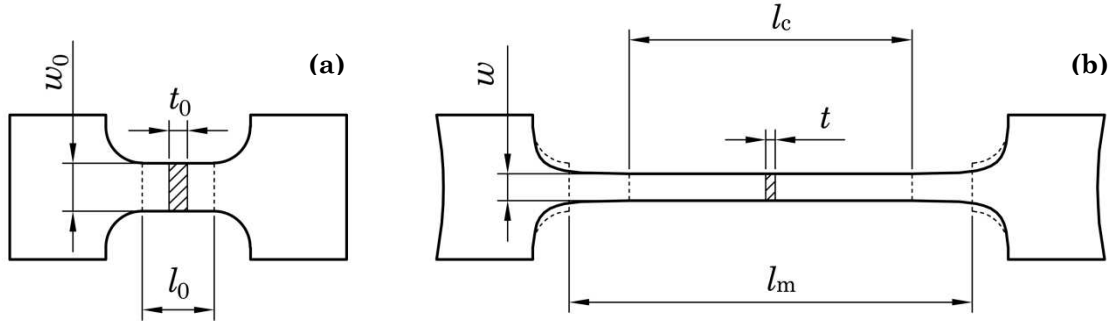


Figure 3.5: Specimens illustration before (a) and after (b) the tensile test and the measured lengths.

Before the test all the interrupted specimens gauge length l_0 , the gauge wide w_0 , the sheet thickness t_0 were measured. After the test, the measured length l_m (the distance between the shoulders of the specimen minus the fillet radius) was obtained. It should be emphasized that the correct length to measure would be the parallel length l_c (the measured length between the parallel portion of the reduced section of the test specimen), but is impossible to determine the initial length corresponding to this length. Therefore, the thickness and the wide of the reduced section were measured.

As some distances cannot be compared directly, the strains ε_m and ε_s are calculated as it is explained in the next equations:

$$\varepsilon_m = \ln (l_m/l_0) \quad (3.7)$$

$$s_0 = w_0 \cdot t_0 \quad (3.8)$$

$$s = w \cdot t \quad (3.9)$$

$$\varepsilon_s = \ln (s_0/s) \quad (3.10)$$

3.3.2 Grain size measurement

Optical micrographs were obtained in the middle of the specimens in order to compare the deformation behaviour of the material at different strain rate and strain values. The sample preparation consist on embedding the sectioned specimens in resin, grinding them up to 1200 grit SiC paper and final polishing with 1 μm silica colloidal suspension.

After polishing, the specimens were chemically etched in order to be analyzed in an optical microscope (Leica MeF-3) equipped with picture measurement software (Leica IM50 v4.0 Release 131). To detect grain size the specimens were electro-etched using Barker's etching reagent (5 ml HBF₄ + 100 ml distilled H₂O) at 27,5 V for 4-10 s and the surface was analyzed with polarized light.

3.3.3 Void area fraction measurement

To reveal the voids of the material the same sample preparation as the one used in the grain size measurement was conducted, but in this case, the optical micrographs were obtained in different areas to pick the most damaged zone. The samples were directly observed (without etching) under the optical microscope Leica MeF-3 and were analyzed with the software Leica Materials Workstation v3.4.

Although different void parameters could be analyzed in a superplastic deformation process, in this work all the efforts are focused in the void fraction determination. In theory the void area fraction is the ratio between the void area S_f and the total area S_t :

$$f_a = S_f/S_t \quad (3.11)$$

To determine its value, different micrographs were used comparing the amount of cavity pixels to the total amount of pixels. The ratio of the two numbers is the void area fraction f_a .

The void volume fraction has a relationship on the void area fraction assuming that the void area fraction is independent to on the orientation of the observed plane:

$$\sqrt{1 - f_a} = \sqrt[3]{1 - f_v} \quad (3.12)$$

3.4 Tensile test results

In the next section, the results obtained from each tensile test group are going to be presented and discussed. Note that the results are not displayed in true stress – true strain form, as it was found that in high temperature superplastic tensile tests there are effects that are not negligible, so it is incorrect obtaining the true stress and the true strain values in the traditional way. This issue is going to be more extensively discussed in the section 3.5, and the curves with true stress – true strain will be presented in the Chapter 4.

3.4.1 Controlled strain rate tests

Firstly, different temperature test were carried out at 450°C, 475 °C, 500 °C and 525 °C. The temperature with the highest enlargement value turned out to be the test at 500°C for strain rates at 2×10^{-4} , 5×10^{-4} and 1×10^{-3} (Figure 3.6).

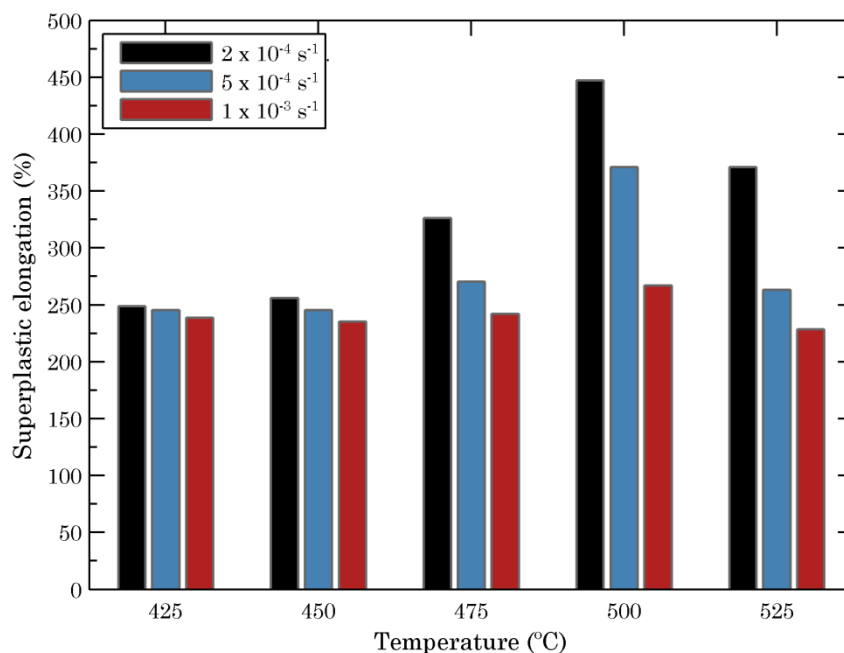


Figure 3.6: Superplastic elongation of AlNOVI-1 alloy at different temperatures and strain rates.

It has been seen that generally the strain rate sensitivity is maximum at certain temperature, which becomes in a reduction on the necking behaviour [Pil89] and on the contrary, the cavitation damage accumulation increases with decreasing temperature in Al-5083-SPF aluminium alloy [Ver96]. Due to this response of the material and the nature of the SPF processes, which are generally isothermal to ensure a high homogeneity of temperature, the selection of the optimum temperature was complex and was determined to be the temperature in which the material obtains the maximum elongation.

Afterwards, controlled strain rate tests were performed at four different strain rates at a temperature of 500 °C, following the procedure explained in the section 3.2. This material is supposed to have an isotropic behaviour at high temperature tensile testing, as Snipped and Meinders [Sni10] measured, being absolute amount of anisotropy ΔR value smaller than 0.005. Due to this isotropic behaviour, only one direction was used for these tensile tests, the 0° or RD oriented specimen. It must be remarked that it has been detected some induced anisotropy when tested ALNOVI-1 [Sni11], but this anisotropy is significant only when the cavitation value is high.

The set of results for four controlled strain rates are displaced in the Figure 3.7. An evident observation is that the forces are very low compared to results usually obtained in tensile tests on aluminium specimens. Moreover, the displacement compared to the gauge length l_0 is very high too. What is more, the high strain rate sensitivity is appreciable since there is a big difference between the forces among the different strain rates.

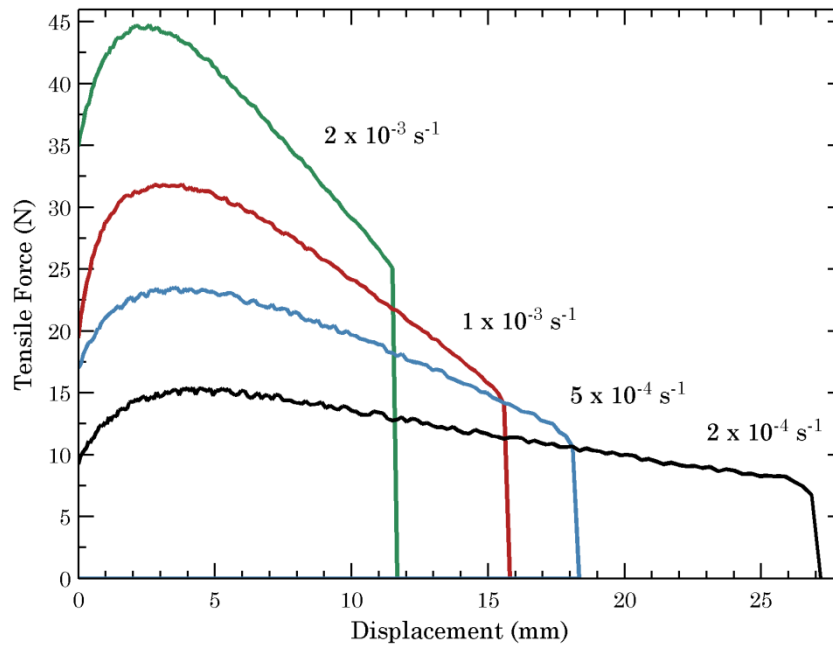


Figure 3.7: Tensile force – displacement curves for various strain rates at 500 °C.

In the Figure 3.8 the specimens at different strain rates after fracture can be seen.

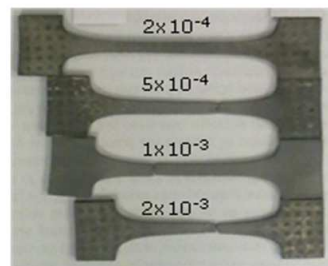


Figure 3.8: Specimens obtained at different controlled strain rates at 500 °C until fracture.

3.4.2 Jump tests

The obtained three curves for the four controlled strain rates jump-tests are displaced in the Figure 3.9. It can be seen that there is a good agreement from one to other forces for a same theoretical strain rate.

Furthermore, there is certain similitude in the fracture stress values between the three curves. The significance of the strain rate sensitivity is clear since there is a big difference between the forces among the different strain rates.

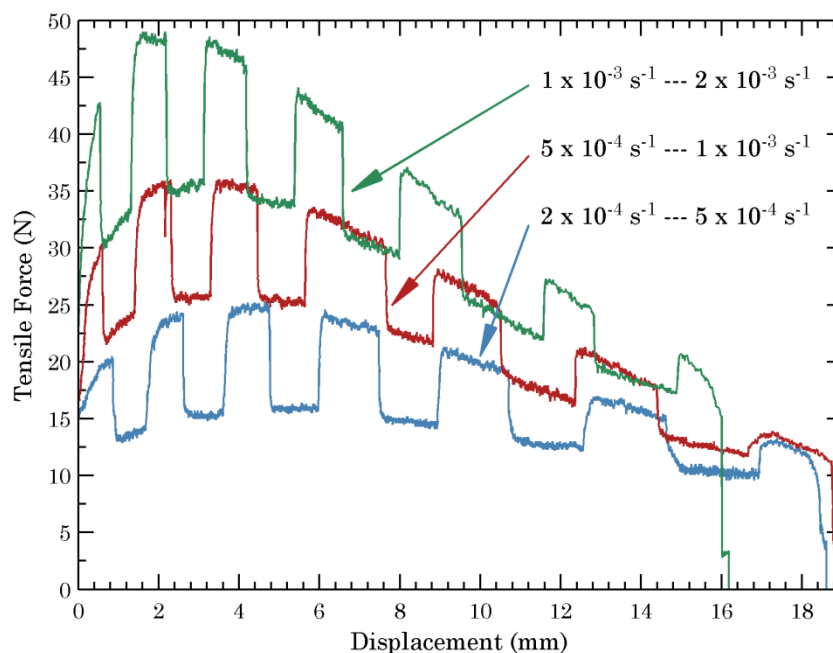


Figure 3.9: Tensile force – displacement curves for three different jump tests between 2×10^{-4} , 5×10^{-4} , 1×10^{-3} and $2 \times 10^{-3} \text{ s}^{-1}$ strain rates.

3.4.3 Interrupted tests

The specimens selected for this analysis are presented in the Table 3.2, being three different strain rates and strains analyzed.

Table 3.2. Interrupted tests carried out at different theoretical strain rates and theoretical strain values.

Specimen nº	Strain rate (s^{-1})	Strain (-)
1	2×10^{-4}	0.7
2	2×10^{-4}	1.2
3	2×10^{-4}	1.7
4	5×10^{-4}	0.3
5	5×10^{-4}	0.8
6	5×10^{-4}	1.3
7	1×10^{-3}	0.5
8	1×10^{-3}	0.8
9	1×10^{-3}	1.1

In the next sections the results of the geometrical measurement of the interrupted tests' specimens, the grain size evolution and the void fraction evolution will be presented.

Geometrical measurement of the strain values

The results of the different two strains appear in Figure 3.10. As can be seen in the Figure 3.10 (a) graph, the strain calculated by the movement of the cross-head and the measured between the two heads of the specimens are in good agreement. This is an indicative of the acceptable accuracy of the machine cross-head control

On the other hand, the Figure 3.10 graphs (b) shows large discrepancies between the different strains, with a clear the disagreement between the calculated from measured longitudinal strain ϵ_m and sectional stress ϵ_s .

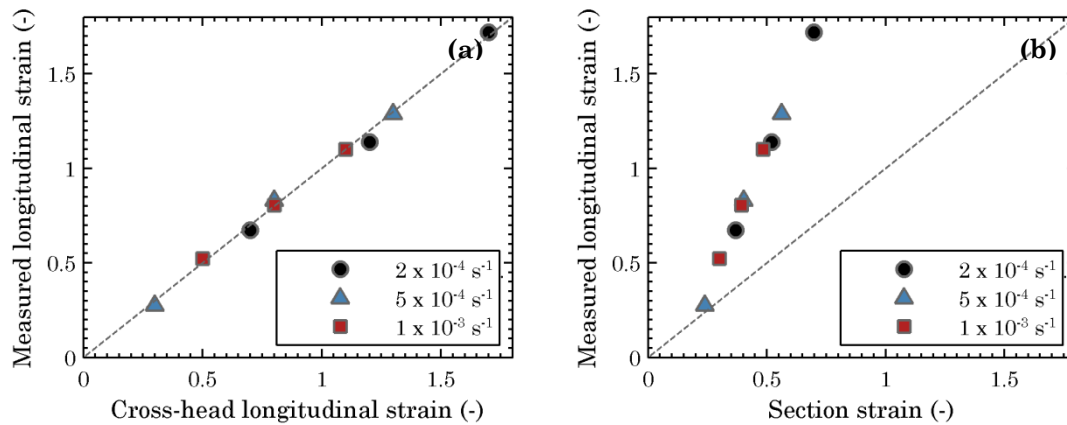


Figure 3.10: Comparison of the different strains. (a) measured longitudinal strain ϵ_m against cross-head longitudinal strain and (b) measured longitudinal strain ϵ_m against section strain ϵ_s .


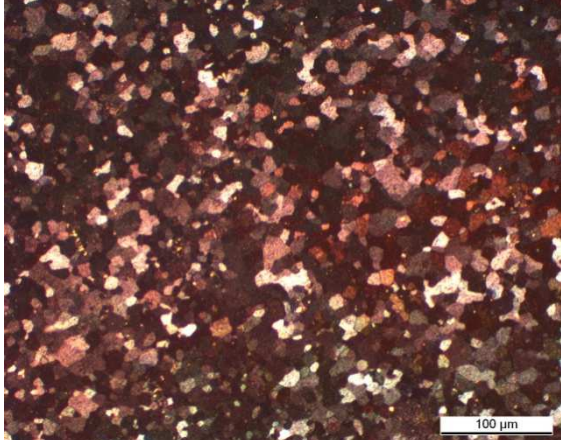
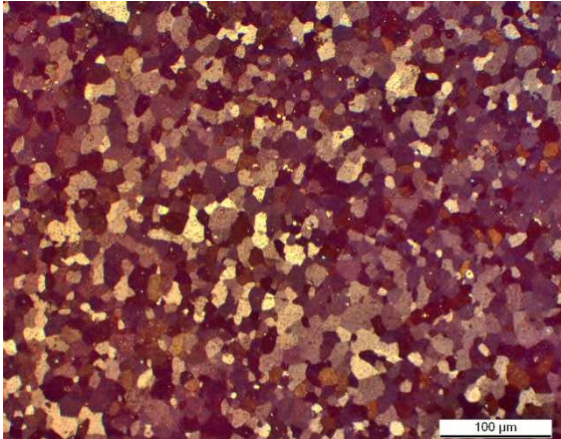
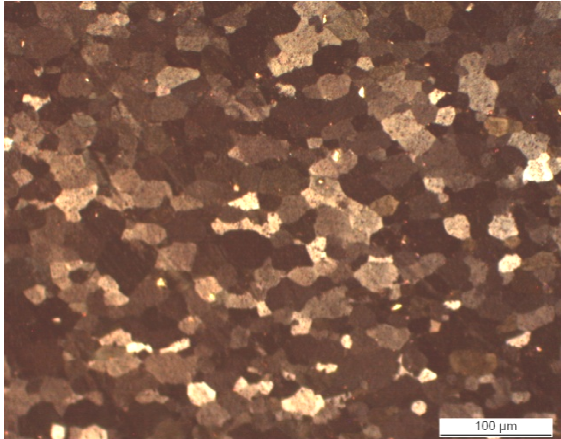
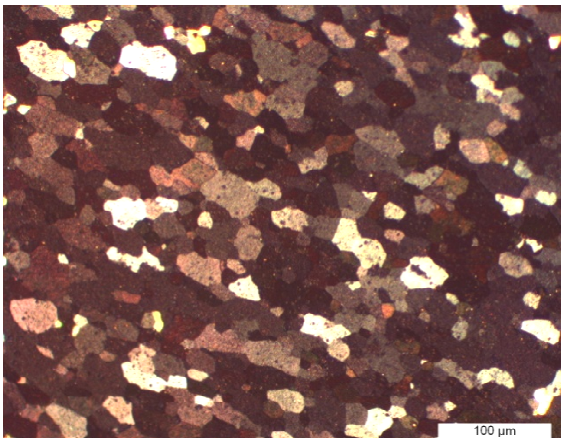
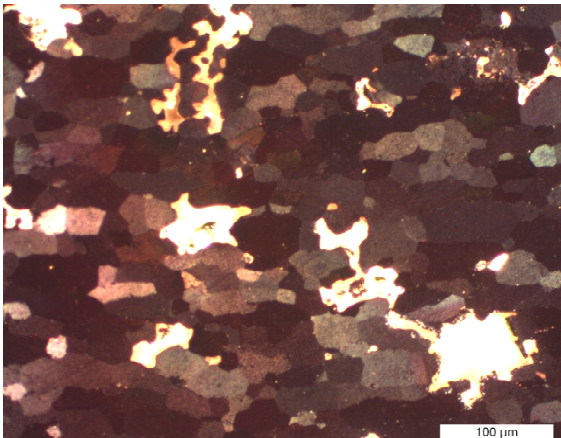
The discrepancies of the different strains obtained by the direct measurement of the specimens reveal the need of other methods for the achievement of the accurate constitutive model.

Microstructural measurement: Grain size

As explained before, grain size was measured using micrographs obtained from an optical microscope. Typical grain micrographs can be seen in Table 3.3.

In the table the grain of materials thermally treated and strained are shown. The as-received alloy shows large elongated grains with the appearance of the dendritic structure. Complete static recrystallization can be reached by heating up to 500°C to produce an equiaxed grain structure with an average grain size of $15.5 \mu\text{m}$ in only 5 minutes.

Table 3.3. Micrographs of the tensile test specimens at different conditions, electro-etched using Barker's etching reagent.

As received material	$\varepsilon = 0$ $t = 5$ min $T = 500$ °C
 <p data-bbox="703 763 751 786">100 μm</p>	 <p data-bbox="1246 763 1294 786">100 μm</p>
$\varepsilon = 0$ $t = 90$ min $T = 500$ °C	$\varepsilon_s = 0.37$ $\dot{\varepsilon} = 2 \times 10^{-4}$ min $T = 500$ °C
 <p data-bbox="663 1256 711 1279">100 μm</p>	 <p data-bbox="1246 1256 1294 1279">100 μm</p>
$\varepsilon_s = 0.52$ $\dot{\varepsilon} = 2 \times 10^{-4}$ min $T = 500$ °C	$\varepsilon_s = 0.7$ $\dot{\varepsilon} = 2 \times 10^{-4}$ min $T = 500$ °C
 <p data-bbox="663 1749 711 1771">100 μm</p>	 <p data-bbox="1246 1749 1294 1771">100 μm</p>

In opposition of the expected behaviour, no static grain growth is detected when the specimens are maintained at 500 °C in 5, 15, 30 and 90 minutes. In all these cases, the average grain size was around 15 - 16 μm , obtaining the smaller of 15.03 μm value at 90 minutes treatment specimen.

To determine the average grain growth behaviour, the graphs Figure 3.11 (a) and (b) are depicted, where the grain size values for different strain and strain rate are shown. The strain values of the graphs are the theoretical strain value or cross-head longitudinal strain (a), which is calculated from the distance between the clamps) and the sectional strain (b), which is achieved measuring the sectional area of the specimen. The decision of comparing the grain size with the two different strains was made to see if there is any difference in the interpretation of the tendency of the material.

The Figure 3.11 shows that the dynamic grain growth reveals an expected behaviour when the material is stretched, as the value of the average grain size increases when the strain value increases too.

Regarding to the effect of the strain rate, it is not clear if there is any relation between the rate the material is stretched and the grain size, although the average grain size of the $2 \times 10^{-4} \text{ s}^{-1}$ rate seems to suffer from a faster growth, as can be seen in the Figure 3.11 (b).

On the contrary, the other two rates seem to have a different tendency depending on which strain measurement is picked. In Figure 3.11 (a) the smaller the strain rate, the grain growth rate is higher. In contrast, according to the Figure 3.11 (b), the growing tendency is so similar for the different strain rate test.

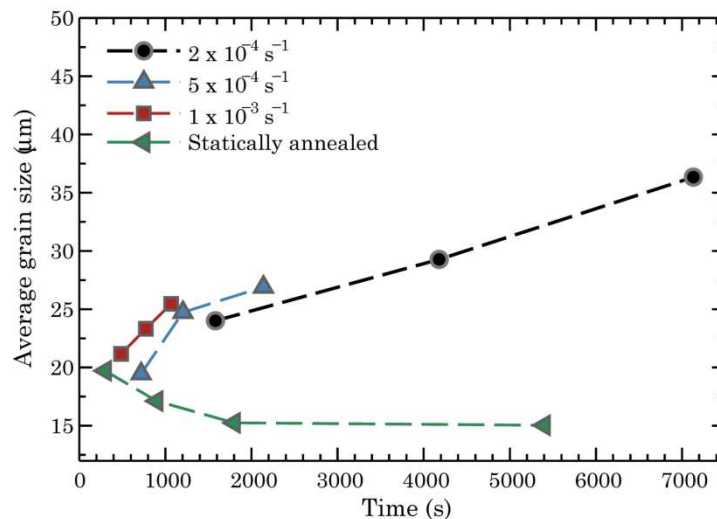
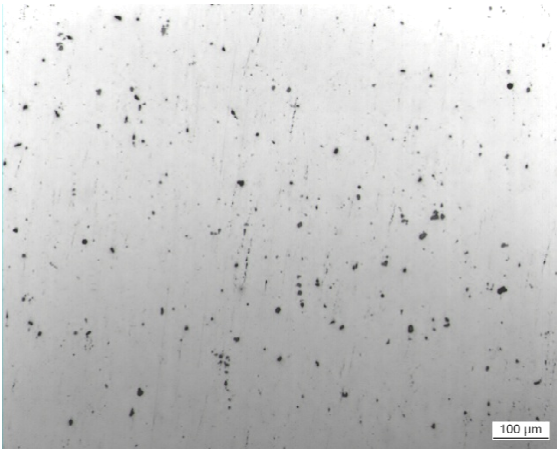
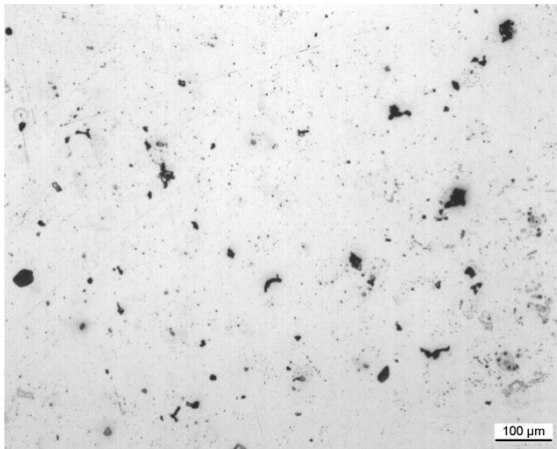
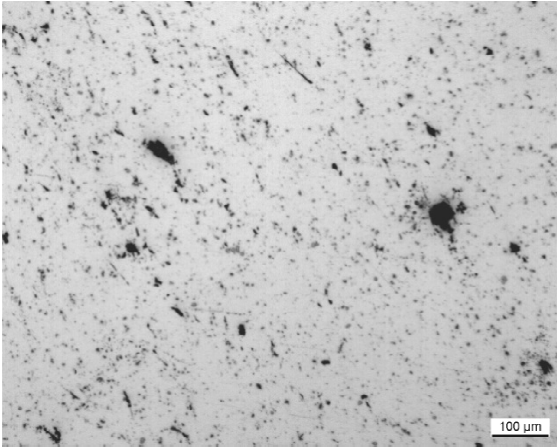


Figure 3.11: Average grain size evolution obtained from micrographs of the interrupted tests for Al-5083-SPF.

Microstructural measurement: Void volume fraction

As explained before, cavitation fraction was measured using micrographs obtained from an optical microscope. Typical cavitation micrographs can be seen in Table 3.4 , where voids of different sizes are visible and differences of the homogeneity and the distribution of the voids are noticed. Visually, it can be concluded that as the material is stretched using the same strain rate, the cavitation fraction increases.

Table 3.4. Micrographs of the polished tensile-test specimens at different conditions of strain at $2 \times 10^{-4} \text{ s}^{-1}$ strain rate.

$\epsilon_s = 0.37 \quad \dot{\epsilon} = 2 \times 10^{-4} \text{ min} \quad T = 500^\circ\text{C}$	$\epsilon_s = 0.52 \quad \dot{\epsilon} = 2 \times 10^{-4} \text{ min} \quad T = 500^\circ\text{C}$
	
$\epsilon_s = 0.7 \quad \dot{\epsilon} = 2 \times 10^{-4} \text{ min} \quad T = 500^\circ\text{C}$ 	

To determine the void volume fraction f_v evolution the Figure 3.12 is depicted, where the void fraction values for different strains and strain rates are shown.

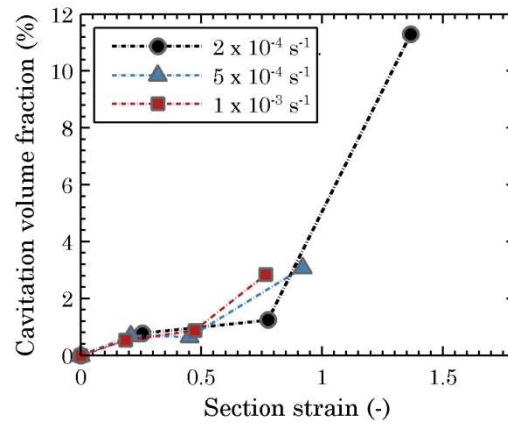


Figure 3.12: Comparison of cavitation volume fraction and the section strain obtained from micrographs of the interrupted tests.

The plotting of the cavitation volume fraction against theoretical strain value or cross-head longitudinal strain and sectional strain is used in this case too. The relation between strain and cavitation show an exponential tendency.

3.5 Closure

In this chapter tensile test data over a wide range of strain rates and temperatures is presented, being the main objective the comprehensive characterization of the mechanical behaviour linked to the microstructure evolution of the material. This was accomplished to obtain precise constitutive equation parameters of the Al-5083-SPF. Anyway, a discussion arose when the true stress - true strain were tried to calculate. The equations traditionally used for calculating the stress-strain curves make some controversial assumptions:

- there is no volume change in the material
- there is no necking
- the cross-head movement has a direct effect in the straining of the effective length of the specimen

This is assumable in ambient temperature tests, but in the high temperature superplastic tensile tests, the next effects must be taken into account:

- There is certain necking in the gauge section
- There is a straining of the specimen heads and the fillet radius
- The volume change is not zero in materials that suffer from cavitation damage
- There is some transition between the heads and the constant section length of the specimen, so the gauge losses its brick geometry during the forming although there is no necking

In the Figure 3.13 a schematic representation of the final geometry obtained in this test can be observed, with the different defeats.

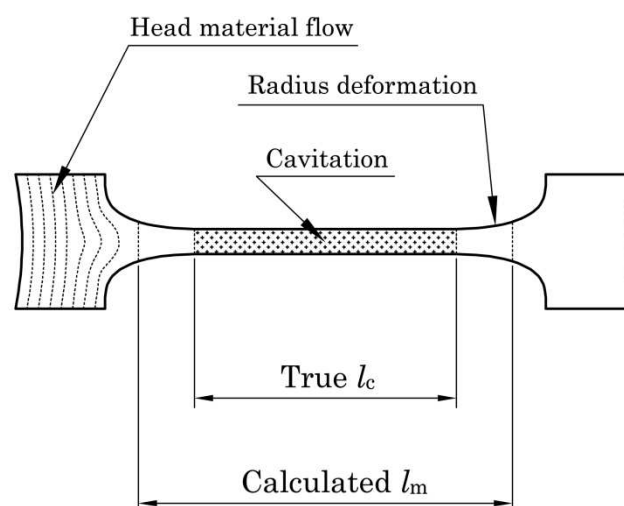


Figure 3.13.: Schematic representation of the final geometry of a superplastic alloy specimen after being stretched in a tensile test machine.

The discrepancies of the different strains obtained by the direct measurement of the specimens reveal the need of other methods to obtain data for the achievement of the accurate constitutive model. Anyway, it is observed that the used specimen geometry is not the most adequate because of the next reasons:

- The fillet radius of the specimens' should be smaller to avoid the effect of its enlargement in the total length of the specimen
- The specimens length to width ratio is too small (ratio = 1.5)

Although there are several limitations associated with the small superplastic specimens, there are also several important reasons for their use. First, superplastic behaviour is characterized by a strong dependence of the flow stress on the strain rate. This prevents the localized necking and premature failure that would otherwise occur due to the end effects at the transition from the gauge section to the head [Kha96]. Second, since total elongation is often used as a measure of superplasticity, practical limits on furnace length and total cross-head movement have limited the specimen length. Third, the low flow stress in some alloys and limits on load cell accuracy can also limit the use of smaller width specimens as a means of increasing the length-to-width ratio.

Therefore, the presented tensile tests are used to obtain uniaxial mechanical behaviour of the material and stress-strain curves have been constructed by inverse modelling using the finite elements code Abaqus in conjunction with Matlab mathematical software. This is going to be explained in the next chapter, where the material model used for this approach will be explained.

CONSTITUTIVE MODELLING OF SPF MATERIALS

Synopsis

The superplastic material behaviour involves complex mechanisms that differ from the traditional plastic behaviour. Therefore, the use of typical plastic material models can be unsuitable for superplastic forming simulation.

In this chapter, a modification of Dunne's mechanism-based constitutive equation set is proposed. The modification is mainly focused in implementing the damage behaviour for materials suffer from cavitation evolution.

On the other hand, an inverse technique has been developed to fit the modified constitutive equations, in order to obtain precise equation parameters. The comparison of the different curves shows a remarkable improvement in the accuracy of simulated tensile tests comparing to the experimental data.

4.1 Introduction

As explained before, the accuracy of finite element analysis is directly involved with the precision of the material constitutive equations. Moreover, the superplastic material behaviour involves complex mechanisms that differ from the traditional plastic behaviour. Therefore, the use of typical plastic material models can be not recommendable for superplastic forming simulation.

In addition, it has been discussed in previous chapters about the discrepancies that emerge between idealized stress – strain values and the real data. In order to extract the proper values of the equations parameters and as it was demonstrated that some assumptions could not be taken into account, the constitutive equations parameters were achieved within an iterative approach.

In the first part of this chapter, a new viscoplastic material model for voided material with variable density is presented. In order to establish the flow rule for voided materials, it was first consider the flow rule for the matrix material. Then the explanation is extended to voided viscoplastic material model with fixed density, to finish developing the voided viscoplastic material model with density variation. All the material models use mechanism-based sigmoidal constitutive equations.

In the second part of this chapter, the interactive approach to obtain more accurate model parameters is shown. Finally, the obtained parameters for voided viscoplastic material model with density variation and the comparison with the real data are shown.

4.2 Viscoplasticity model

Superplastic deformation is modelled along the framework of viscoplasticity, with almost negligible elastic strain. Then the following kinematical relationship can be used:

$$\mathbf{D}^t = \mathbf{D}^e + \mathbf{D}^{vp} \approx \mathbf{D}^{vp} \quad (4.1)$$

where \mathbf{D}^t is the strain rate tensor, \mathbf{D}^e and \mathbf{D}^{vp} are the elastic and viscoplastic parts respectively. Because creep processes may occur independently of plastic yielding, it is not appropriate to use a yield surface, in the conventional sense. Instead, a potential function is defined from which creep strain rate are determined. Due to this, for viscoplastic deformation, the general associated flow rule [Dun05] is given by:

$$\mathbf{D}^{vp} = \lambda \frac{\partial \phi}{\partial \boldsymbol{\sigma}} \quad (4.2)$$

where $\dot{\lambda}$ is the plastic multiplier, ϕ is the potential function, and $\boldsymbol{\sigma}$ is the Cauchy stress tensor.

4.2.1 Viscoplastic model for matrix material

In order to establish the flow rule for voided materials we first consider the flow rule for the matrix material (without the effect of voids). The associated flow rule is written as:

$$\mathbf{D}^{\text{vp}} = \frac{3}{2} \dot{\varepsilon}^{\text{vp}} \frac{\boldsymbol{\sigma}'}{\sigma_e} \quad (4.3)$$

$$\dot{\varepsilon}^{\text{vp}} = \sqrt{\frac{2}{3} \mathbf{D}^{\text{vp}} : \mathbf{D}^{\text{vp}}} \quad (4.4)$$

$$\boldsymbol{\sigma}' = \boldsymbol{\sigma} - \frac{1}{3} \text{Tr}(\boldsymbol{\sigma}) : \mathbf{I} \quad (4.5)$$

$$\sigma_e = \sqrt{\frac{3}{2} \boldsymbol{\sigma}' : \boldsymbol{\sigma}'} \quad (4.6)$$

where $\boldsymbol{\sigma}'$ is the deviatoric stress tensor, $\dot{\varepsilon}^{\text{vp}}$ is the viscoplastic equivalent strain rate and σ_e is the von Mises equivalent stress.

4.2.2 Mechanism based constitutive equation

According to different authors, during the high-temperature deformation of some titanium and aluminium alloys, a number of mechanisms operate [Rua88]. For a particular range of strain rate, temperature and stress, a predominant mechanism may exist. However, this is not always the case, and it is most likely that a number of mechanisms operate in parallel, sometimes in an iterative manner, sometimes not. For example, the Al5083 aluminium alloy creep behaviour is believed to be governed by the additive and independent contributions of GBS and slip creep [Per01].

From this point of view, the constitutive equations that appear in the literature can be divided in two groups: the first one are the physical ones and the second one the mechanical ones. The physical constitutive equations are developed for describing the different physical mechanisms and include microstructural parameters. The mechanical constitutive equations are in general phenomenological and are developed for describing relatively accurate macroscopic material behaviour in a simpler manner.

In this work, the selected constitutive is half way from the mechanical and physical equation set, as an unified viscoplastic mechanisms-based constitutive equation set presented by Zhou and Dunne [Zho96, Kim97, Dun05] is used. These constitutive equations are adequate for obtaining pressure-time curves for SPF parts in an uncomplicated way, but they describe important microscopic behaviour like grain size. A key advantage of the

mechanisms-based equation set is that it is valid for a wide range of strain rates and the constants are independent of strain rate.

The unified viscoplastic constitutive equations proposed by Zhou and Dunne have the following form:

$$\mathbf{D}^{\text{vp}} = \frac{3}{2} \frac{\alpha}{d^\gamma} \sinh \beta (\sigma_e - R - \sigma_y) \frac{\boldsymbol{\sigma}'}{\sigma_e} \quad (4.7)$$

$$\dot{R} = (C_1 - \gamma_1 R) \dot{\boldsymbol{\varepsilon}}^{\text{vp}} \quad (4.8)$$

$$\dot{d} = \frac{(\alpha_1 + \beta_1 \dot{\boldsymbol{\varepsilon}}^{\text{vp}})}{d^\mu} \quad (4.9)$$

$$\boldsymbol{\varepsilon}^{\text{t}} - \boldsymbol{\varepsilon}^{\text{vp}} = \frac{1}{E} \boldsymbol{\sigma} - \frac{\nu}{E} (\text{Tr}(\boldsymbol{\sigma}) \mathbf{I} - \boldsymbol{\sigma}) \quad (4.10)$$

$$\boldsymbol{\varepsilon}^{\text{vp}} = \int_0^t \mathbf{D}^{\text{vp}} dt \quad (4.11)$$

where $\boldsymbol{\varepsilon}^{\text{t}}$ and $\boldsymbol{\varepsilon}^{\text{vp}}$ are total and viscoplastic strain, d is average grain size, R is an isotropic hardening variable, σ_e is the effective von Mises stress, σ_y is the yield stress and E is young's Modulus. α , β , γ , C_1 , γ_1 , α_1 , β_1 and μ are material constants.

For low stress levels, this constitutive equation approximates to a linear relationship between the strain rate and stress, enabling diffusion controlled and grain boundary sliding (GBS) processes to be modelled. For high stress levels, the relationship becomes non-linear, reflecting the material behaviour under conditions for dislocation creep controlled deformation.

4.2.3 Damage mechanics

Since Al5083 aluminium alloy formed in superplastic conditions suffers from cavitation, a model that counts for internal degradation of the material is needed. The gradual internal deterioration at the microscopic level has an effect in the macroscopic behaviour of the material and can eventually lead to the occurrence of the macroscopic failure of the material. Furthermore, as experimentally verified by many authors, the nucleation and growth of voids and microcracks causes considerable reduction of strength [Khr07], and is highly influenced by the triaxiality of the stress state [Pil86, Pil89, Cho93].

Continuum damage mechanism (CDM)

During this work, the implementation of the material degradation was done within the framework of continuum mechanics, using the Continuum Damage Mechanics (CDM) approach. The use of the CDM for materials that degrade by void nucleation and growth

leads to an inconsistency when using the classical theories of metal plasticity, the volume change.

In CDM, the material is assumed to be a continuum body, and the effect of the damage on the deformation process is taken into account by introducing damage variables into the constitutive equations of the material. The mechanics of continuous media is characterized by the Representative Volume Element (RVE) on which all properties are represented by homogenized variables [Lem05] (see Figure 4.1).

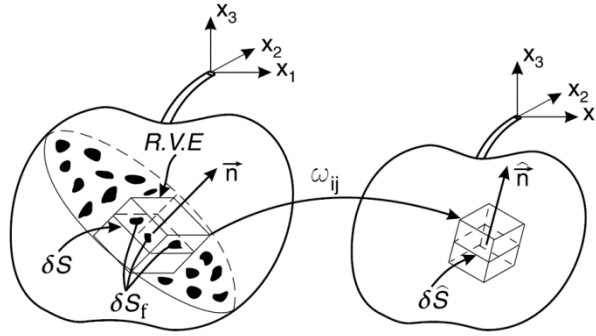


Figure 4.1.: Physical damage and mathematical continuous damage, modified from [Lem05].

Damage variable and effective stress

Considering an RVE that is enlarged considerably and voids have nucleate and grow. The variable S will be the overall sectional area defined by the normal \vec{n} . Likewise, this sectional area will have cavities and imperfections, being S_f their total area. The effective sectional area \hat{S} will be the resisting area taking into account these cavities and the microstress concentrations in the vicinity of discontinuities and the interactions between closed cavities. Therefore the effective section area can be say it is:

$$\hat{S} < S - S_f \quad (4.12)$$

The damage $\omega_{(ij)}$ will be physically represented as the corrected area of cavities per unit surface cut by a plane perpendicular to a normal vector \mathbf{n} (see Figure 4.1). The representation of the damage that takes place in a body can be represented by a variable ω , as in this case is supposed to be isotropic damage behaviour and therefore does not depend on the normal \vec{n} , being:

$$\omega = \frac{S - \hat{S}}{S} \quad (4.13)$$

In addition, the definition of damage by means of an *effective* resisting \hat{S} area leads to the definition of the so-called *effective stress* [Kac58]:

$$\hat{\sigma} = \frac{\sigma}{1 - \omega} \quad (4.14)$$

The concept of effective stress allows describing the phenomenon of internal degradation of a material in a simple manner.

Density change of the material

As can be seen in Figure 4.2, when a body suffers from cavitation damage and CDM approach is employed, the density of the formed material decreases due to the void nucleation and growth, as $abc \neq a'b'c'$ and in consequence, the initial volume V and the final volume V' are different.

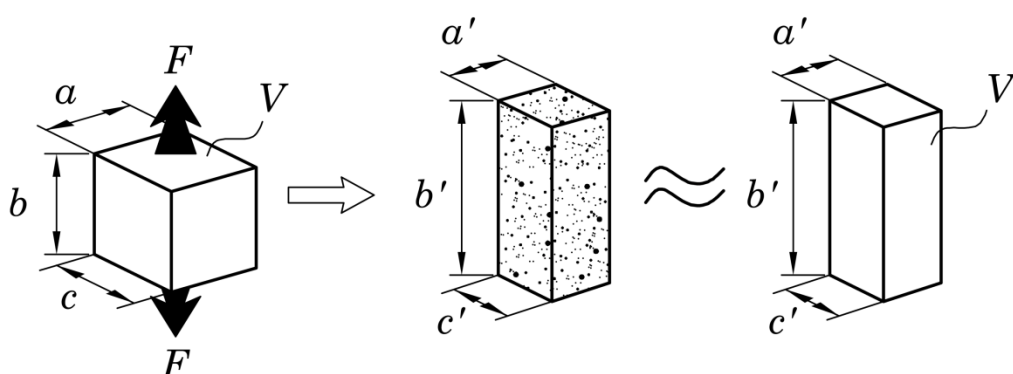


Figure 4.2.: Representation of the volume change in a uniaxially tensiled RVE body that suffers from cavitation and the approximation of this damaged body using CDM.

Because of this, if the material is represented as a continuum body with no heterogeneities, a material model with volume change capabilities should be used. Some models with this singularity exist for ductile plastic damage [Gre71, Shi75, Gur75, Per84] and for geotechnical dilatant plasticity [Reg97].

In this work, the evolution equation for the volume change is derived from the assumption that volume changes in the plastic regime are exclusively due to changes of the void volume fraction, following the law of conservation of mass [Rou86]:

$$\mathbf{D}_{\text{vol}}^{\text{vp}} = \frac{1}{3(1 - f_v)} \dot{f}_v \mathbf{I} \quad (4.15)$$

where $\mathbf{D}_{\text{vol}}^{\text{vp}}$ is the volumetric viscoplastic strain rate tensor, f_v is the cavity volume fraction.

Cavitation behaviour of the material

To specify the effective section area during the forming and in consequence the damage variable, there is a need to define cavity volume fraction f_v and cavity area fraction f_a . With this aim, the following equation set was used for accomplishing this work.

Two main mechanisms of cavitation generation are widely accepted, i.e., vacancy diffusion controlled growth and plastic deformation controlled growth. It is considered that the mechanism of plastic deformation controlled growth is dominant during most of superplastic deformations. It is found that the number of cavitation tends to increase with the increasing strain. Cavitation in superplastic materials is frequently quantified by the equation of variation with strain of the cavity area fraction f_a according to:

$$\dot{f}_a = f_{a0} \psi \exp(\psi \varepsilon^{VP}) \dot{\varepsilon}^{VP} \quad (4.16)$$

where ψ is a cavity growth parameter and f_{a0} is a fitting constant which may be defined as an initial cavity volume fraction or a propensity of cavity nucleation. Note that the equation has been modified to the rate-type equation form, comparing to the equation (2.3), which is necessary because the cavity growth parameter ψ depends on the strain rate.

The cavity growth parameter is defined according to the next equation, based on the work developed by Pilling and Ridley [Pil89] founded on the work developed by Cocks and Ashby [Coc80, Coc82], that supposes the grains sliding and the cavitation, as can be seen in Figure 4.3

$$\psi = \frac{3}{2} \left(\frac{m+1}{m} \right) \sinh \left[2 \frac{2-m}{2+m} \left(\frac{\sigma_m^\mu}{\sigma_e} \right) \right] \quad (4.17)$$

$$m = \alpha_2 + \beta_2 \ln(\dot{\varepsilon}^{VP}) \quad (4.18)$$

m is the strain rate sensitivity and the mean stress is $\sigma_m^\mu = \sigma_{kk}^\mu / 3$. The void growth parameter ψ equation [Pil89] depends on the tensional state of the material, which is described by the triaxiality, defined as the ratio between the mean stress and the von Mises stress (σ_m^μ / σ_e).

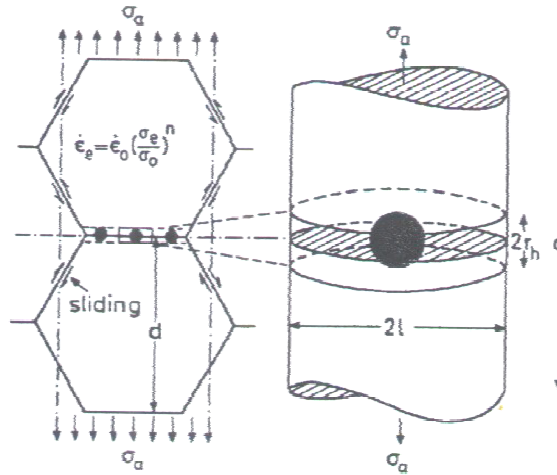


Figure 4.3.: Void grow on grain boundary for GBS [Coc80].

The reason of picking the theory based equation 4.17 presented by Cocks and Ashby is because there were not tested uniaxial test at different triaxial states due to technical limitations, and there would be a lack of data for the fitting of a phenomenological equation. Note that the actual ratio between the mean stress and the von Mises stress (σ_m^μ/σ_e) defines the triaxiality of stress localized in the grain boundary (therefore the means stress is defined with a μ symbol) and not a macro perspective.

To be able to have an equation that uses macro stress and strains, Pilling and Ridley applied the analysis made by Beeré about the stresses and deformations that are present in the grain boundaries [Bee78], obtaining the equation (2.4) presented in the chapter 2. This equation uses the next relationship:

$$\frac{\sigma_m^\mu}{\sigma_e} = \left(\frac{K_s}{3} - \frac{P_h}{\sigma_e} \right) \quad (4.19)$$

where K_s is a geometric constant (being values of $1 \leq K_s \leq 2$ for uniaxial deformation and $2 \leq K_s \leq 2.5$ for balanced biaxial deformation). P_h is the superimposed hydrostatic pressure. This method of calculating the triaxiality in the grain boundary is valuable for very specific and ideal situations, but not for complex shapes where the stress state varies throughout the different areas of the part.

For getting this geometric constant variables K_s , Pilling and Ridley used two different equations for two different situations; the equation (4.19) is for the case of no grain boundary sliding and the equation (4.20) is for the case of freely sliding grains [Pil86].

$$\frac{\sigma_m^\mu}{\sigma_e} = \frac{\sigma_m^\infty}{\sigma_e} \quad (4.20)$$

$$\frac{\sigma_m^\mu}{\sigma_e} = \frac{1}{2} \left(\frac{\sigma_1^\infty}{\sigma_e} - \frac{\sigma_m^\infty}{\sigma_e} \right) \quad (4.21)$$

where σ_m^∞ is remotely applied mean stress, and σ_1^∞ is the remotely applied maximum principal stress. In [Pil86], the lower values of geometric constant K_s are for no grain boundary sliding and the higher values would be valid when the boundaries freely slide. Pilling and Ridley calculated the exact K_s values by assuming that in superplastic deformation it is believed that approx 50% of the accumulated strain is accommodated by grain boundary sliding [Cho93, Pan09]. Therefore, $K_s = 1.5$ and $K_s = 2.25$ are designed for uniaxial and biaxial deformation respectively.

Therefore, in this work the next equation is used to determine the triaxiality in the grain boundary:

$$\frac{\sigma_m^\mu}{\sigma_e} = (1 - \chi_{\text{GBS}}) \left[\frac{\sigma_m^\infty}{\sigma_e} \right] + \chi_{\text{GBS}} \left[\frac{1}{2} \left(\frac{\sigma_1^\infty}{\sigma_e} - \frac{\sigma_m^\infty}{\sigma_e} \right) \right] \quad (4.22)$$

where χ_{GBS} is the fraction of GBS strain. For this work, the value of χ_{GBS} was set to 0.5. Anyway, as it was pointed out by Bae and Ghosh [Bae02b], it is awkward having the same value of GBS contribution for materials with different m values.

4.2.4 Viscoplastic model for voided material with fixed density

The associated flow rule for this model is the same as the one for the viscoplastic model for matrix material (equations (4.3-4.6)), with a little distinction related to the effective stress, as it is assumed that the material is isotropic and obeys the von Mises flow rule according to the J_2 theory of plasticity. It is assumed that the mean stress only affects the cavitation behaviour and there is no effect in the elastic part.

In the case of the viscoplastic model for voided material with fixed material volume, the effective resisting area is usually picked to be the next one:

$$\hat{S} = S - S_f \quad (4.23)$$

where S_f is the area of the cavities inside S . Combining equation 4.13 with 4.23 and understanding that the voids area fraction $f_a = (S - S_f)/S$, it is obtained:

$$\omega = f_a \quad (4.24)$$

Therefore, the equation 4.7 was modified for implementing softening behaviour to the curves, with an area of voids fraction f_a for this purpose in:

$$\mathbf{D}^{\text{vp}} = \frac{3}{2} \frac{\alpha}{d^{\gamma}} \sinh\beta(\hat{\sigma} - R - \sigma_y) \frac{\boldsymbol{\sigma}'}{\sigma_e} \quad (4.25)$$

$$\hat{\sigma} = \frac{\sigma_e}{1 - \omega} = \frac{\sigma_e}{1 - f_a} \quad (4.26)$$

4.2.5 Viscoplastic model for voided material with density variation

The flow rule for this model is different from the previous model, as in this case the effect of the volumetric strain is implemented in the equations, to reproduce the density variation the materials suffer from. Therefore, the viscoplastic strain is divided into two different strain rate tensors, the deviatoric strain $\mathbf{D}_{\text{dev}}^{\text{vp}}$ and the volumetric strain $\mathbf{D}_{\text{vol}}^{\text{vp}}$:

$$\mathbf{D}^{\text{vp}} = \mathbf{D}_{\text{dev}}^{\text{vp}} + \mathbf{D}_{\text{vol}}^{\text{vp}} \quad (4.27)$$

In the case of the viscoplastic model for voided material with material volume change, the effective resisting area is going to differ from the one proposed for the viscoplastic model for voided material with fixed material volume:

$$\hat{S} < S - S_f \quad (4.28)$$

In this case, apart from the area of cavities, the effect of the microstress concentrations in the vicinity of discontinuities and the interaction between closed defects will be taken into account by:

$$\omega = (\alpha_3 f_a)^{\beta_3} \quad (4.29)$$

where α_3 and β_3 are parameters that depend on voids' size, shape and iteration.

The first part, the one related to the deviatoric strain, uses the next equations:

$$\mathbf{D}_{\text{dev}}^{\text{vp}} = \frac{3}{2} \frac{\alpha}{d^{\gamma}} \sinh\beta(\hat{\sigma} - R - \sigma_y) \frac{\boldsymbol{\sigma}'}{\sigma_e} \quad (4.30)$$

$$\hat{\sigma} = \frac{\sigma_e}{1 - \omega} = \frac{\sigma_e}{1 - (\alpha_3 f_a)^{\beta_3}} \quad (4.31)$$

On the other hand, the volumetric stress is obtained assuming that all the volume variation is due to the void nucleation and growth. Therefore, the equivalent volumetric strain is supposed to be the void volume fraction:

$$\mathbf{D}_{\text{vol}}^{\text{vp}} = \frac{1}{3} \dot{f}_v \mathbf{I} \quad (4.32)$$

where \hat{f}_v is the void volume fraction and \mathbf{I} is the unit matrix. Note that to get the void volume fraction value the assumption of $\sqrt{1 - \hat{f}_a} = \sqrt[3]{1 - \hat{f}_v}$, to relate the two dimensional and three dimensional fractions has been done, supposing that the void fraction is independent on the orientation of the plane. Similarly, we can say that density $\rho = \rho_0(1 - f_v)$ being ρ_0 the density of the matrix following these equations.

Finally, equations used for the viscoplastic model for voided material with density variation are summarized in Table 4.1.

Table 4.1. Summary of the equations used for the viscoplastic model for voided material with density variation.

1. Elastoplastic Split of the strain tensor

$$\mathbf{D} = \mathbf{D}^e + \mathbf{D}^{vp}$$

2. Elastic law

$$\boldsymbol{\varepsilon}^t - \boldsymbol{\varepsilon}^{vp} = \frac{1}{E} \boldsymbol{\sigma} - \frac{\nu}{E} (\text{Tr}(\boldsymbol{\sigma}) \mathbf{I} - \boldsymbol{\sigma})$$

3. Plastic flow rule

$$\mathbf{D}^{vp} = \dot{\lambda} \frac{\partial \phi}{\partial \boldsymbol{\sigma}} = \mathbf{D}_{dev}^{vp} + \mathbf{D}_{vol}^{vp}$$

4. Deviatoric viscoplastic strain rate tensor

$$\mathbf{D}_{dev}^{vp} = \frac{3}{2} \frac{\alpha}{d^{\nu}} \sinh \beta (\hat{\sigma} - R - \sigma_y) \frac{\boldsymbol{\sigma}'}{\sigma_e}$$

5. Volumetric viscoplastic strain rate tensor

$$\mathbf{D}_{vol}^{vp} = \frac{1}{3} \dot{f}_v \mathbf{I}$$

6. Isotropic strain hardening

$$\dot{R} = (C_1 - \gamma_1 R) \dot{\varepsilon}^{vp}$$

7. Average grain size evolution

$$\dot{d} = \frac{(\alpha_1 + \beta_1 \dot{\varepsilon}^{vp})}{d^{\mu}}$$

8. Effective stress using CDM

$$\hat{\sigma} = \frac{\sigma_e}{1 - \omega} = \frac{\sigma_e}{1 - (\alpha_3 f_a)^{\beta_3}}$$

9. Cavitation area fraction evolution

$$\dot{f}_a = f_{a0} \psi \exp(\psi \varepsilon^{vp}) \dot{\varepsilon}^{vp}$$

$$\psi = \frac{3}{2} \left(\frac{m+1}{m} \right) \sinh \left[2 \frac{2-m}{2+m} \frac{\sigma_m^{\mu}}{\sigma_e} \right]$$

$$m = \alpha_2 + \beta_2 \ln(\dot{\varepsilon}^{vp})$$

$$\frac{\sigma_m^{\mu}}{\sigma_e} = (1 - \chi_{GBS}) \left[\frac{\sigma_m^{\infty}}{\sigma_e} \right] + \chi_{GBS} \left[\frac{1}{2} \left(\frac{\sigma_1^{\infty}}{\sigma_e} - \frac{\sigma_m^{\infty}}{\sigma_e} \right) \right]$$

4.3 Uniaxial model fitting

In order to model the stress-strain behaviour of the material, results from material characterization (Chapter 3) were used. As it was explained before, the data shown in this chapter are force – displacement curves instead of stress – strain ones, to avoid the errors that are derived from assuming a purely uniaxial behaviour in the tensile tests and volume constancy in the material. Therefore, the only way to solve this problem was determined to be using the inverse method to obtain the viscoplastic model parameters by using an iterative technique. The stress - strain curves are constructed using the FE code Abaqus, the commercial software used for simulating the different SPF tests in this work. More information about body discretization, material parameter implementation etc. will be explained in the next chapter.

4.3.1 Inverse method development for stress – strain curve fitting

This section describes the method used to transform the force-displacement curves of the tensile experiments into stress – strain curves. Figure 4.4 shows a flow chart.

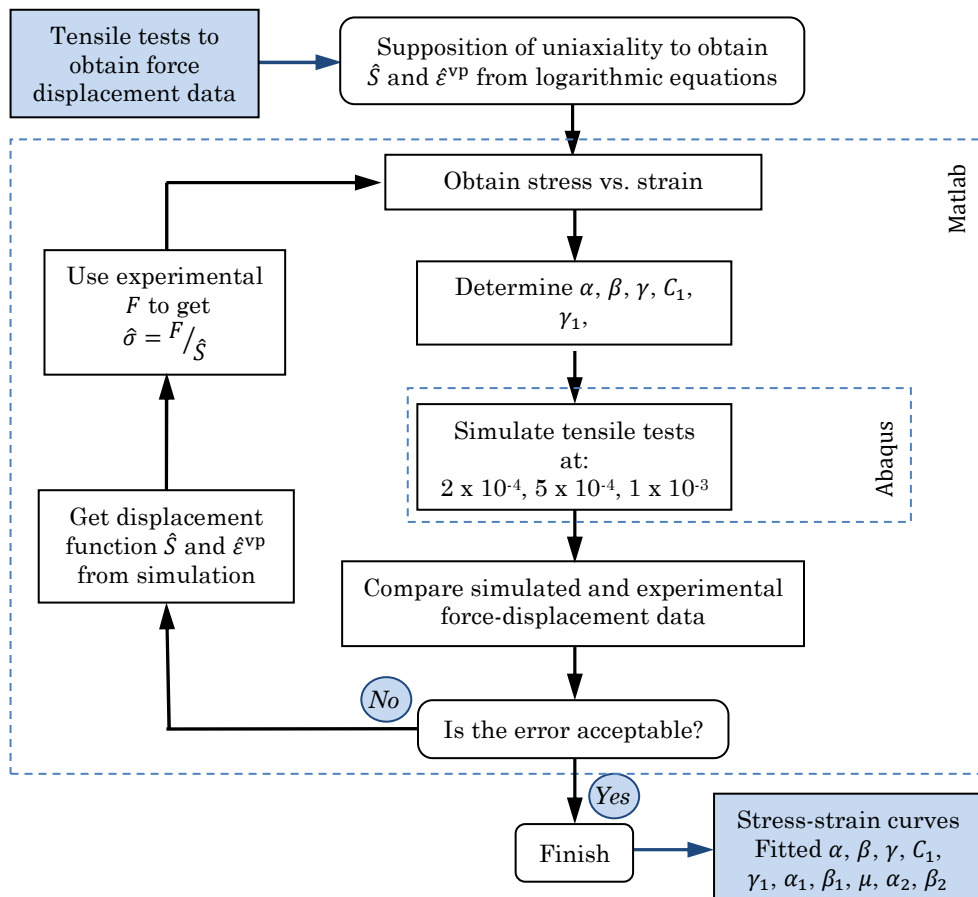


Figure 4.4.: Basic chart flow of data and actions from the start of an iterative curve fitting.

First of all, displacement data of the tensile experiment are used to estimate the current viscoplastic strain and the effective cross-sectional area \hat{S} in each increment of the test. As explained before, not all of the displacement of the cross-head can be attributed to the effective length of the specimen, but at first approach it was calculated neglecting the other behaviours.

So, \hat{S} and $\dot{\varepsilon}^{vp}$ were obtained assuming constant strain rate tests (using $V_{cross} = \dot{\varepsilon}(l_0(1 + e))$ and $\varepsilon = \ln(l/l_0)$ equations). The elongation of the effective length is used to determine plastic strain in this area. This results in the strain evolution as function of time. The stress – time and strain-time relationships are then coupled to construct stress-strain curves at different strain rates. These stress-strain curves are used to perform an inverse modelling of the tensile tests.

Once the first stress – strain curves are achieved, the parameter determination starts. A curve-fitting methodology was developed within Matlab for the identification of the constitutive parameters. To optimize the parameters, an error minimization procedure has been programmed using least square error technique. The objective function used can be written as follows:

$$F(x_K) = \sum_{j=1}^n \sum_{i=1}^p [(R_i^t)_j - (R_i^e)_j]^2 \quad (4.25)$$

Where x_K are material parameters to be optimized, R_i^t are the theoretical values of the variable to fit, which are determined from the constitutive equations by means of a numerical integration method, R_i^e are the simulation values of stress, p the number of data points and n is the number of stress-strain curves to be considered.

Using this stress – stress curves the different parameters of the constitutive equations are obtained. Then the tensile tests are simulated with this material parameters implemented in Abaqus, using the displacement versus time curves of the experimental tests.

The simulated force-displacement output is compared with the one measured in the experiments. The deviation between both is used to improve the stress-strain behaviour. From the simulation results, displacement function \hat{S} and $\dot{\varepsilon}^{vp}$ is achieved. Then, they are used to get the updated effective stress $\hat{\sigma}$ and strain rate $\dot{\varepsilon}^{vp}$ using the force – time curves of the experiments. So, the constitutive equations parameters are updated to the current curves. This procedure is repeated until sufficient correspondence between the experiment and the simulation is reached.

4.3.2 Initial parameter determination

In this section, the achievement of the parameters for grain size and cavitation behaviour will be explained and other parameters first iteration determination is described.

The grain size average and cavity area fraction evolution equations were fitted at first and these values were maintained during all the interaction process. This was assumed to be accurate enough because the strain and strain rate values were obtained using the measurements carried out in the specimens of the interrupted tests (see Chapter 3), assuming that section strain minus volumetric strain due to cavitation ($\epsilon_{vol}^{VP} = f_v$) is the deviatoric effective viscoplastic strain ϵ_{dev}^{VP} . The deviatoric effective viscoplastic strain rate $\dot{\epsilon}_{dev}^{VP}$ was calculated making an approximation, taking into account the calculated ϵ_{dev}^{VP} and the interrupted test time. This is necessary to carry out since it was established that the controlled strain rate is not constant.

The other parameter initial determination was made in the conventional way assuming constant strain rate and purely uniaxial behaviour. Therefore, some error were obtained between the curve achieved in the conventional way, and the curves simulated using this same parameters entered in Abaqus.

Grain size average and cavity area fraction equation parameter determination

The fitted parameter values can be seen in Table 4.2 for the equation 4.9. The experimental results and the fitted curves are shown in Figure 4.5. Note that there is no static average grain growth behaviour fitting.

Table 4.2. Initial parameters for average grain size growth equation.

α_1	β_1	μ	d_0 (μm)
7.823×10^{-2}	4.605×10^2	1.251	16.72×10^{-3}

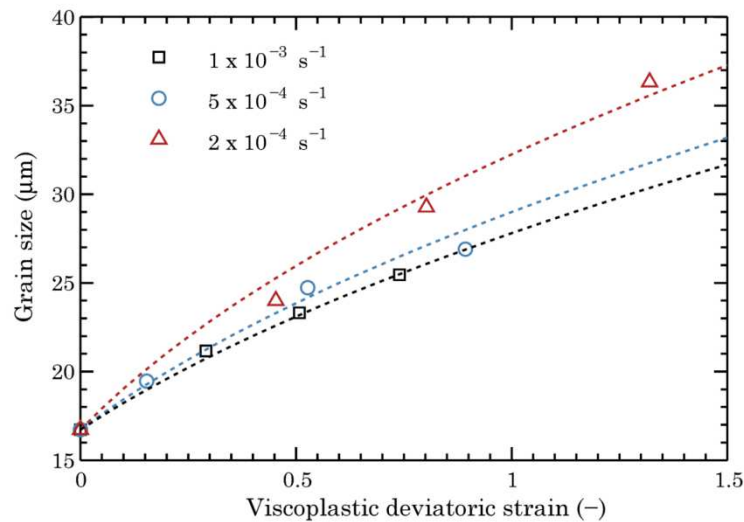


Figure 4.5.: Average grain size evolution for different interrupted tensile tests and fitted model curves.

Likewise, the cavitation area fraction was fitted using equations 4.17 and 4.18. In this case, the triaxiality factor σ_m/σ_e was determined to be 1/3. Similarly, the m parameter used for the equation 4.18 was decided to be constant for all strain and strain rates only for the cavitation area fraction evolution determination. Therefore, the parameter m was fitted as can be seen in Figure 4.6. The results can be seen in Table 4.3:

Table 4.3. Initial parameters for cavitation area fraction evolution equations.

m	f_{a0} (%)
0.452	0.1

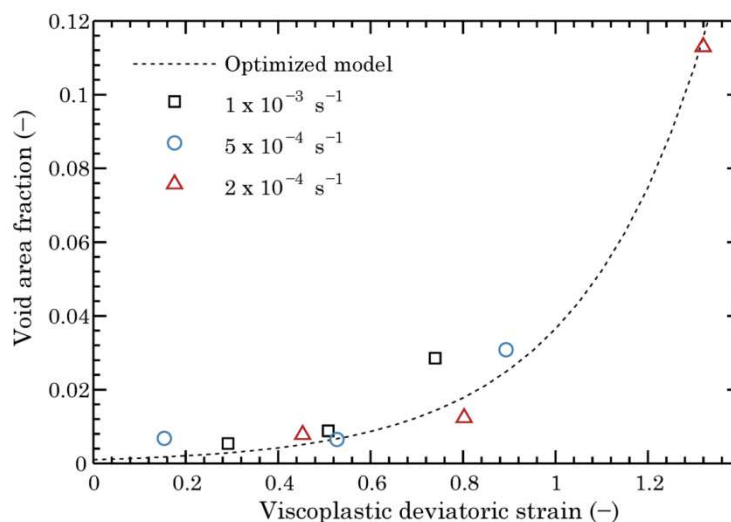


Figure 4.6.: Void area fraction evolution for different interrupted tensile tests and fitted model.

First parameter determination

For the initial parameter determination the traditional method of obtaining stress and strain curves was used. The common large deformation true stress – true strain equations are calculated using the next equations:

$$\varepsilon = \ln(l/l_0) \quad (4.26)$$

$$\sigma = (F/A_0)(l/l_0) \quad (4.27)$$

The achieved curves can be seen in Figure 4.7. Correspondingly, fitted model curves can be seen, with the achieved optimized parameters (Table 4.4). This model fitting show a good agreement with the points transformed into stress – strain curves from the experimental data.

Table 4.4. Fitted parameters for the initial model equation for viscoplastic voided material with fixed density

α	β	γ	C_1	γ_1	σ_y (MPa)
1.017×10^{-7}	0.324	1.123	5.87	4.98	0.1

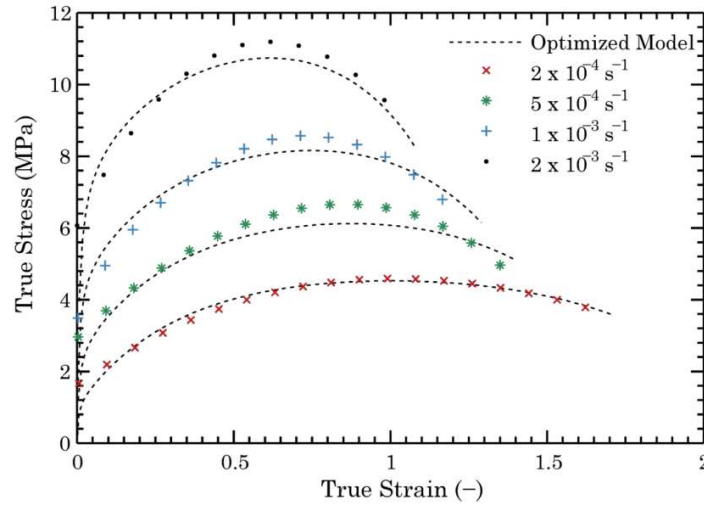


Figure 4.7.: “True” stress – “true” strain obtained in the traditional way and the fitted model curves for the initial parameter determination.

Conversely, these curves do show a conflict when the experimental data is compared to the theoretical values. The first comparison is the gauge section of the theoretical model and the one measured in the interrupted tests (Figure 4.8). All the measurements start at same value of 6 mm². Nevertheless, the evolution is quite different from the model to the experimental. Note that there is same behaviour for all the tests, being only one dash curve.

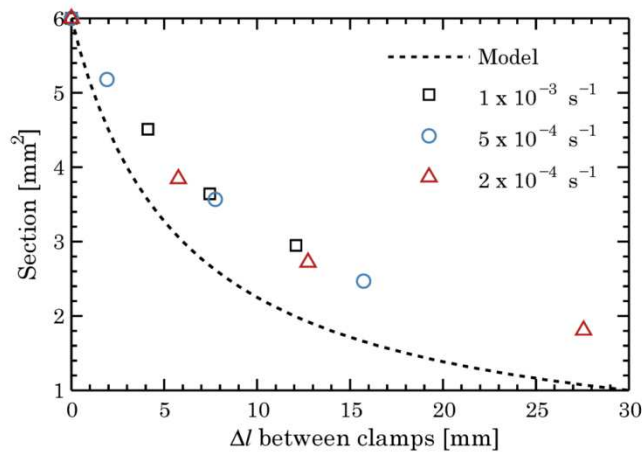


Figure 4.8.: Gauge section versus distance change between clamps for experimental data and initial model.

Furthermore, when the parameters of Table 4.4 are simulated variance is obtained for the supposed fitted true stress, true strain curves and the viscoplastic strain rates (see Figure 4.9). In the case of the true stress – true strain curves, it can be seen that there is similar behaviour at the beginning but the discrepancy increases with the strain. This can be because at low strains and with no damage, the true stress – true strain behaviour can be assumed to behave as purely uniaxial tests. However, when the strain rises, the incongruity becomes too prominent.

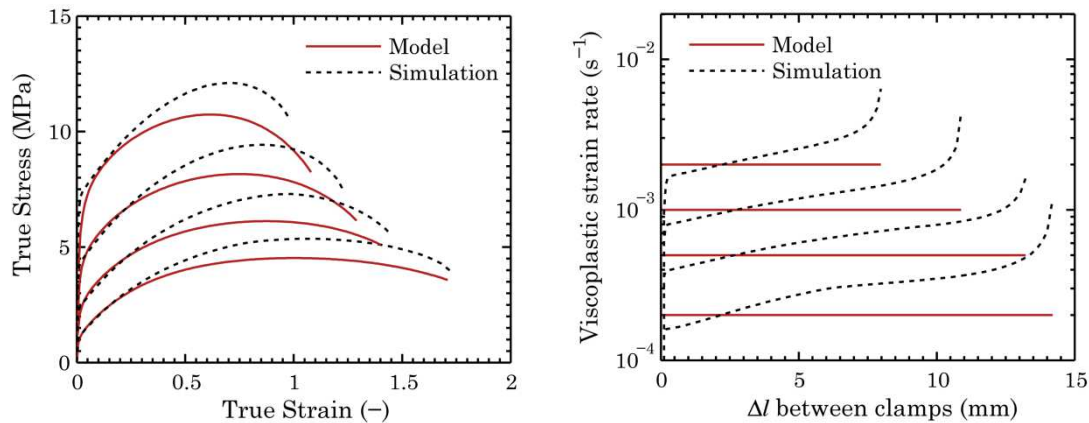


Figure 4.9.: Comparison between the curves obtained from the model using ideal situation and the simulated with the same equation parameters.

This is mainly obtained because when the tensile tests are simulated using parameters of the model, the section and strain behaviours are different from the supposed ideal ones, as can be seen in the simulated geometries of Figure 4.10. These geometries are very similar to the geometries obtained in the reality.

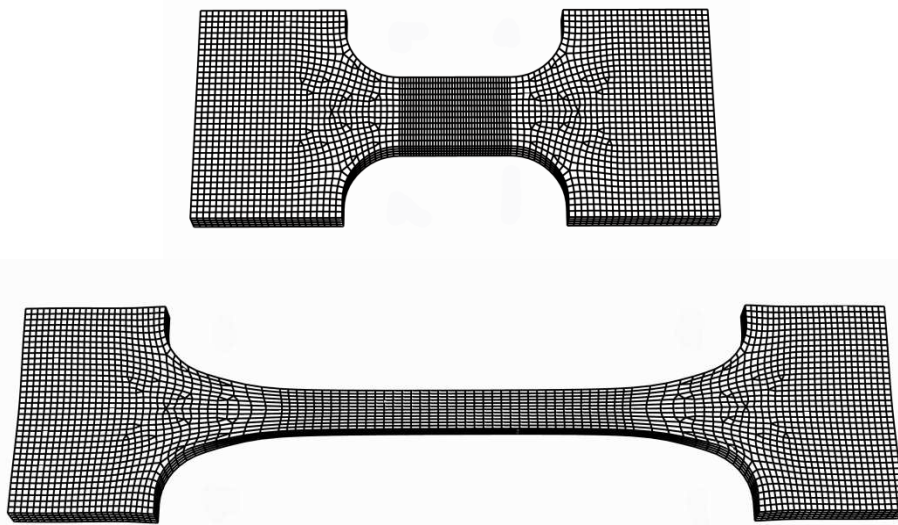


Figure 4.10.: Initial and formed simulated tensile test specimen geometries.

Furthermore, when the experimental force – displacement curves are compared to the obtained by the numerical modelling, the disagreement continues. As can be seen in Figure 4.11, the discrepancies increase when the distance between clamps increase too.

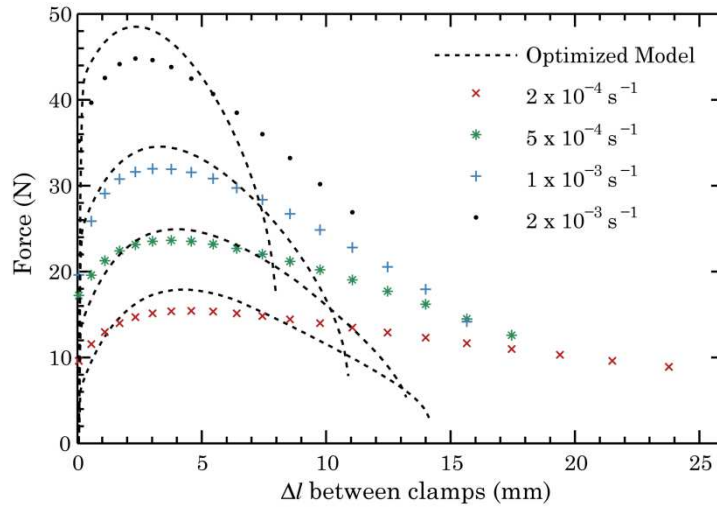


Figure 4.11.: Force – displacement experimental data versus simulated results for initial model parameters.

4.3.3 Viscoplastic model for voided material with density variation parameter determination

In this section the viscoplastic material model fitting results for voided material with density variation are shown. The parameters were achieved performing several iterations between Matlab and Abaqus. The fitted parameters can be seen in Table 4.5:

Table 4.5. Fitted parameters for viscoplastic model for voided material with density variation equations

α	β	γ	C_1	γ_1	α_2	β_2	σ_y (MPa)
9.567×10^{-5}	0.31889	0.304	5.96	2.03	-0.1893	-0.0869	0.1
α_1	β_1	d_0 (μm)	α_3	β_3	χ_{GBS}	f_{a0} (%)	
7.86×10^{-2}	4.61×10^2	16.72	1.98	2.03	0.5	0.1	

The true stress – true strain curves and the viscoplastic strain rate curves obtained by simulating the different tensile tests are the ones visible in Figure 4.12. In true stress – true strain curves it is shown that as in the equations there is no effect of the strain rate on the cavitation evolution of the material. Therefore, the softening behaviour of the curves is the same for the four tests, and the damage occurs at the same strain value. The differences on the elongation of the specimens are assumed to be due to different necking behaviour, which

makes the cavitation occur at different specimen elongation in each tensile test since the strain is different too.

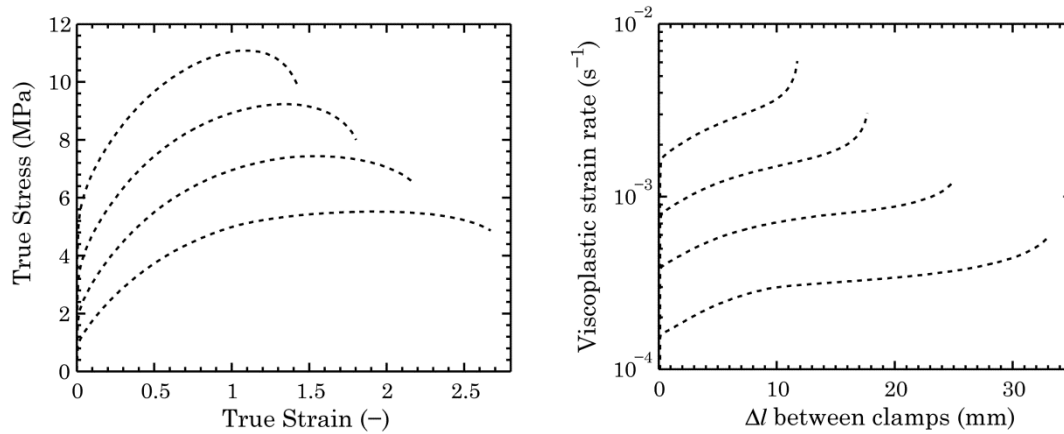


Figure 4.12.: True stress vs. true strain and viscoplastic strain rate values for simulated tensile tests for viscoplastic model for voided material with density variation equations.

In addition, the strain rate behaviour shows a non-constant pattern, as it was expected. The discrepancies between the idealized and the actual strain rates using the approach presented in the standard ASTM E2448 were previously shown by Khaleel *et al.* [Kha96]. Actually, these authors established that the strain rate is geometry dependent. It was shown that it is possible to use FEM models to adjust the velocity profiles [Kha98]. In this case, a new cross-head speed was computed such that the calculated strain rate was equal to the target strain rate. Nevertheless, it should be taken into account that the strain rate is not homogeneous throughout the gauge section of the specimen, a problem that becomes severe at high strain values (Figure 4.13).

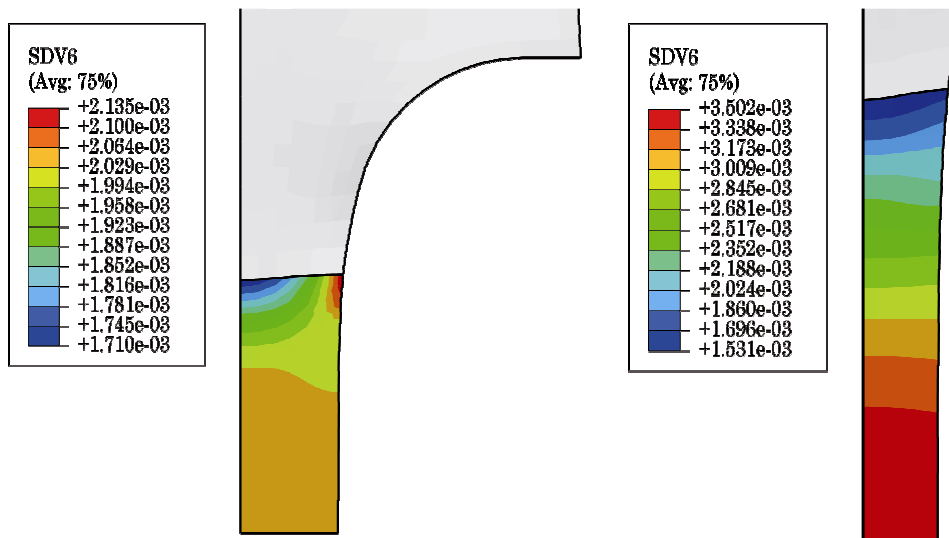


Figure 4.13.: Simulated strain rate pattern for the gauge section of a quarter specimen at strain value of 0.3 and 0.9 .

If constant strain rate deformation is required to perform at high strain values where damage is important, the mechanical phenomenology of the cavitation behaviour should be more properly understood.

As it was proceed in the previous section, to see if the model is in good agreement with the experimental data, two different comparisons can be done. The first is the comparison with the force – displacement data (obtained from the controlled strain rate tests). The second is the section area – displacement points (obtained from interrupted tests). The comparative graph of force – displacement data can be seen in Figure 4.14. The model curve and experimental data show good agreement for the different controlled strain rate tests.

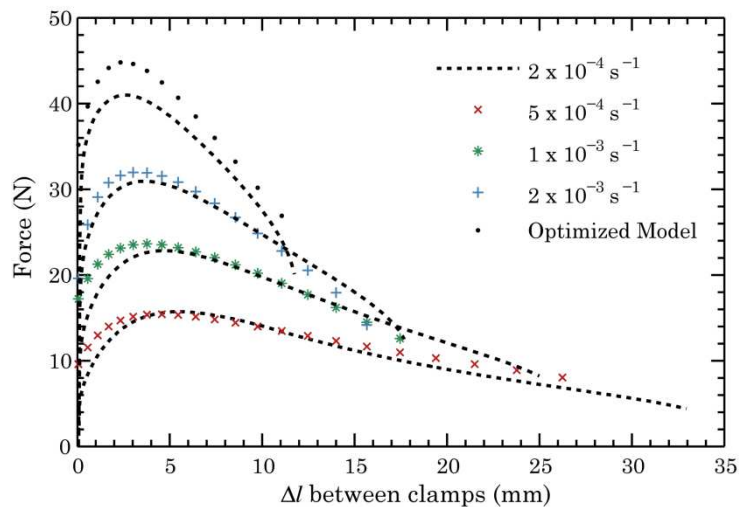


Figure 4.14.: Force – displacement experimental data versus simulated results for iterated model parameters.

The comparison of the gauge section of the simulated models and the ones measured in the interrupted tests is depicted in Figure 4.15. In this case, the model and the experimental data show better agreement than the idealized strain rate model results (Figure 4.8). It must be said that the concordance is very close at the beginning of the tests with low elongation values. However, it can be seen that the longer the elongation the closer the degree of agreement. Note that there is variation in the model case from one tensile test to other, being patent that necking occurs at some clamp distance points. This necking happens at lower elongation values at higher strain rate tests.

Furthermore, the average grain size and cavitation evolution data show a good agreement with the experimental data too (Figure 4.16). It must be empathized that the validity of the cavitation equation parameters is reduced to less than 5 % cavitation area fraction, and not extendable to near fracture behaviour.

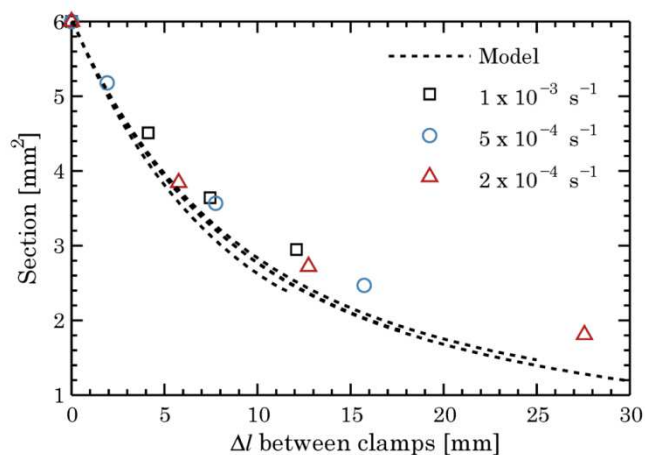


Figure 4.15.: Section area versus distance between clamps for model and experimental results.

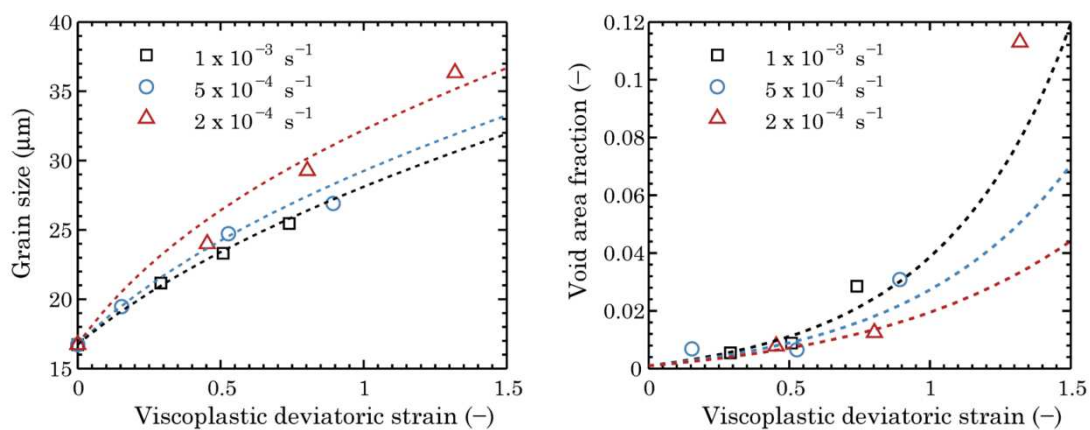


Figure 4.16.: Constitutive model versus experimental data for average grain size and cavitation area fraction evolution.

4.4 Closure

In this chapter, a modification of Dunne's mechanism-based constitutive equation set is proposed. The modifications are mainly focused in implementing the damage behaviour materials suffer from cavitation evolution. Due to this, the modifications can be divided into:

- A damage behaviour due to void area fraction growth, implemented by continuum damage mechanism CDM method, and with a damage variable ω
- A volume change in the material due to CDM assumption, assuming that the volume change rate is equal to total cavity volume growth
- A cavity evolution description that takes into account the material state (triaxiality ratio) to determine the void area growth rate, and uses microscopic and macroscopic stresses relationship concept.

On the other hand, an inverse technique has been developed to fit the modified constitutive equations, in order to obtain precise equation parameters. The comparison of the different curves show a remarkable improvement in the accuracy of simulated tensile tests comparing to the experimental data.

Moreover, severe differences were achieved when stress, strain and strain rate were calculated theoretically or by inverse modelling. The most relevant discrepancy is the difference of strain rate values, having errors of more than 50 % for the same tensile test (see Figure 4.17). These dissimilarities show the importance of the tensile test specimen geometry and the significance of the inverse modelling as a tool for SPF.

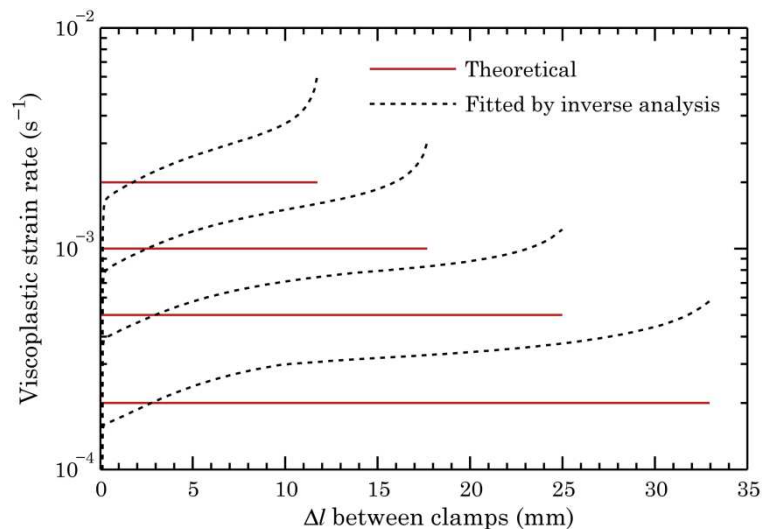


Figure 4.17.: Strain rate values calculated theoretically and by inverse modelling.

SPF NUMERICAL MODEL IMPLEMENTATION

Synopsis

In the case of the superplastic forming, even more than in the case of other sheet metal forming processes, numerical modelling is a key to optimize the process time and the overall costs of the manufacturing. In this chapter, the development of the implementation of SPF process into Abaqus is explained, describing for that the analysis type, body discretization, contact description, material model implementation and loading strategies.

Therefore, the numerical model implementation was used for the development of two aspects related to pressure-time curves:

The first is the improvement of accuracy of the control in Abaqus, having strategies that have no convergence problem but smooth control schemes. For this aim, a technique was developed, using a gas cavity volume control instead of gas pressure control.

The second is the optimization of the SPF process itself, using the mechanism-based material model as basis for exploiting maximum superplastic capabilities of the material during the process.

5.1 Introduction

In the case of the superplastic forming, even more than in the case of other sheet metal forming processes, numerical modelling is a key to optimize the process time and the overall costs of the manufacturing.

In the first section of this chapter, the used mechanical approach and the finite element analysis software are brought. Then, the geometrical discretization of the tensile tests, and two gas forming SPF geometries are described, likewise cavity flow discretization. Similarly, the contact and friction behaviour is described and the implementation of the material model presented in the Chapter 4 is explained.

On the other hand, in the second part of this chapter, the loading and the pressure control strategies are explained and the implementation of the backpressure and its effect is shown.

Finally, general results of the simulations are presented, showing the benefits and the drawbacks of the different approaches that were carried out during this work.

5.2 Mechanical analysis

Implicit and Explicit solvers are the two common numerical techniques currently used in FE simulation industry. From the physical point of view, the kinetic energy plays an important role in selecting the type of FE technique to be used for the analysis. We can broadly classify the metal forming processes into two types.

1. In quasi-static problems, the kinematic energy is insignificant comparing to the total energy. Superplastic forming falls into this category.
2. In high strain rate phenomena, or purely dynamic processes, the kinetic energy is overwhelmingly dominant. This is the case of processes with a high energetic impact.

The dynamic explicit method is advantageous for analysis of sheet metal forming where the real time is just a few seconds. It has the characteristic of less memory requirement and greater computer efficiency since the need for consistent stiffness matrix is obviated. However, for a process such as superplastic forming, this method reveals its inability to reduce the calculations time because of stability requirements on the size of the time step, thus requiring larger number of incremental steps. In addition, when rate sensitive materials are involved, accurate results are extremely difficult to obtain unless a large number of steps are used. Therefore, a quasi-static mechanical analysis was selected in order to simulate the SPF process, using commercially available finite element software Abaqus Standard.

5.3 Body discretization

The simulated geometrical shapes are divided into two different processes. On one hand the aforementioned tensile tests were modelled at different controlled strain rate. Issues related to this geometry have been extensively discussed in the Chapter 4, as the main reason for the simulation of this shape was to obtain the viscoplastic material model parameters using inverse engineering. On the other hand, two SPF geometries were simulated.

The tensile tests were modelized into two different bodies. One is a quarter of the specimen and the other a rigid element that represents the clamp radius (see Figure 5.1).

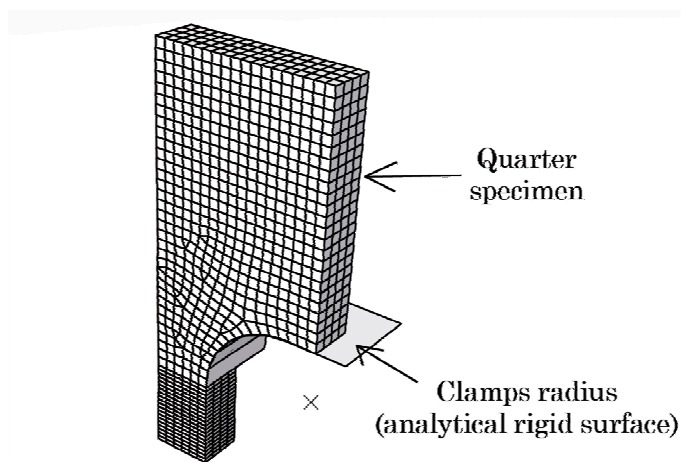


Figure 5.1.: Mesh for tensile specimen representation with a clamp.

For simulating the SPF process, two different geometries were studied during this work: the first one is a bulge-test shape and the second a half toroid shape. Both geometries were superplastically formed as it is going to be explained in the Chapter 6 using the SPF prototype designed for the realization of this research work. As both geometries are axisimetric, and taking into account that superplastic forming simulation can be quiet time consuming, it was decided to implement an axisimetric model for this work in the two cases.

The bulge-test geometry was selected for the material constitutive model validation. Using this geometry, the material behaviour can be analyzed in a biaxial form with a quite simple approach. Furthermore, the effect of the backpressure can be studied using this kind of die, being the effect of the friction between the die and the sheet almost irrelevant. Other advantage of using this shape is the possibility of forming the material until fracture, which can be impossible with close dies at certain superplastic conditions. A schematic representation of the bulge-test model can be seen in the Figure 5.2.

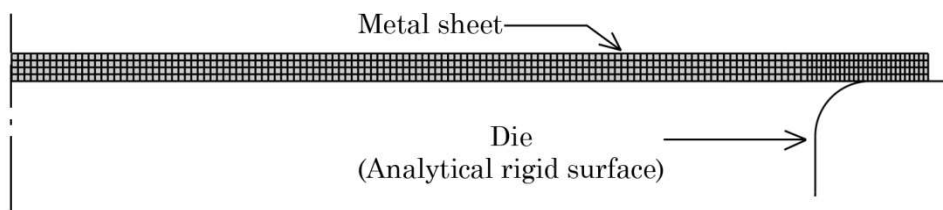


Figure 5.2.: Bulge-test model discretization with axisymmetric element.

To take into account a more realistic situation of the SPF process, a second geometry was selected, the above-mentioned toroid shape. This geometry is more complex to form and there is more contact between the die and the sheet comparing to the bulge-test geometry so the forming pressure-time curves are more sensitive to the roughness of the die. The schematic representation of the bulge-test model can be seen in the Figure 5.3.

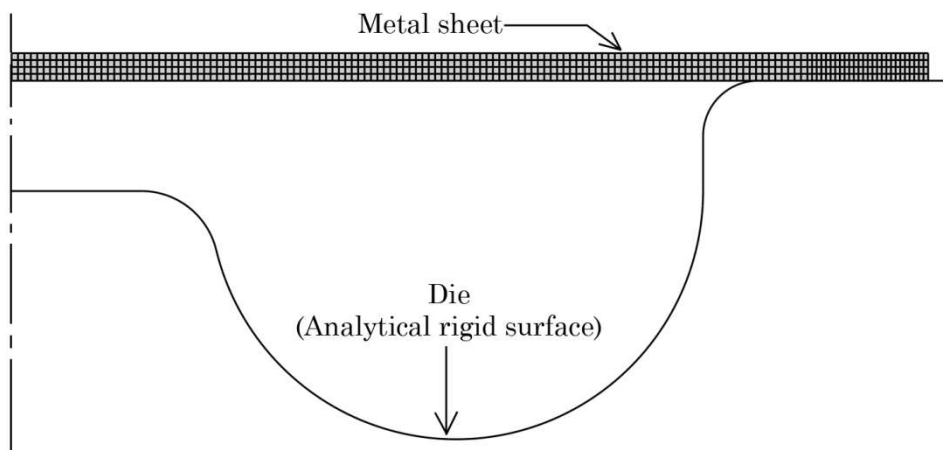


Figure 5.3.: Toroid-shape model discretization with axisymmetric element.

5.3.1 Sheet mesh

Although usually the metal sheet of forming processes are modelled using shell elements because they represent properly the bending behaviour during the forming and are not too time consuming, in this case all the sheet elements were selected to be solid ones. The reason of picking the continuum solid elements is that the shell elements are not capable of representing volume changes due to the cavitation behaviour.

The chosen elements were fully integrated first order elements with incompatible mode. This kind of element was selected to avoid the hourglassing without miscalculating the bending effects of the material by shear locking.

In the case of the tensile tests, the specimen were meshed using C3D4I. These elements continuum three-dimensional elements. with eight node and four integration points. The specimen was discretized into 2288 elements. Note that there is a region with finer mesh in the gauge section (see Figure 5.1), being the longitudinal distance of the elements 2/3 of the width and thickness direction. This longitudinal fine mesh was obtained to avoid problems due to the large deformation the elements undergo.

For the SPF gas forming, CAX4I elements where used to represent the sheet. These elements are axisimetric four node fully integrated elements with incompatible mode, so they use four integration points within the element. The sheet was discretized in 600 elements with four elements in the thickness direction.

5.3.2 Die mesh

Abaqus permits to use analytic rigid parts, but only when they are simple. Therefore, only extruded and revolved parts can be discretized as analytic rigid parts, having an enormous improvement in contact problems. These analytic rigid parts made a difference in terms of calculus time since the integration time was permitted to be larger than in the simulations using common rigid elements.

Consequently, the radius of the clamp in the case of the tensile tests and the axisimetric dies in the case of the SPF gas forming processes were discretized as analytic rigid parts (see Figure 5.1, Figure 5.2 and Figure 5.3)

5.3.3 Fluid mesh

As is going to be explained in a subsequent section, fluid elements where used in some simulation to describe the pressure done by the argon in the SPF process. The capability of fluid-filled cavities is available in ABAQUS/Standard and Explicit. It provides the coupling between structure and the enclosed fluid. It is also assumed that the cavity is completely filled with pneumatic (compressible) or hydraulic (incompressible) fluid.

Hydrostatic fluid elements have to cover only a boundary of the fluid-filled cavity. All fluid elements are first-order, which means that the interpolation of the element displacement is linearly dependent on node displacement. All hydrostatic fluid elements associated with the cavity share common reference node that has a single degree of freedom representing pressure in the cavity. Actual pressure in the cavity (PCAV) and actual cavity volume (CVOL) can be obtained as output in the cavity reference node.

The easiest possibility of modelling flow of the fluid is just removing and adding the fluid into the cavity using *FLUID FLUX. Using this command we define mass flow rate q into the cavity. Defined flux can vary during the step when *AMPLITUDE command is used.

During this work, fluid-filled cavity capabilities were used for controlling the cavity volume between the SPF sheet and the cover of the die. The cavity volume was controlled by the user-subroutine UAMP, as is described in Figure 5.4. For it, F2D2 hydrostatic fluid elements that share nodes with the sheet and die cover elements were used through all the surface of the cavity.

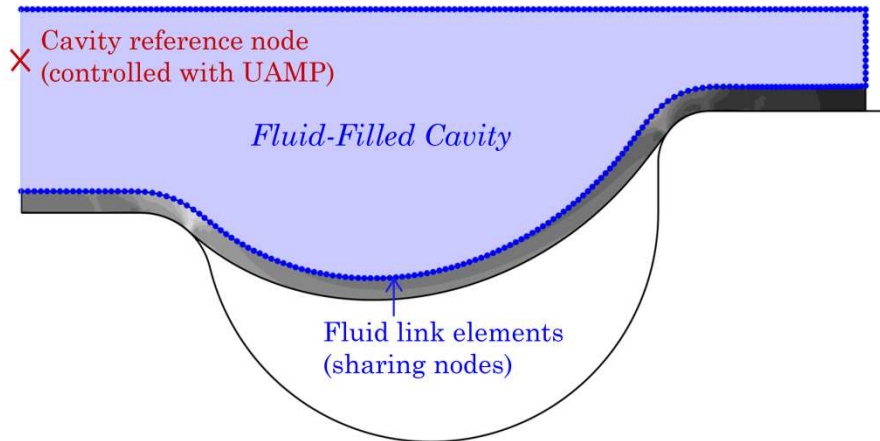


Figure 5.4.: Fluid-filled cavity in a toroid shape geometry with the hydrostatic fluid elements nodes in blue and the cavity reference node in red.

It must be taken into account that as the intention in this work was to control the volume of the cavity, the modeled fluid was characterized as an incompressible fluid with unity density. Using this technique the pressure for the process can be obtained changing the volume flux into the cavity. In contrast, it could be interesting using a flow rate control strategy instead of the pressure control in SPF processes, as first kind of control have some advantages over the second one. Hydrostatic fluid elements give the possibility to get flow rate-time curves using pneumatic compressible and temperature dependant fluid parameters.

5.4 Contact and friction

The contact problem during the SPF process is complex. Contact between the sheet and the die is highly nonlinear because of its asymmetry, where at a position in space a node is either free or rigidly constrained depending on an infinitesimal change of position normal to the die surface. The boundary conditions dramatically vary as a result of change in the contact region.

The mechanical contact between the sheet and the tools employed in the numerical models is based on the so-called penalty method; in addition, a finite sliding is used for the formulation of the mechanical constraint. Firstly, slave and master surfaces are defined, with nodes lying in those surfaces referred as slaves and master nodes, respectively [Abq08]. At

each instant of time, the penetration of any slave node through the master surface is checked and a contact force is applied in those penetrating nodes. The magnitude of the contact force is proportional to the penetrated distance.

An extended version of classical isotropic Coulomb friction model provided in Abaqus is used during the present SPF analysis. Friction modelization is based on the Coulomb formulation, where the stick regime (no relative displacement between the bodies) and the slip conditions (relative displacement between the bodies) are proportional to the normal force. In stick conditions, the frictional force is defined as:

$$F_t < \mu \cdot F_n \quad (5.1)$$

where F_t is the friction force, F_n is the normal force and μ is the friction coefficient. On the other hand, in sliding conditions the frictional force is defined as:

$$F_t = \mu \cdot F_n \quad (5.2)$$

In general, despite the significance that friction behaviour can have in simulation of SPF, there are few experimental measurements of the friction parameter μ [Che96, Kel04, Sni11].

For this work two different values of μ were used, since as it is going to be explained later, two different dies of two different base materials with different roughness were used. For the refractory stainless steel bulge-test die $\mu = 0.16$ value was used, based in the work of [Che96]. For the refractory concrete toroid shape die $\mu = 0.5$ was used.

5.5 Material model implementation

The material model used for this work was extensively described in the Chapter 4. Abaqus provides different user subroutines that allows users to adapt Abaqus with particular analysis requirements. The aforementioned constitutive equations were implemented into the FE solver through user defined subroutine CREEP.

CREEP subroutine was used to define time dependent viscoplastic material behaviour. The user subroutine must define the increment of inelastic strain, as a function of stress and the time increment. Other variables such as grain growth and cavitation were defined as solution dependent state variables (SDV). SDV's are values that can be defined to evolve with the solution of the analysis.

Furthermore, CREEP user subroutine allows to model deviatoric and hydrostatic stress dependent materials, is able to describe non-associated flow models, and takes into account

volumetric strain behaviours. This is achieved filling in creep strain increment $\Delta\bar{\epsilon}^{cr}$ and swelling strain increment $\Delta\bar{\epsilon}^{sw}$ in the next equation [Abq08]:

$$\Delta\boldsymbol{\epsilon}^{cr} = \Delta\bar{\epsilon}^{cr} \frac{\partial \sigma_e}{\partial \boldsymbol{\sigma}} + \frac{1}{3} \Delta\bar{\epsilon}^{sw} \mathbf{I} \quad (5.3)$$

Likewise, USDFLD user subroutine is used to obtain maximum principal stress that is necessary to solve the equation (4.22).

For loading control strategies, an iterative procedure of CREEP and UAMP subroutines was used, which will be more extensively explains in the section 5.6.4.

5.5.1 Cavitation volume growth and triaxiality dependence

As mentioned before, the equations used in this work for describing the cavitation fraction evolution, are susceptible to change depending on the load state. As the data for the fitting of the material equations is obtained from uniaxial tests, the triaxiality ratio has been set to the theoretical value of $\sigma_h/\bar{\sigma} = -1/3$.

The effect that the triaxial ratio has in the material behaviour according to the viscoplastic model for voided materials with density variation equation set is shown in Figure 5.5.:

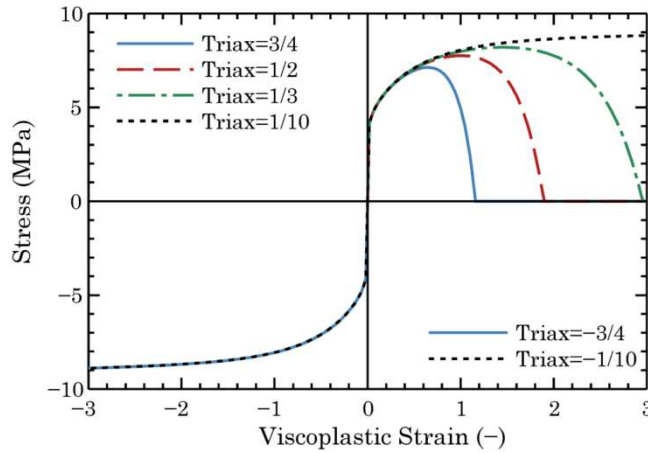


Figure 5.5.: Curves at different triaxial states according to viscoplastic model for voided materials with density variation.

The equations point out that the softening tendency can grow dramatically depending on the triaxial state of the material. In the case of $\sigma_h/\bar{\sigma} = 3/4$, which can be considered as the theoretical value of the triaxiality in the pole of a dome in a bulge-test of SPF using equation (4.22), the maximum strain that can be reached for the same strain rate is less than a half. Furthermore, the softening behaviour is significantly superior at higher strain rates.

5.6 Loading and pressure curves

If a superplastic aluminium sheet is deformed at its optimal superplastic temperature, control over the maximum strain rate is necessary. Exposing the material for a long time to a high temperature will result, however, in losing superplastic properties, so the deforming time should be as small as possible. Hence, the optimal way to deform a sheet is by taking care that at each time point, this maximum strain rate will be reached. This can be achieved by prescribing the forming pressure as a function of time [Luc04, Li04, Hoj08].

Superplasticity is exhibited by materials only in a narrow strain rate range with an optimum value unique to each material. This factor makes it essential to determine the pressure loading history in order to maintain the maximum strain rate near the optimum value throughout the whole forming process. Furthermore, as the target strain rates are usually small, adjusted pressure-time curves are preferable in order to explore the maximum superplastic capabilities of the material and consequently reduce the forming times.

Different ways to obtain the pressure history are presented in this work. The different approaches developed used Abaqus Standard as basis with the model previously presented. The approaches used for a proper obtaining of the curves are:

- Control strategy
- Target integration point number selection
- Target strain rate selection by material constitutive equation

5.6.1 Control strategy

Abaqus provides an own control strategy formulation, but generally talking is rough but effective in almost any case. Apart from this approach, two other control strategies are presented, an smoothed pressure control strategy and a smoothed volume control strategy.

Abaqus' pressure control strategy

This control formulation is implemented in Abaqus by means of solution-dependent amplitude [Abq08]. The applied pressure P is to be varied throughout the simulation to maintain the strain rate $\dot{\epsilon}$ at a predetermined value $\dot{\epsilon}_{opt}$. During an increment, Abaqus calculates r_{max} , the ratio of the equivalent strain rate to the target optimal strain rate for any integration point in a specified element set. This element set is selected based on the control scheme used i.e. constant strain rate control in the free forming region, constant strain rate control in the die entry region, maximum variable strain rate control or strain rate gradient control.

$$r_{max} = \frac{\dot{\epsilon}_{max}}{\dot{\epsilon}_{opt}} \quad (5.4)$$

Assuming all quantities are known at increment n , the pressure algorithm is developed as follows:

if	$r_{\max} < 0.2$	then	$P_{i+1} = 2.0P_i$
if	$r_{\max} > 3.0$	then	$P_{i+1} = 0.5P_i$
if	$0.2 \leq r_{\max} < 0.5$	then	$P_{i+1} = 1.5P_i$
if	$0.5 \leq r_{\max} < 0.8$	then	$P_{i+1} = 1.2P_i$
if	$0.8 \leq r_{\max} < 1.5$	then	$P_{i+1} = P_i$
if	$1.5 \leq r_{\max} < 3.0$	then	$P_{i+1} = 0.5P_i$

where P_{i+1} is the new pressure value corresponding to the iteration $i + 1$ and P is the old pressure value corresponding to the iteration i . Although the controlling algorithm is simple and relatively rough, it helps to obtain the desired pressure time profile at a low computational cost.

Smoothed pressure control strategy

This pressure time accomplishing scheme needs to be programmed using user subroutines. In this case, two user subroutines are used: the CREEP subroutine for the acquisition of the material properties (and implementation of the material constitutive equations as explained before) and the UAMP subroutine for the control of the pressure.

Assuming all quantities are known at increment i , the pressure algorithm is developed as follows [Hoj08]:

$$P_{i+1} = 1 - \ln(r_{\max}) \cdot P_i \quad (5.5)$$

This scheme is smoother and gets better ratio results, but is not very robust and presents problems when there are contact condition changes and the pressure change ratio varies abruptly. Furthermore, it presents problems in the final stages of the forming where the strain rate sensitivity ratio m and the thickness of the material are smaller and with small pressure time variations there are large changes in the strain rate.

Smoothed fluid control strategy

Due to the problems derived from the pressure control algorithm, which in general are robust but rough or smooth but weak, a new approach for pressure history solution obtaining was developed.

Instead of controlling the pressure loading in the surface of the sheet, this new approach controls the volume inside the cavity. The volume change in a superplastic cavity blow forming process is monotonic and its derivative is almost constant. Using Abaqus a volume change can be controlled and calculate the pressure that is needed inside this fluid cavity as explained before.

The followed equation for doing a smoothed fluid control was the next one:

$$\dot{V}_{i+1} = 1 - \ln(r_{\max}) \cdot \dot{V}_i \quad (5.6)$$

where \dot{V}_i is the previous increment volume flow and \dot{V}_{i+1} is the new volume flow.

5.6.2 Target integration point number selection

Other strategy here developed was the smoothing of the control by selecting more than one integration point's strain rate to quantify the maximum equivalent strain rate of whole the sheet, obtaining an average. Moreover, strain rate points with maximum strain rates can be deselected from the maximum equivalent strain rate, to avoid non-wanted effects of numerical instabilities. Lukey *et al.* presented this kind of approach [Luc 04].

In the case of a maintaining the maximum strain rate to the constant optimum strain rate target $\dot{\epsilon}_{\text{opt}}$, next equation is used:

$$r_{\max} = \left(\frac{1}{n_a - n_b} \sum_{i=(n_{\text{tot}}-n_a)}^{(n_{\text{tot}}-n_b)} \dot{\epsilon}_{\max} \right) / \dot{\epsilon}_{\text{opt}} \quad (5.7)$$

were n_{\max} is the total integration point, n_b number of integration points with $\dot{\epsilon}_{\max}$ which are deselected from the average and n_a is the number of integration points with $\dot{\epsilon}_{\max}$ that would be part of the average. Note that $n_{\text{tot}} < n_b < n_a$.

5.6.3 New approach: m max strategy by material constitutive equation

Usually, an optimum constant strain rate is chosen at the strain rate where the maximum elongation is achieved, trying to approach the m_{\max} of the material (Figure 5.6 b). One of the advantages of the mechanisms-based hyperbolic equations is that describes a sigmoidal curve. Therefore, the strain rate sensitivity value can be calculated for a wide range of strain rate and strain values, unlike other simpler material equations like the power law. For the material forming process, the maximum m value is wanted for having less softening behaviour in the material. Both the material instability and the fraction of cavitation increase when the strain rate sensitivity decreases.

The strategy presented in this work focuses on reaching maximum m value using the mechanisms-based hyperbolic equation set and the viscoplastic model for voided materials with density variation as a tool. Using this set of equations, it is possible to predict the optimal target strain rate at certain strain and stress states.

Typically, most superplastic materials show a sigmoidal variation of the flow stress with strain rate [Pil89], and they can be represented with the curve shown in Figure 5.6 a.

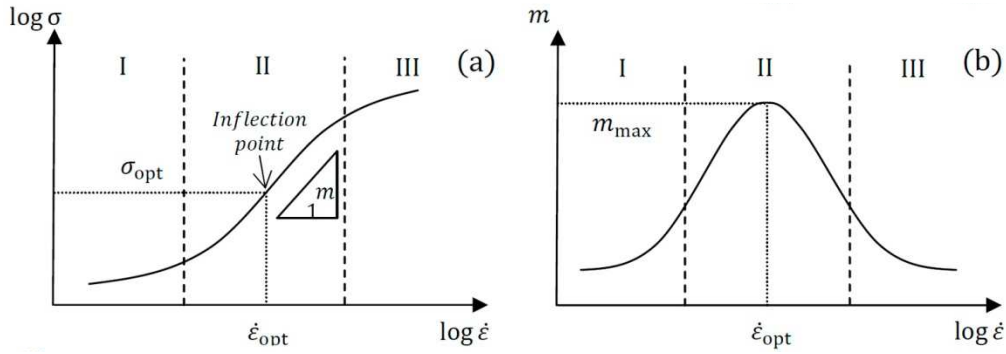


Figure 5.6.: Schematic (a) sigmoidal variation of the logarithmic flow stress vs. logarithmic strain rate and (b) strain rate sensitivity vs. logarithmic strain rate

This sigmoidal curve passes through a maximum, called inflection point. The slope of this curve is strain rate sensitivity m (Figure 5.6 b):

$$m = \frac{\partial \ln \sigma}{\partial \ln \dot{\epsilon}} \quad (5.8)$$

For SPF processes, the most suitable forming strategies are those that allow the obtaining of the target part at as low as possible forming time. The major inconvenience for using forming stress-strain curves that use the maximum strain rate sensitivity index of the material through the process is that the material constitutive equations are not usually able to reproduce this sigmoidal curve. This can be seen in Figure 5.7, where m value of a common double power law and a Dunne's constitutive equations are compared

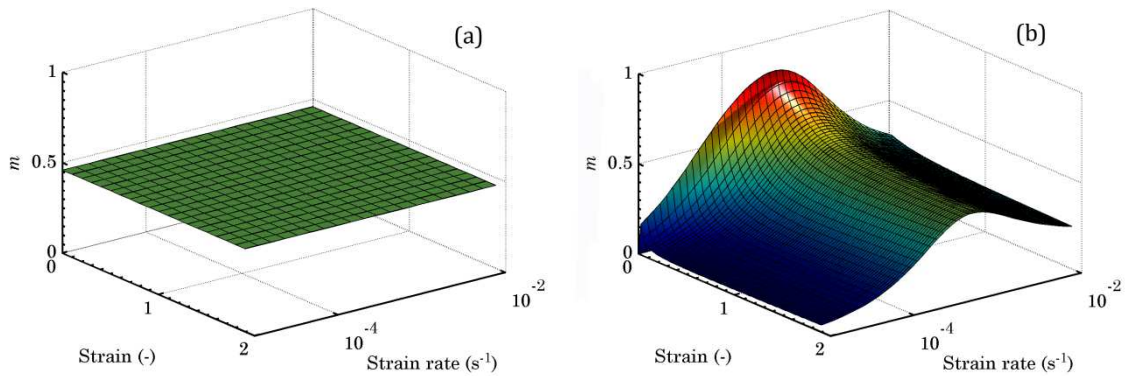


Figure 5.7.: Strain rate sensitivity versus strain rate at different strain values.

Therefore, with the help of the mechanism-based hyperbolic equation set, a new forming strategy that takes into account the formability and the cavitation behaviour of the material has been developed.

On the other hand, a number of researchers have examined the effect of stress state on cavitation [Pil86, Pil89, Sto83, Bae02a, Bae02a, Kul06]. The cavitation evolution is important

not only for an accurate description of the material behaviour and fracture, but also for the consideration that excess cavity concentration can degrade mechanical properties before fracture [Sto83]. Pilling and Ridley [Pil89] showed that the cavity growth rate under biaxial tension is different to that under uniaxial tension, which means that cavitation is stress-state dependent.

Furthermore, it has been shown by different authors that the strain rate sensitivity m value changes with the strain and strain rate [Bae02a, Pil91]. This effect can be seen in Figure 5.8.

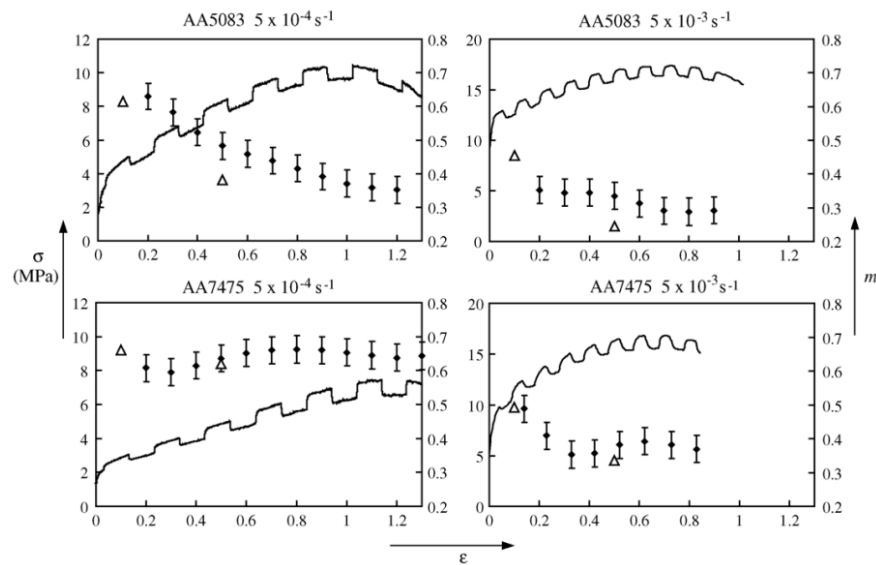


Figure 5.8.: Jump test carried out by Bae and Ghosh where the a variance of strain rate sensitivity values can be seen [Bae02a].

The Dunne’s constitutive equation has been modified to describe a cavitational behaviour. The uniaxial test is used as example, since the triaxiality ratio changes depending on the load state. The strain rate sensitivity vs. logarithmic strain rate can be plotted for different strains (Figure 5.9), and the maximum m value of each different strain curve has been obtained.

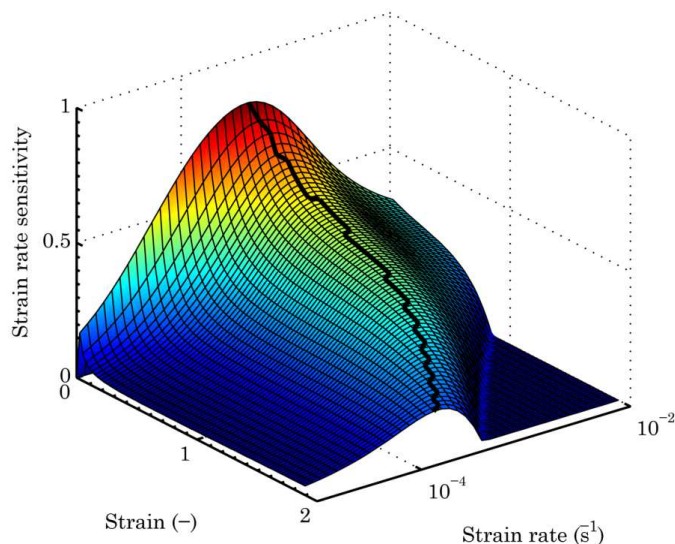


Figure 5.9.: Strain rate sensitivity versus strain rate at different strain values.

So the target strain rate depending on the strain can be seen in Figure 5.10 (a) and (b):

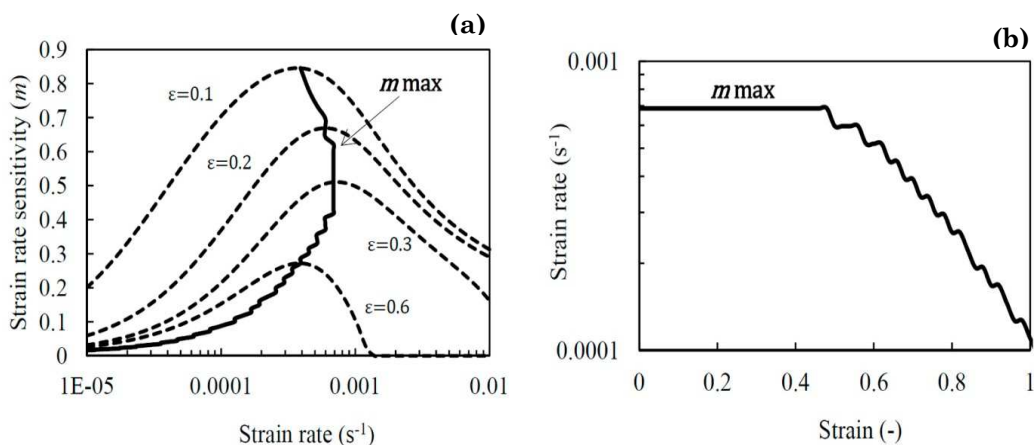


Figure 5.10.: Optimal strain rate path for a tensile test.

Note that the curve starts with higher strain rates values, around $7 \times 10^{-4} s^{-1}$, but it needs to slow down near a strain of 0.5, when the fraction of cavitation starts becoming important. Khraisheh et al. [Khr06] presented a similar shape curve, using a multiscale stability criterion as strategy for superplastic tensile test of a magnesium alloy AZ31.

5.6.4 Implementatin of control strategies into abaqus

The control strategies above mentioned were implemented into Abaqus using an iterative procedure between CREEP and UAMP subroutines. A flow chart of the strategy is shown in the Figure 5.11.

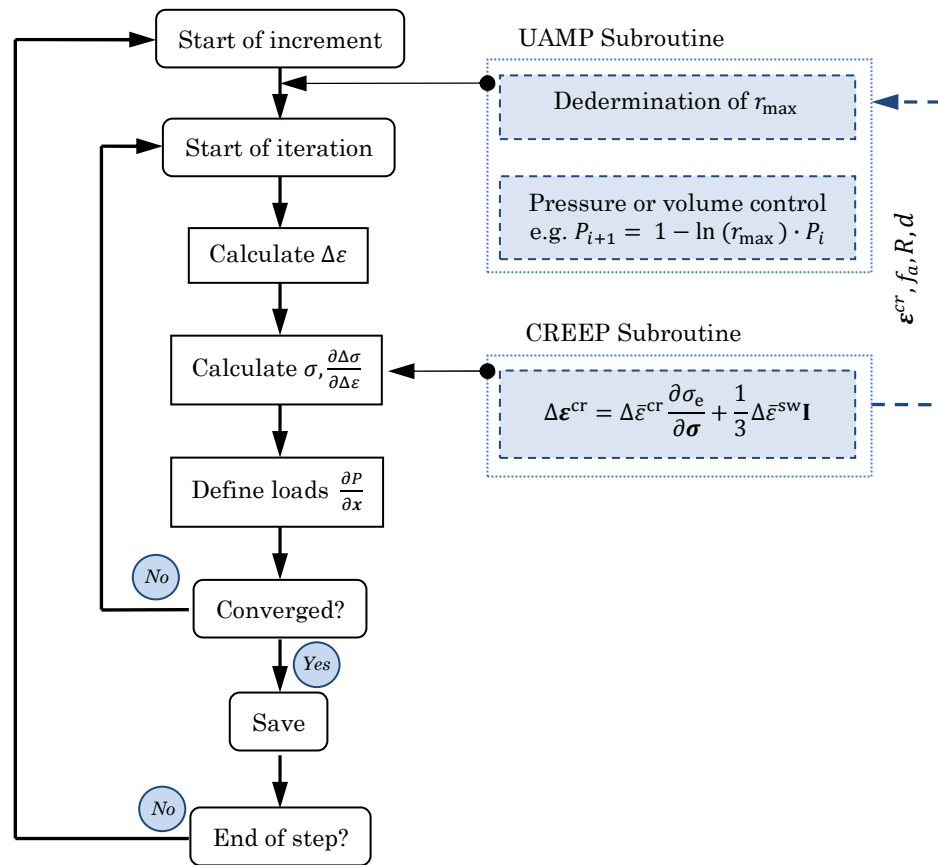


Figure 5.11.: shows the basic flow of data and actions from the start of an ABAQUS analysis to the end of a step.

The CREEP subroutine was developed to provide Abaqus with information needed to describe the material like deviatoric and volumetric strain, grain size, isotropic hardening and cavitation area fraction. At the same time, it was used to pass information to UAMP subroutine. Employing these values, UAMP determines the maximum ratio r_{\max} for one or more integration points, by picking between the optimum constant strain rate target approach or the maximum m approach. Finally, the UAMP subroutine decides the new amplitude (depending on the r_{\max} value) by means of pressure or volume control strategies.

5.6.5 Implementation of the backpressure into Abaqus

As the cavitation behaviour the SPF materials can be reduced by using backpressure, the constitutive equations of this work are triaxiality factor dependent. This backpressure can be easily implemented into Abaqus by using uniform pressure loads. Nevertheless, the main drawback of the implementation is that the backpressure value should have no effect when there is a contact between the sheet and the die. Therefore, the surface where there is backpressure should be the one is not in contact, which will be changing during the process (see Figure 5.12).

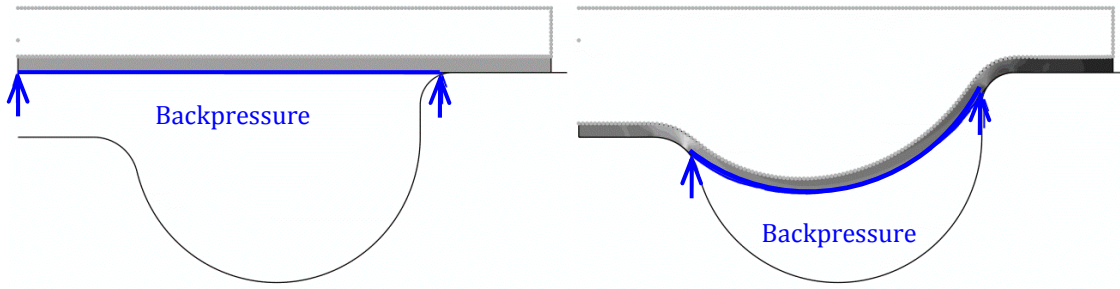


Figure 5.12.: Difference in the surface where the backpressure (in blue) should be applied in different increments of the process.

If the pressure is maintained in contact surfaces, it will have an effect in the contact normal and the friction between the sheet and the die, miscalculating them into a less severe state. Consequently, a subroutine set was developed to determine the surfaces that undergo backpressure in each increment of the simulation. First, UMEHSMOTION subroutine is used to determine which nodes are in contact with the die. Then the subroutine solves if all the nodes of the surface of an element are in contact. Then if it is concluded that the surface of an element is in contact, the DLOAD subroutine removes the backpressure from the integration points of this element surface. All this procedure is schematically represented in Figure 5.13.

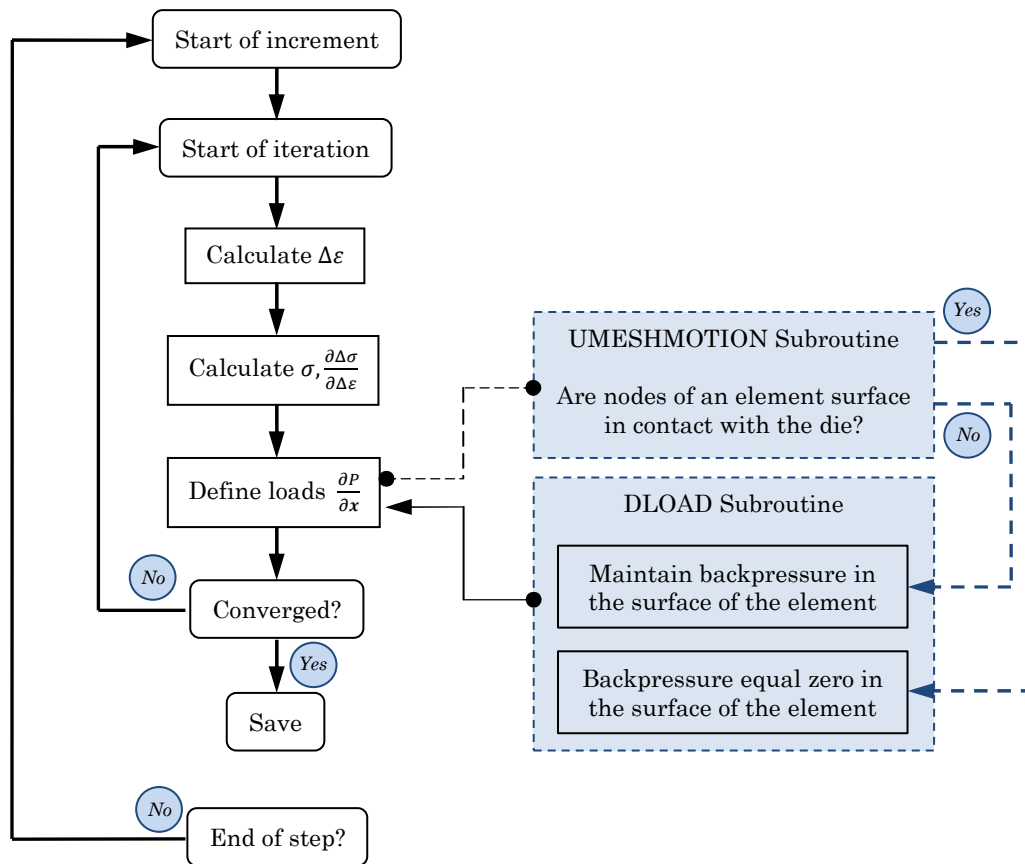


Figure 5.13.: shows the basic flow of data and actions from the start of an ABAQUS analysis to the end of a step.

5.7 General results

In this section, general results obtained from the simulations will be explained. They are mainly focused in the effect the backpressure and the control strategies have in the simulations. The uniaxial tensile test results are not presented in this section as the most important data have been shown in the Chapter 4. Similarly, the results of different biaxial tests that were numerically and experimentally carried out will be presented in Chapter 6 in the numerical model validation section.

Therefore, the results presented in here are shown to explain:

- The effect of the backpressure in the model
- The effect of the different control approaches in the pressure-time curves

5.7.1 Backpressure effect

Three different simulations have been run for modelling the bulge-test of a material that suffers from cavitation damage and see the effect the backpressure has on the material behaviour of the simulation. The three of them are based on a step of pressure rise and a constant gas pressure value. The difference between them is the backpressure value that is applied in the other side of the sheet. In the first simulation a pressure of 0.15 MPa and no back pressure has been used, in the second one a pressure of 0.45 MPa and 0.4 MPa of backpressure and in the third one 0.85 MPa of main pressure and 0.8 of backpressure.

Figure 5.14 a shows the predicted effective strain rate evolution at the dome pole for constant pressure and different backpressure values. Note that the constant pressure starts at point 0,33 strain value because there is a pressure rise before it.

As can be seen in Figure 5.14 a, when the pressure starts to be constant, in 0.33 of strain value, there is a decrease of the strain rate between 0.3 and 0.5 strain value, which points the hardening of the material. However, this tendency changes at 0.55 strain value, denoting that the material starts a softening behaviour that finished in total damage at around 0.8 strain value, when the material is not able to reach the tension to deal with the pressure.

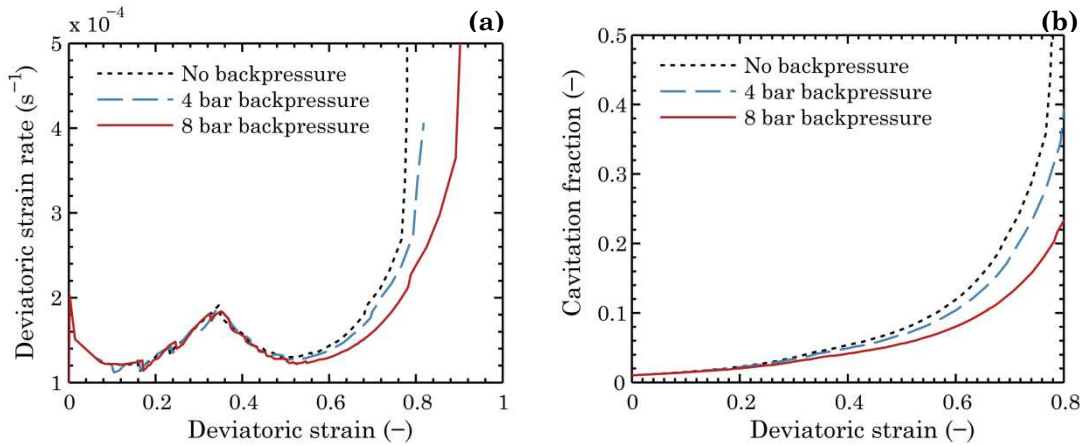


Figure 5.14.: Evolution of effective strain rate (a) and cavity area fraction (b) at the dome pole for Al5083 at 773 K at different stress states.

Figure 5.14 b shows the FE-predicted dome pole cavitation fraction evolution at the same three cases. The cavitation fraction is initially so similar for the three cases but this tendency changed as the strain is higher, having big differences of cavitation fraction (Figure 5.14 b). This has an impact in the strain rate too, having different strain rates at the end of the simulation too for different backpressure values.

The FE performed SPF bulge-test models shows the importance of the cavitation evolution equations for Al5083 aluminium alloy, as SPF components must have a controlled cavitation fraction. The significance of the triaxiality in the cavitation can be denoted, showing the results that the backpressure is an important tool to form by SPF materials that are considered to be susceptible to cavitation damage.

5.7.2 Simulation control approaches effect

In this section the effect the different control strategies will have in the simulations will be studied. This study is important because the pressure-time curves obtained from simulations will be different depending on the followed strategy, so the most accurate and effective one should be determined mainly for two different reasons: the first is that there is no reason to develop complex material models if they are not accompanied with numerically precise pressure-time curves. The second is that having accurate process curves is necessary to validate the material models

Different controls strategies effect

In this section, the effect of different forming control strategies is going to be studied. This control strategies are divided into the Abaqus control strategy, the smoothed pressure control strategy and the smoothed volume control or fluid control strategy explained in the section 5.6.1. The strategies were implemented for obtaining a constant strain rate of $\dot{\epsilon}_{opt} = 1 \times 10^{-3}$ for toroid shape geometry using one integration point as reference.

The graphs from Figure 5.15 show the effect of using the different forming strategies. As can be seen in this figure, pressure time curves have a different shape, being the Abaqus' forming strategy curve the roughest, and the other two show a lineal slope change. Anyway, the pressure control strategy curve show a smooth curve development until the material start to cavitate and a softening behaviour starts, where the control strategy starts to go "crazy". Actually, the Abaqus' strategy is not able to decrease the pressure value, so it is stopped when a lower pressure value than in previous increments is required.

On the other hand, the fluid control strategy shows a smooth pattern during the entire pressure-time curve, so similar to the pressure control strategy curve in the first 600 s. In this two smooth strategies curve the moment the sheet contacts the die is visible too, in the 50 s, where a slope change comes into sight.

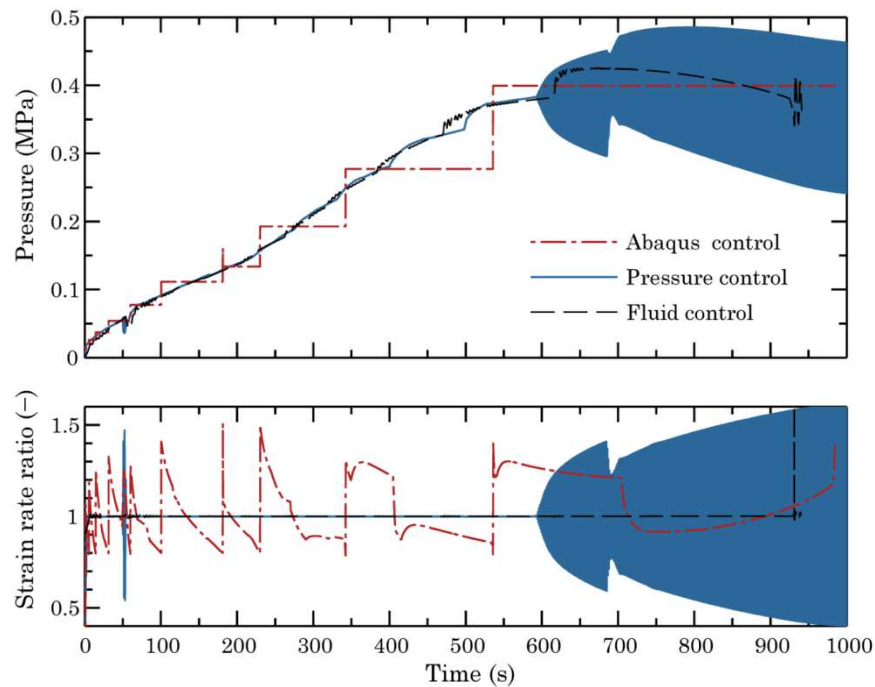


Figure 5.15.: Pressure time curves obtained using different control schemes and strain rate ratios for different control schemes.

The same pattern is visible in the Figure 5.15 where the strain rate ratios are observable for the same simulations. The Abaqus' pressure control strategy shows quite rough answer. This is not a problem for certain material constitutive equations, but not recommendable when the equations describe material mechanism where the history of the forming is important.

Equally, it is visible how the pressure control diverges the result when there is a material softening and the material m value decreases (600 second). Furthermore, the contact instant between the sheet and the die is detectable too in the strain rate ratio graph (50 second).

Looking at these curves, it seems like the smoothed volume control scheme is the most suitable, as it is able to control the forming of complex shapes with strain rate ratios near one. This happens because the volume change is not as material behaviour dependant as pressure control algorithms and the volume change will always be monotonically increasing in contrast to the pressure change. However, this method is a bit more time consuming computationally, so it should be analyzed if it is valid for all the complex shapes.

Integration point number selection effect

The different integration point numbers schemes where implemented for obtaining a constant strain rate of $\dot{\epsilon}_{opt} = 1 \times 10^{-3}$ for toroid shape geometry using smoothed pressure control and smoothed fluid control strategies. It is not possible to use Abaqus' control strategy as it is limited to use only one integration point to calculate the effective strain rate of the increment. In both cases the simulations were made with:

- one integration point (same as Figure 5.15),
- 1 % integration points using (24 integration points in current case) and rejecting using the 0.02 % with the highest strain rate values (5 integration points)
- 3 % integration points using (72 integration points in the current case) and rejecting using the 1 % with the highest strain rate values (24 integration points)

In Figure 5.16 the results for pressure control strategy can be seen. It is reasonable affirming that there is an improvement in terms of divergence of the result, getting to make disappear the problems derived from the material softening.

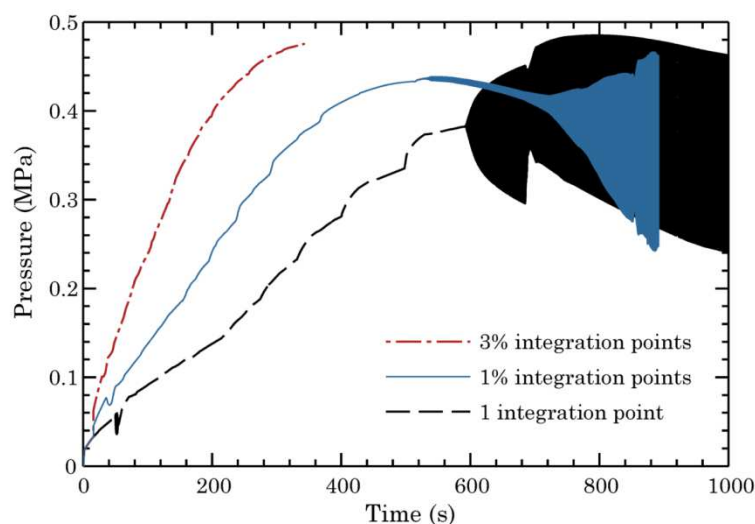


Figure 5.16.: Pressure time curves achieved using smoothed pressure control strategy using different integration point numbers for obtaining the effective strain rate

Anyway, it is also clear that the pressure-time curves change severely, so a different material behaviour will be expected in the reality. For example, the curve for one integration point reaches the total damage around 1000 s, and the curve for 3% integration point there at 350 s.

Similar results can be seen in Figure 5.17, where a smoothing of the curves is visible. Nevertheless, there is no curve divergence to try to avoid, so in this case this strategy is less significant. As well, it is also clear that the pressure-time curves change severely depending on the integration point number, as it happens for the pressure control algorithms case. In both cases, the results are very similar and for the different integration point cases.

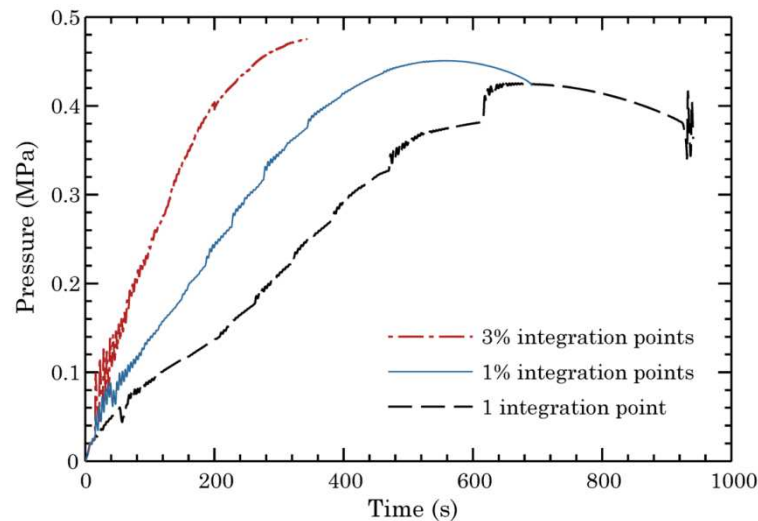


Figure 5.17.: Pressure time curves achieved using smoothed fluid control strategy using different integration point numbers for obtaining the effective strain rate

The results obtained in this section showed that the use of several integration points technique to smooth the curves and reach convergence of them [Luc04, Jar10], changes the pressure-times curve shape dramatically. In the case of Jarrar et al., a 20 % of integration point average and the main 5 % integration point rejection is used, which would be an excessive approach in the case of toroid-shape simulation.

As the pressure-time profiles can be modified in a very severe way, an analysis of the standard deviation is recommended when this technique is used. In contrast, it is interesting for the avoiding the effect of distorted integration points in the control scheme.

During this work, the fluid control technique with 1 % of integration point average for the effective strain rate calculation was picked to complete all the pressure-time curves calculus.

Use of FEM to obtain bulge-test pressure-time curves

Using the model explained in this work, bulge-test pressure time curves were calculated with Abaqus (Figure 5.18) to use them later as input in the SPF device develop during this work (see Figure 5.19, Figure 5.20 and Figure 5.21).

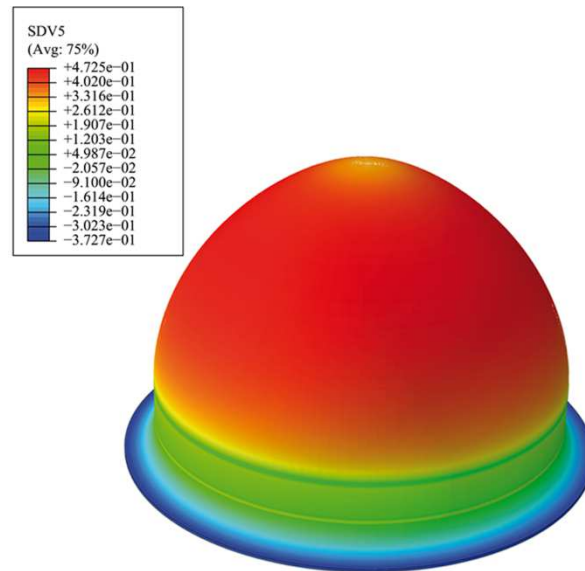


Figure 5.18.: Final geometry and triaxiality map of bulge-test simulation for $2 \times 10^{-4} \text{ s}^{-1}$ control strain rate and 18 bar backpressure results.

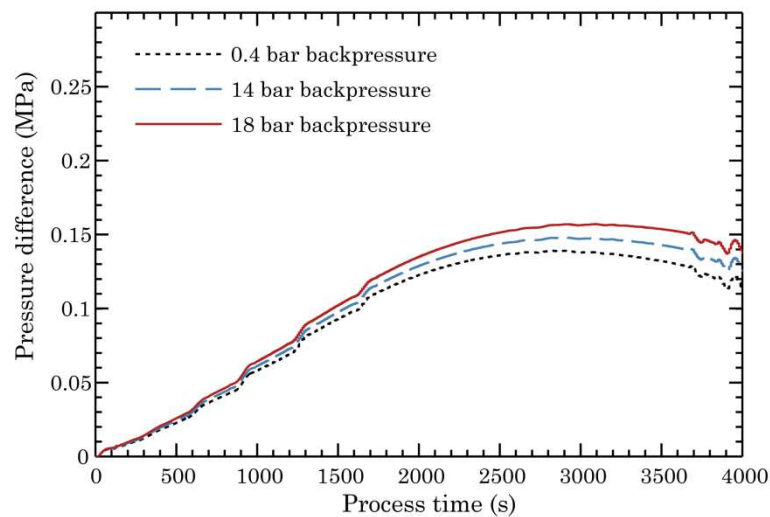


Figure 5.19.: Pressure-time curves for controlled constant strain rate of $2 \times 10^{-4} \text{ s}^{-1}$.

The curves show a similar pattern for the same target strain rate, but there are small differences that increase as the time increases. This happens because of the inhibition of the cavitation behaviour due to the backpressure effect (the pressure difference is between the forming and backpressure chambers).

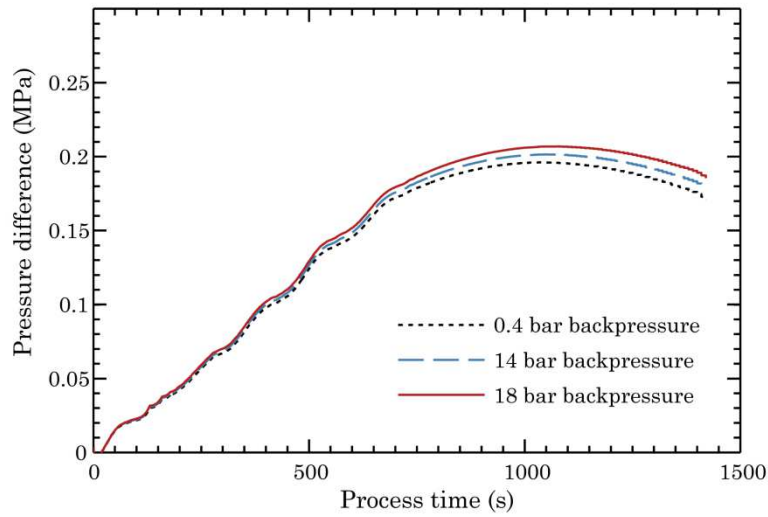


Figure 5.20.: Pressure-time curves for controlled constant strain rate of $5 \times 10^{-4} \text{ s}^{-1}$.

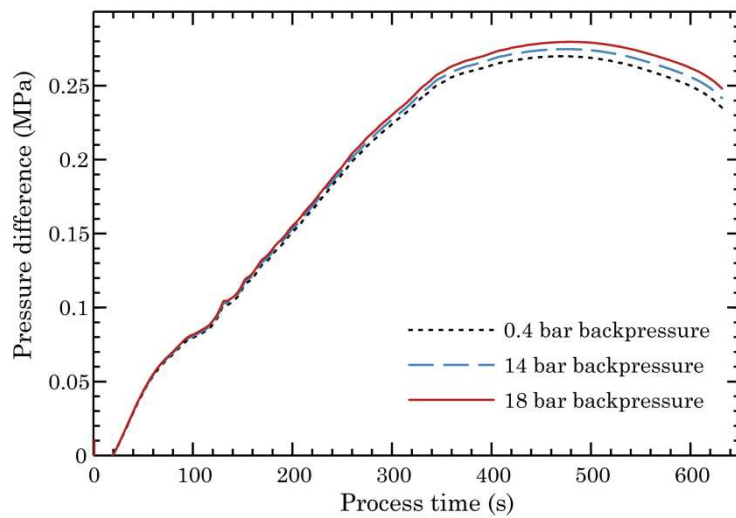


Figure 5.21.: Pressure-time curves for controlled constant strain rate of $1 \times 10^{-3} \text{ s}^{-1}$.

Use of new m max multiscale control strategy

For this section four different strategies have been used to simulate the toroid-shape forming test. The first one at constant strain rate of 2×10^{-4} , the second at constant strain rate of 2×10^{-4} and a backpressure of 1.8 MPa, the third at constant strain rate of 6×10^{-4} and a backpressure of 1.8 MPa, and the fourth at variable strain rate value that follows the maximum m value curve presented before and a backpressure of 1.8 MPa. Figure 5.22 shows the predicted pressure difference profiles that have been achieved with the programmed user subroutine (the pressure difference is between the forming and backpressure chambers). It is observed that in both simulations of 2×10^{-4} constant strain rate control show the same pressure difference in the beginning of the process, and it starts being a distinction as the effect of cavitation becomes relevant at 1800 s. On the other hand, the curves of 6×10^{-4} constant strain rate and the maximum m value strategy is more abrupt and needs less forming time.

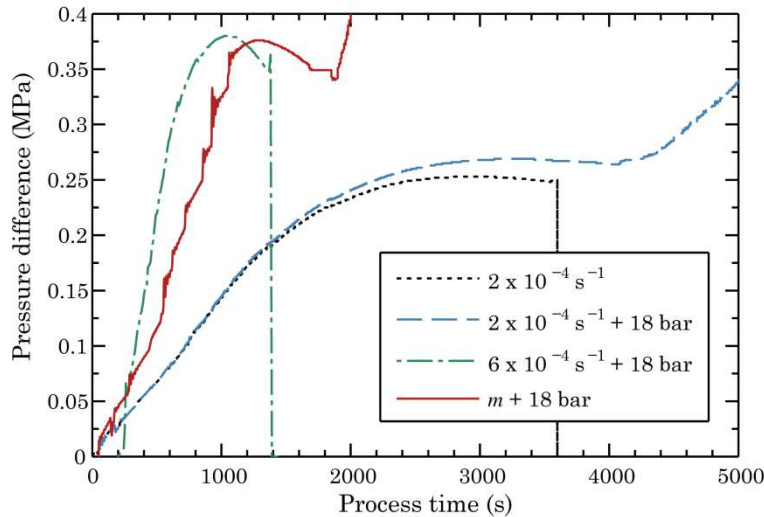


Figure 5.22.: Pressure difference-time curves for toroid shape part with four different strategies: 2×10^{-4} constant strain rate, 2×10^{-4} constant strain rate with backpressure, 6×10^{-4} constant strain rate with backpressure and variable strain rate with backpressure.

Last increments of each simulation are shown in Figure 5.23. It is observed that the strategy with no backpressure and the one at 6×10^{-4} and backpressure cannot fill the die shape, as the damage of the material in the zone A reaches $f_a > 1$ value (Figure 5.24) and therefore the simulation is forced to stop. The other two strategies with backpressure reach to form the toroid shape completely, although it can be seen that there is an improvement in forming time and final thickness for similar fraction of cavitation (Figure 5.24) when a variable strain rate approach is used.

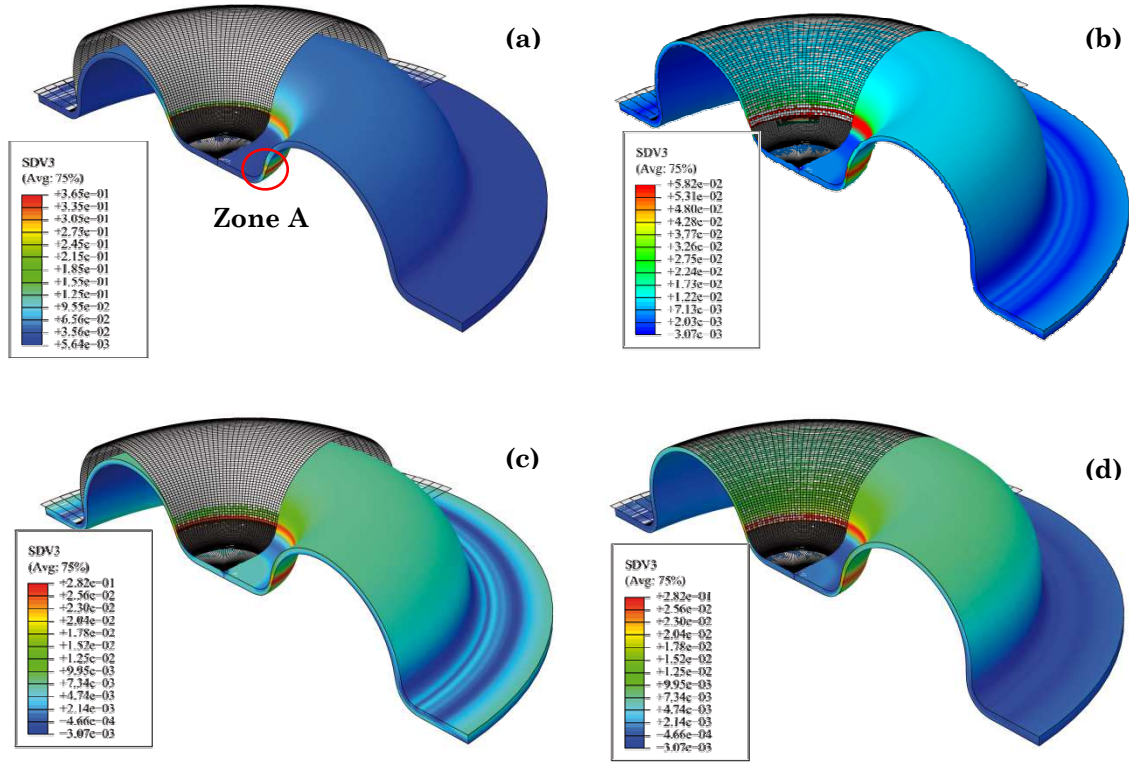


Figure 5.23.: Cavitation fraction last increment maps for toroid-shape simulations, for: (a) target $2 \times 10^{-4} \text{ s}^{-1}$ constant strain rate. (b) target $2 \times 10^{-4} \text{ s}^{-1}$ constant strain rate with backpressure of 18 bar. (c) target $6 \times 10^{-4} \text{ s}^{-1}$ constant strain rate with backpressure of 18 bar. (d) m max strategy with backpressure of 18 bar.

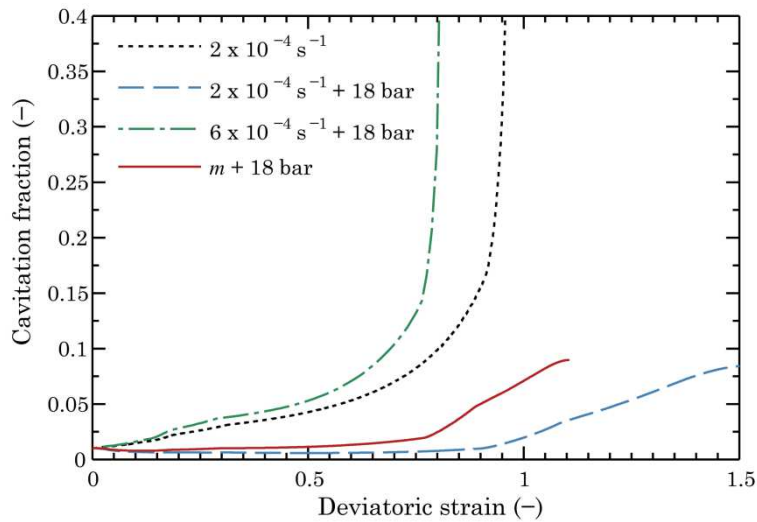


Figure 5.24.: Fraction of cavitation in A area (Figure 5.23 a) of the toroid shape for four simulations.

The material's loading state is a very important factor that affects the void nucleation, growth and coalescence. As it was explained in this chapter (see Figure 5.5), the lower the triaxiality factor, the more strained the material will cavitate.

In the Figure 5.25 can be the triaxiality factor maps of the $2 \times 10^{-4} \text{ s}^{-1}$ without backpressure test for two forming times, during the forming and the last increment before failure. The triaxiality in the non-contact area (red colour), is about 0.7 value.

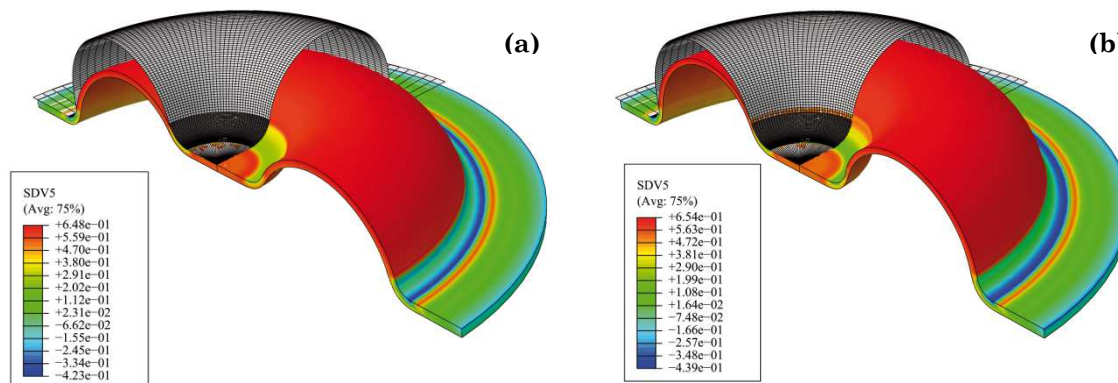


Figure 5.25.: Triaxiality coefficient value maps (a) during the forming and (b) last increment for toroid-shape simulation the pressure-time curves obtained in the experiments for target $2 \times 10^{-4} \text{ s}^{-1}$ constant strain rate.

On the other hand, the values for the contacted area have a minus value, as the material is in compression state. At this point, a remarkable situation highlights, as the equations presented by Cocks and Ashby [Coc82], which is used in this work to represent the cavitation fraction behaviour, says that a negative triaxiality factor could not only inhibit the cavitation but decrease it.

In the Figure 5.26 the results for the target $2 \times 10^{-4} \text{ s}^{-1}$ constant strain rate with backpressure test are shown. In this case, the non-contacted area shows a triaxiality factor around 0.3 value. Similar values are registered for $2 \times 10^{-4} \text{ s}^{-1} + \text{back}$ and $m \text{ max} + \text{back}$ tests, although in these cases the value rises to around 0.35 ratio value.

In the case of the last increment value (when the geometry is obtained), the triaxiality value is negative as expected, because the material is compression.

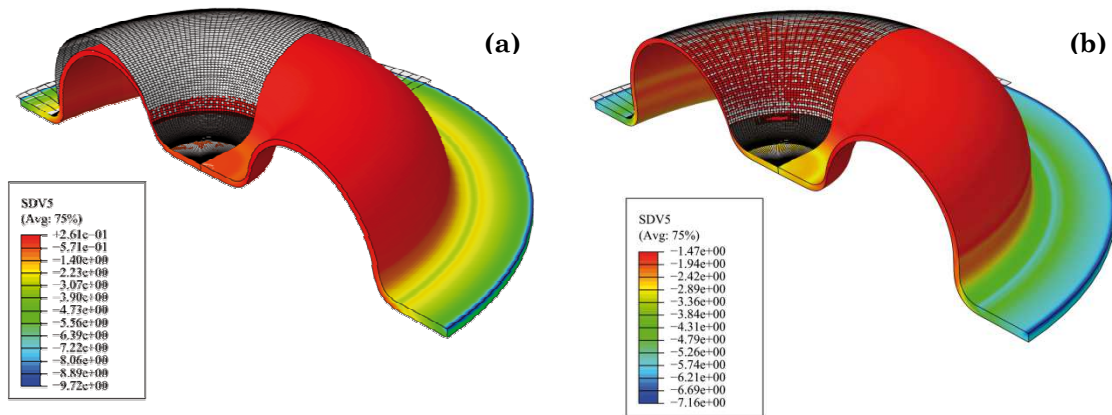


Figure 5.26.: Triaxiality coefficient value maps (a) during the forming and (b) last increment for toroid-shape simulation the pressure-time curves obtained in the experiments for target $2 \times 10^{-4} \text{ s}^{-1}$ constant strain rate with backpressure of 18 bar.

5.8 Closure

Several optimization strategies has been presented by different authors as explained in Chapter 2. Nevertheless, only some of the have been prepared for materials that suffer from damage.

In this chapter, finite element analysis has been carried out to understand and optimize the superplastic behaviour of Al-5083-SPF. The material subroutine used in the analysis is based on the constitutive model that accurately captures the behaviour of the aluminium alloy under consideration.

For this aim, two different geometries were simulated: a bulge-test, where the interaction between the die and the sheet is minimized, and a toroid shape, where the contact has an important role. Using material constitutive equations proposed in the previous chapter and implemented in Abaqus Standard, different optimization strategies are presented, focused in two main areas:

- The improvement of accuracy of the control in Abaqus, having strategies that have no convergence problem but smooth control schemes. For this aim, a smoothed fluid control strategy novel technique was developed, using a cavity volume control instead of gas pressure control.
- The optimization of the SPF process itself, using the mechanism-based material model as basis for exploiting maximum superplastic capabilities of the material during the process.

To conclude, it was shown that this new forming strategy uses the hyperbolic constitutive equations for reaching the maximum m value at each strain, controlling the strain rate. Furthermore, this strategy may allow the achieving of simulated parts with same cavitation fraction using less forming time and better thickness profile.

SPF EXPERIMENTAL TESTS

Synopsis

Experimental tests are necessary to validate the numerical model implemented in Abaqus and the forming strategies applicability presented in Chapter 5. This is the only system to ensure that the suppositions made for the mentioned implementation are assumable. Furthermore, it is important to know if the material constitutive behaviour defined using uniaxial tensile tests is accurate in blow SPF. Finally, experimental tests give a realistic idea if the maximum m value strategy presented in this work is applicable in real industrial environment.

To validate the material model implemented, different bulge-tests at several target strain rates, backpressure values and strain values were conducted. The bulge-test experimental results were compared to numerical ones and showed a good agreement in height and thickness in the pole of the dome of the parts for different strain values

To validate the control strategy approaches, different toroid-geometry tests were conducted. The experimental thickness profile results and the process time of each strategy validated the maximum m strategy presented in Chapter 5 for time optimization without losing quality of the part.

6.1 Introduction

Experimental tests are necessary to validate the numerical model implemented in Abaqus and the forming strategies applicability presented in Chapter 5. This is the only system to ensure that the suppositions made for implementing the numerical model are assumable. Furthermore, it is important to know if the material constitutive behaviour defined using uniaxial tensile tests is accurate in blow SPF. Finally, experimental tests provide a realistic idea if the maximum m value strategy presented in this work is applicable in real industrial environment.

In the first part of this chapter, a blow forming SPF facility developed in Mondragon Unibertsitatea is presented. The requirements for a facility that is capable of forming Ti6Al4V and Al-5083-SPF alloys are explained, and the design of this facility is described. In addition, the design concept of the two dies used for SPF forming are shown, and the manufacturing of the bulge-test die and toroid-shape die is explained.

In the second part of this chapter, results of bulge-test experiments carried out using pressure-time-curves obtained following procedures explained in Chapter 5 are depicted. The bulge-tests were conducted at different target strain rate, strain and backpressure values. Validation of the material constitutive equations presented in Chapter 4 is out, comparing experimental and numerical data of height, thickness, grain size evolution and cavitation area fraction evolution in the pole of the dome of different parts.

In the third part of this chapter, results of toroid-shape experiments conducted for validating the process time optimization strategies are shown, comparing real experiments at target constant strain rate and maximum m value strategies.

6.2 SPF facility

6.2.1 Specifications of the facility

Temperature requirements

As it was explained in the Chapter 2, the superplastic condition is given in a narrow range of temperature. Actually, superplastic conditions are usually determined for a certain temperature value, in which the maximum elongation has been achieved [Pil89]. Therefore, a homogeneous temperature distribution was identified to be necessary, so the process should be as isothermal as possible.

The high temperatures of these process are very important too, so it was determined that the temperature of the facility should reach 950°C, to be able to form Ti6Al4V and Ti6Al2Sn4Zr2Mo [Nie05].

Gas control requirements

The need of having synchronized forming pressure and backpressure was defined, as superplastic material that suffer from cavitation and the mitigation of this behaviour by using hydrostatic pressure was understood to be necessary for this work. Equally, a good sensorization of booth pressure values was determined to be very important.

Mechanical requirements

The need of materials that have good isolation behaviour was conclusive. However, this should be combined with certain die closing force to maintain hermetical chambers inside the mould. Equally, part of the mould should be hold to a moving part that helps to close and open the die having the disadvantages of unions at high temperatures.

6.2.2 Design of a superplastic forming prototype

The superplastic forming prototype was designed using different modules (Figure 6.1). Firstly, an SPF oven was designed. This SPF oven should be removable from a servomechanical press, and should have good isolation and enough strength for the closing force. Secondly, there is a need for two pressure inlets control and measurement. Finally, a temperature control and measurement device is necessary.

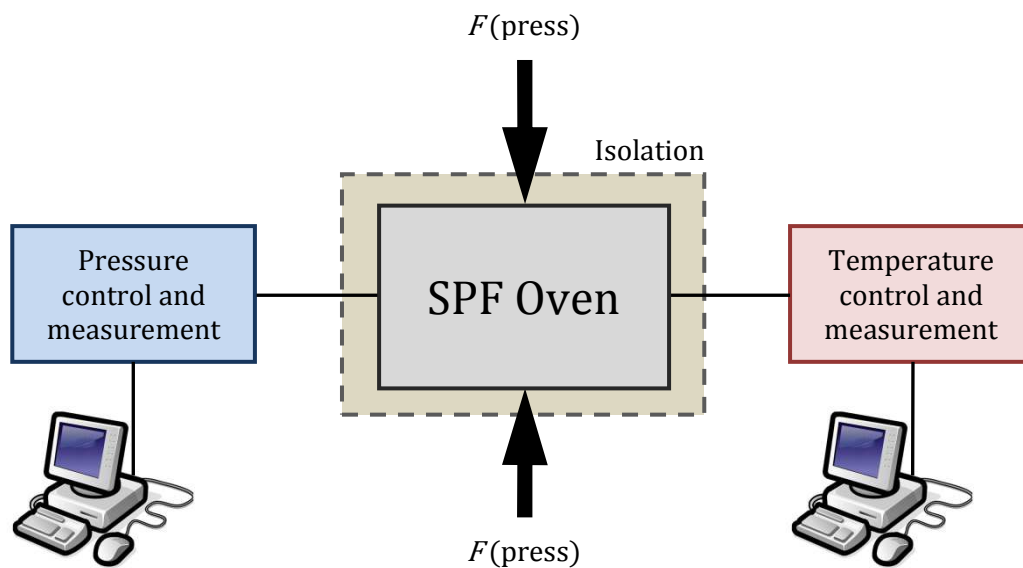


Figure 6.1.: Schematic representation of the SPF prototype .

A picture of the set of the SPF prototype can be seen in Figure 6.2. The oven is inserted in a mechanical servopress with a pressing force up to 400 Tn. The main advantage of using this kind of press in SPF processes is that there is no need of synchronizing the forming pressure and the closing force as it happens in a hydraulic press.

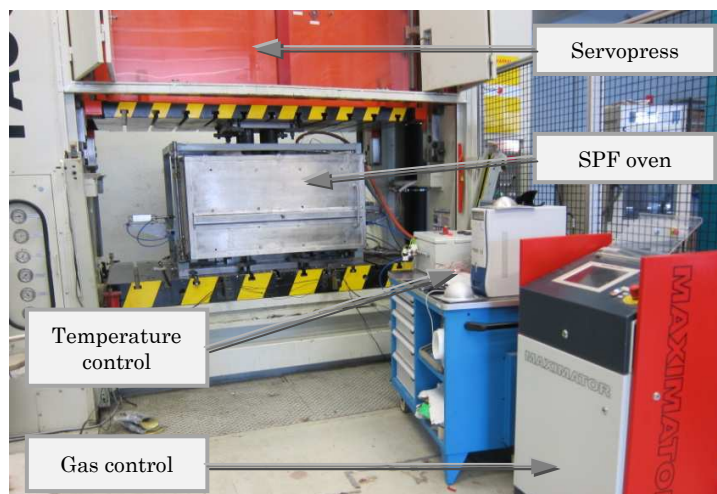


Figure 6.2.: Set of the SPF prototype in the servomechanical press.

Oven structure

The oven structure is divided into two main parts, a mobile and a fixed one (see Figure 6.3). This split is necessary to have access to the blown part after the forming. For heating the dies, two heating plates are used (2), made by XN40SPF Aubert & Duval material (specifically developed for SPF). Twelve multicell radiating heaters are inside these plates.

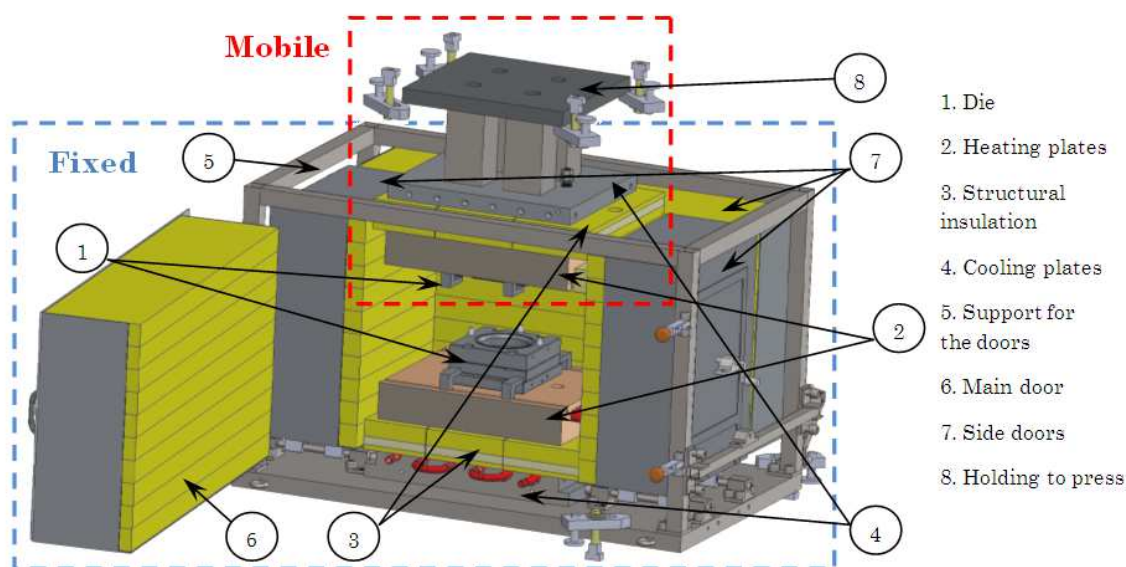


Figure 6.3.: Schematic representation of the SPF oven.

Different thermal insulation materials reduce heat transfer to the press and maintain the temperature homogeneity. For this aim, the structure (5) has four doors, one is the main door (6) and the other three side doors (7) where designed to make an efficient thermal insulating closing when the die is closed, allowing the movement of the mobile part when the part should be catch (Figure 6.4).

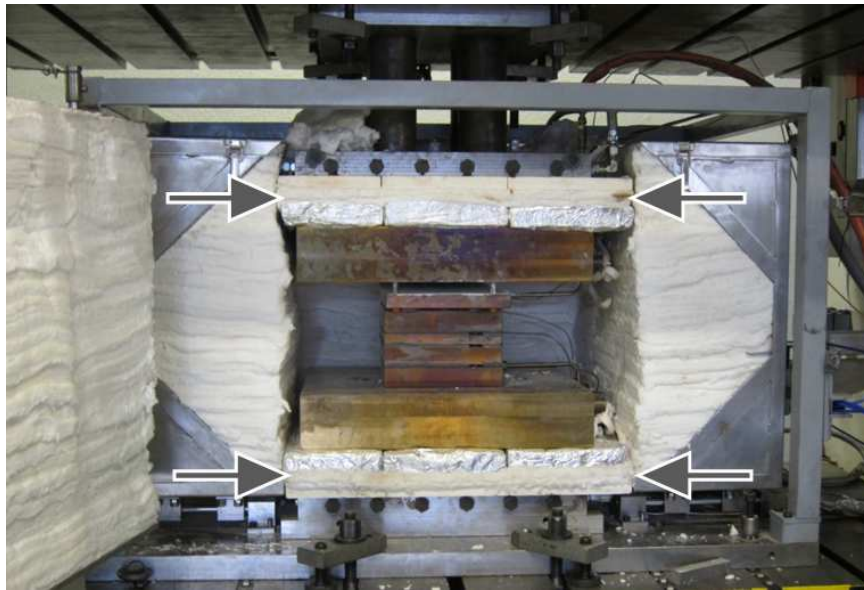


Figure 6.4.: Movement of side doors for temperature sealing.

The direct contact with the servopress is made by a double “sandwich” structure of a heating plate, insulation panels and a cooling plate with an internal drilled path for a cooling fluid (see Figure 6.5). The same configuration is used in the top and the bottom of the whole structure, as can be seen in Figure 6.3, and it was designed to protect the mechanical servopress.

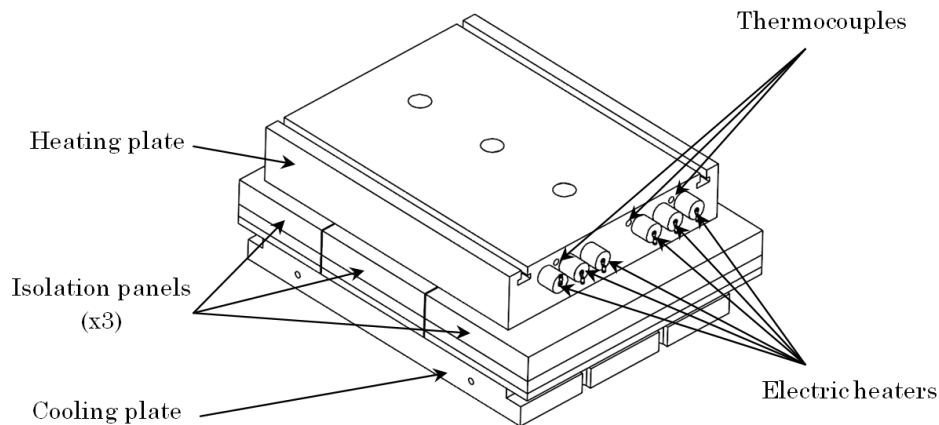


Figure 6.5.: “Sandwich” structure that shows a heating plate this electric heaters and thermocouples, insulation panels and cooling plate .

Each of the heating plates has six electric radiation heaters controlled by three zones directed by three thermocouples.

The bottom part holds the complete structure to the press bed plate, and the top part to the slide of the press. Both sandwich structures were united using three long screws (see Figure 6.6). There is a high temperature difference between the heated plate (3), which

should have reach the 950 °C, and the cooling plate (1), which should have maintained to less than 50 °C. Therefore, two strategies were followed to avoid the fracture of insulation ceramic plates (2) due to the dilatation problems: the first was to cutting the ceramic insulation plates into three different parts(see Figure 6.6).

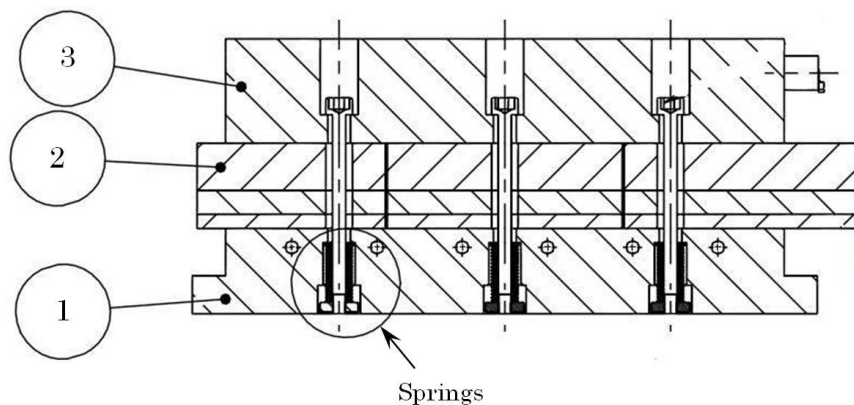


Figure 6.6.: “Sandwich” structure of (1) cooling plate, (2) insulation panels and (3) heated plate .

The second one was to use Belleville springs to maintain the closing force to a minimum value to hold the plates to the press, ut allowing the expansion of the heated plate without increasing the holding force considerably (see Figure 6.6).

6.2.3 Design and manufacture of a die for superplastic forming

In this work two types of geometries were formed. These geometries are the bulge-test, which is used to validate the material model, and the toroid shape, which takes into account contact behaviour with the die, presented and simulated in the chapter 4.

Refractory stainless steel die

The bulge-test die was designed to be able to do free bulge specimens of 72.5 mm diameter, as can be seen in Figure 6.7. The material used was stainless steel AISI 310s. Because of the problems of achieving plates thicker than 50 mm made of this material, the die was designed using a group of different plates.

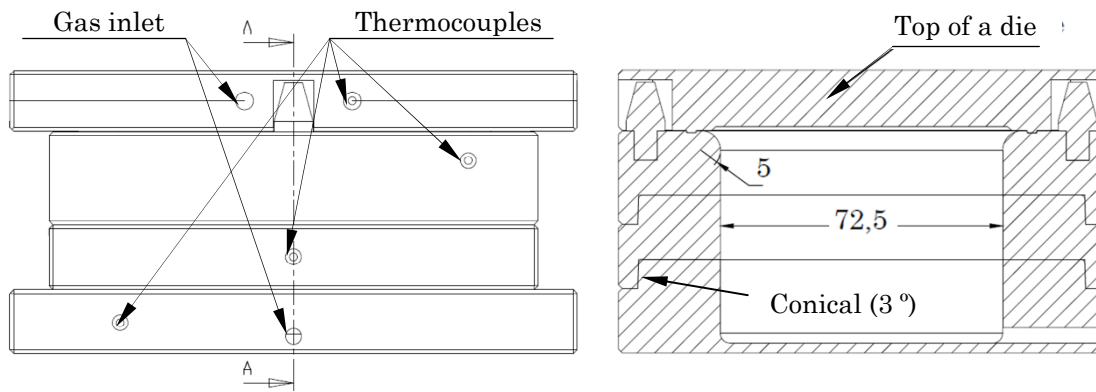


Figure 6.7.: Bulge-test die designed for this work.

Special attention must be paid to the two gas inlets, particularly prepared to use backpressure type forming scheme, using pressure difference between the two chambers. Therefore, the joining of the different plates is made using a conical union of 3° to avoid gas leakage. Four different thermocouples were added to control the homogeneity of the temperature trough the die. One is in the top of the die, and the other three in the different plates at different depths.

Refractory concrete die

For manufacturing the toroid shape was made using a refractory concrete material. The concrete die was manufactured using silicone pattern inside an aluminium mould of 72.5 mm diameter (see Figure 6.8 a). The bulge-test die was used as base to have sealing of the chambers and thermocouples. The concrete geometry was inserted in the cavity of the bulge-test (see Figure 6.8 b).

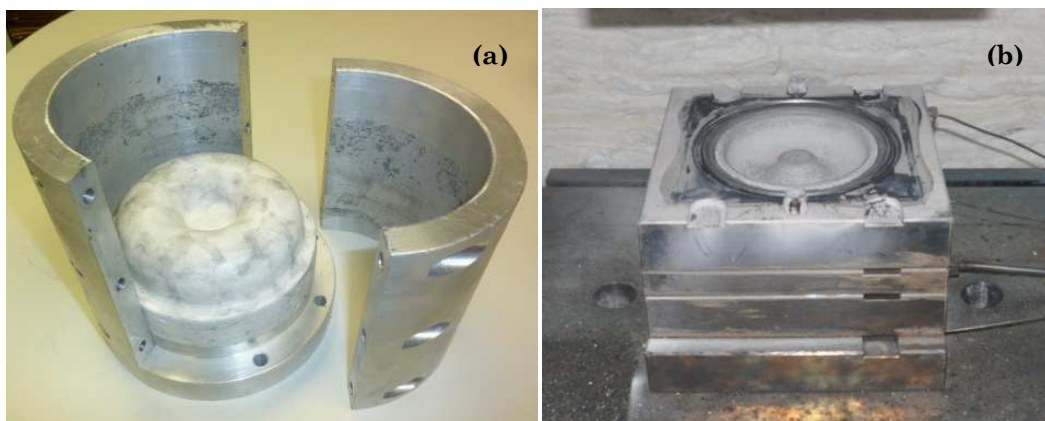


Figure 6.8.: . Concrete die production (a) silicone pattern and (b) final tooling.

6.3 Gas forming test methodology

The tensile test presented in this document can be divided into three different groups:

- Controlled strain rate tests for different backpressure values
- Maximum m value tests for different backpressure values

The first was conducted for validating the material model, and the second for validating the maximum m value approach as strategy to reduce the forming time without losing material properties.

In this work, the followed methodology was to obtain a pressure time curves by finite element method and this curves were used to form the tests. Sensors directly measured the forming pressure and backpressure during the test. Finally, these were used to simulated again with the real pressures to validate the material model. It must be highlighted that all the numerical results shown in this chapter are obtained conducting a final simulation with the experimentally measured pressure values. The decision of following this methodology was taken since there is an appreciable discrepancy between the targeted and the real pressure inside the die, which is complex to set up.



Figure 6.9.: Set of tests made at different backpressure and strain values for $2 \times 10^{-4} \text{ s}^{-1}$ strain rate.

For the validation of the material model three target strain rate (2×10^{-4} , 5×10^{-4} and $1 \times 10^{-3} \text{ s}^{-1}$), three backpressure values (0.4 bar, 14 bar and 18 bar) and four stops were made, having finally 36 different bulge-tests (in Figure 6.9 twelve of them can be seen). The stops were calculated by using the maximum forming time t_r (when the rupture of the sheet is achieved), and other three tests are conducted with same target strain rate and backpressure values to times of $t_1 = t_r/4$, $t_2 = t_r/2$ and $t_3 = 3t_r/4$.

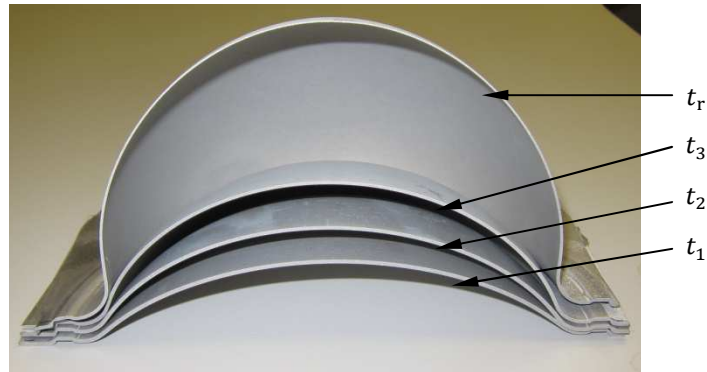


Figure 6.10.: Section of different interrupted bulge-test ed at $5 \times 10^{-4} \text{ s}^{-1}$ target strain rate and 18 bar backpressure.

For validating the material model, four different parameters were measured in the pole of the dome: The height, the thickness and microstructural parameters in the pole. The height and the thickness were measured using This microstructural parameters (grain size and cavitation area fraction) were analyzed only .for backpressure values of 0.4 bar and 18 bar, and three stops of t_1 , t_2 and t_3 . The microstructural parameter determination was carried out following the methodology explained in Chapter 3 for tensile tests.

The results obtained in the experimental tests can be seen in the next section, with the validating of the material model behaviour.

6.4 Material model validation by bulge-test s

Figure 5.19, Figure 5.20 and Figure 5.21 from Chapter 5 show the predicted pressure difference profiles that were achieved with the programmed user subroutine. The numerical results showed in this section were calculated using the experimentally measured pressure-time curves.

6.4.1 Dome pole height

The results for the three different target strain rate paths at 0.4 bar backpressure situations are shown in Figure 6.11.

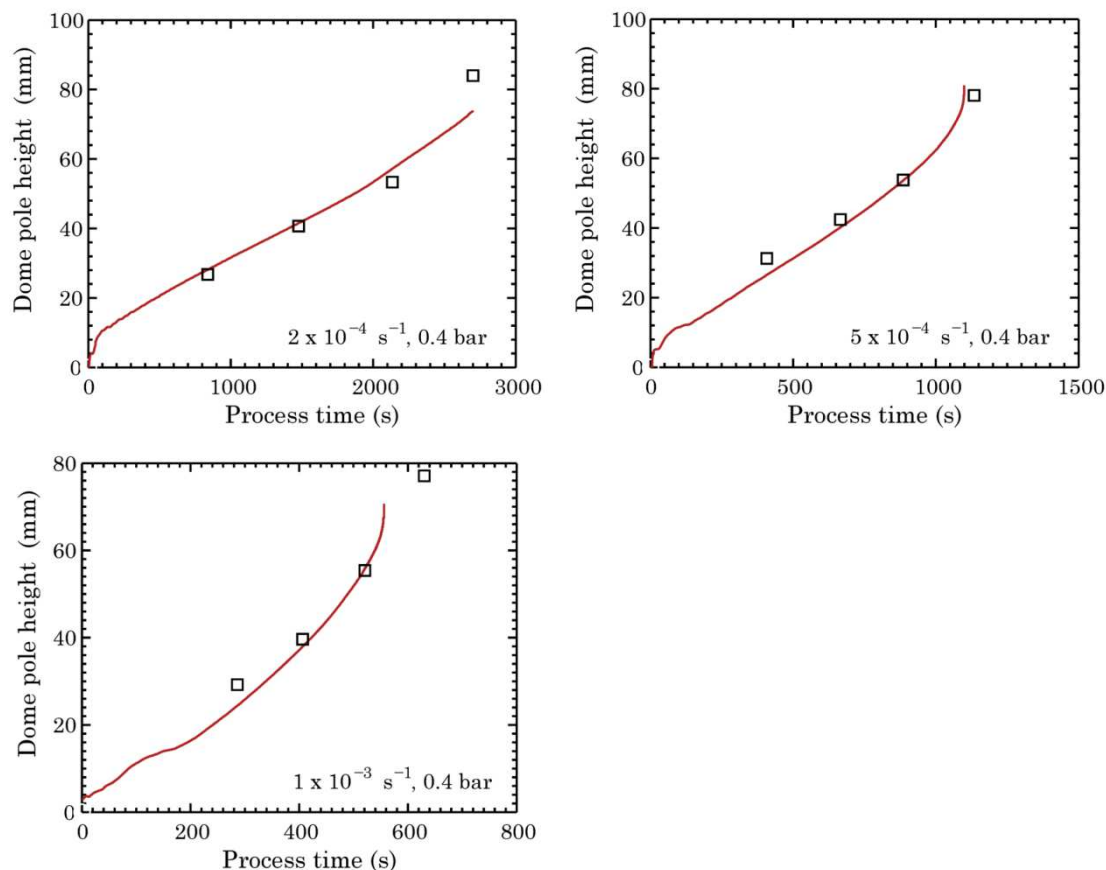


Figure 6.11.: Comparison between simulated (red) and experimentally measured (squared points) height of the pole of the dome for different strain rates applied 0.4 bar backpressure.

The results show a good agreement, but it can be seen a tendency in terms of too severe damage behaviour at the $1 \times 10^{-3} \text{ s}^{-1}$ target strain rate path experiment and not enough damage behaviour for the $2 \times 10^{-4} \text{ s}^{-1}$ strain rate path experiment. The $5 \times 10^{-4} \text{ s}^{-1}$ strain rate path experiment shows the best agreement between the experimental and numerical data.

This tendency is not repeated at 14 bar experiments. As can be seen in Figure 6.12, the $2 \times 10^{-4} \text{ s}^{-1}$ and $1 \times 10^{-3} \text{ s}^{-1}$ strain rate path experiments show a weak damage behaviour, and $5 \times 10^{-4} \text{ s}^{-1}$ experiment is the most accurate. Anyway, overall the experimental and numerical data show a good agreement too.

Another effect that can be seen in this figures is the synchronized rising of the forming and backpressure. To have the 14 bar backpressure, the two pressure are rose together before the forming stage starts. As the synchronization of this rising consumes time, the sheet is formed around 20 mm height in the first 700 s.

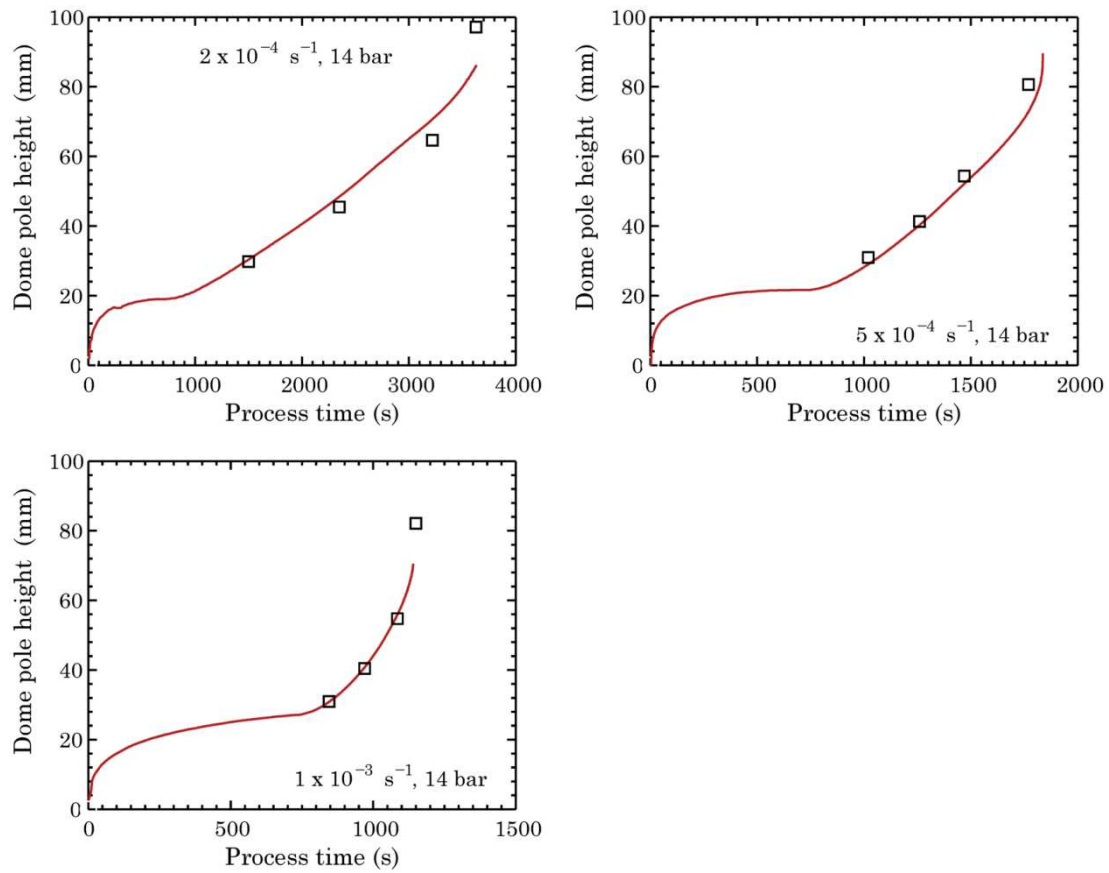


Figure 6.12.: Comparison between simulated (red) and experimentally measured (squared points) height of the pole of the dome for different strain rates applied 14 bar backpressure.

Finally, the results for 18 bar can be seen in Figure 6.13. They show similar effects related to the good agreement in the stages where the damage is zero or low, and more discrepancies in the case of the complete failure of the part (last square).

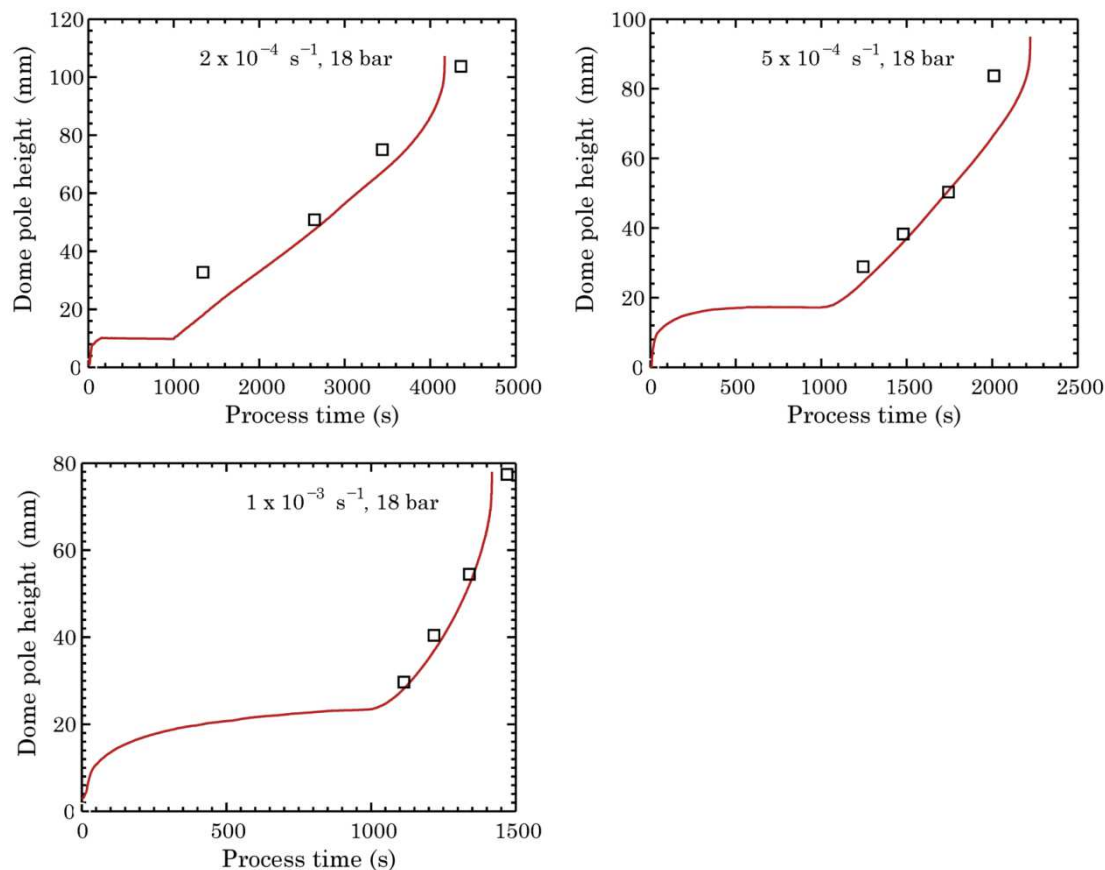


Figure 6.13.: Comparison between simulated (red) and experimentally measured (squared points) height of the pole of the dome for different strain rates applied 18 bar backpressure.

Similarly, the backpressure effect is more pronounced, being increased to a first deformation stage of 25 mm height during the first 1000 s.

About the experimental values, it is expected to obtain the highest height at lowest strain rates. Furthermore, the benefits due to backpressure effect, which are evident as the test reach the total damage at higher bulge values, are more pronounced when the strain rates are lower.

6.4.2 Dome pole thickness

The thickness on the pole of the dome was equally measured during this work. The results can be seen in Figure 6.14, Figure 6.15 and Figure 6.16. In this case too, there is an initial backpressure rising period where the thickness should maintain at 1.5 initial thickness values but it falls between 1.4 mm and 1.3 mm. As explained before, this effect happens due to technical reasons (pressure control precision) and is more relevant the higher is the backpressure value.

On the other hand, the thickness values show a good agreement too, showing little discrepancies in the late stages of the damage behaviour.

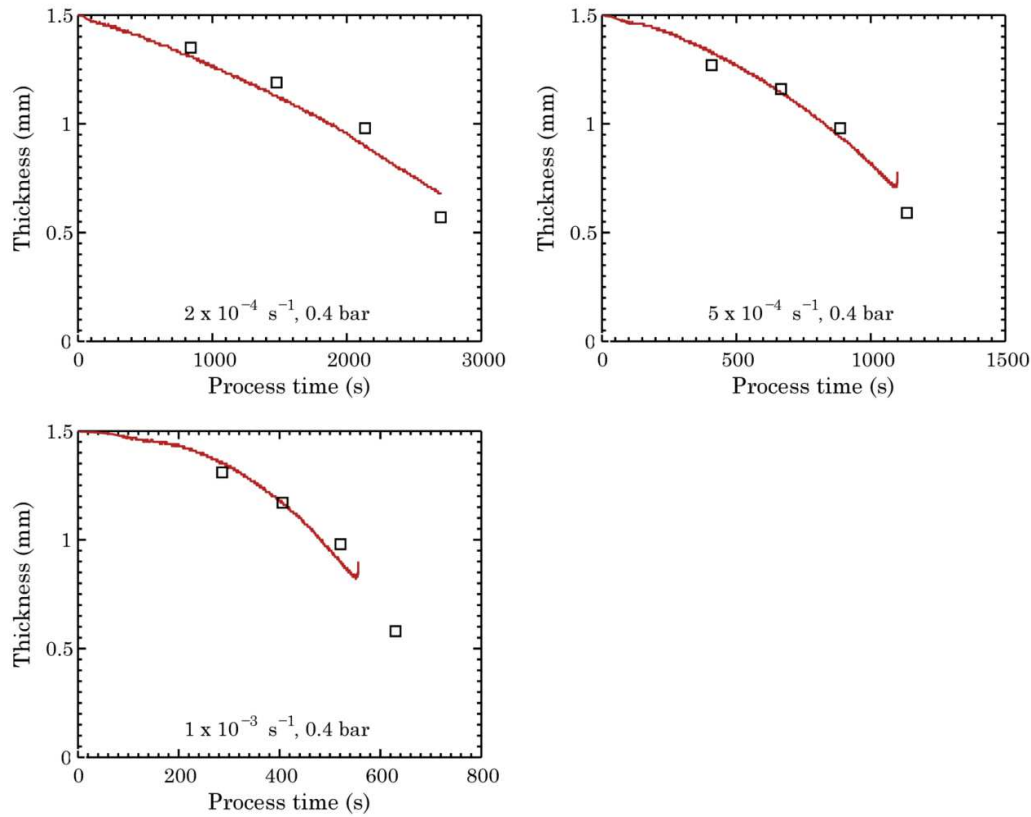


Figure 6.14.: Comparison of simulated and experimental thickness for 0.4 bar bulge-tests.

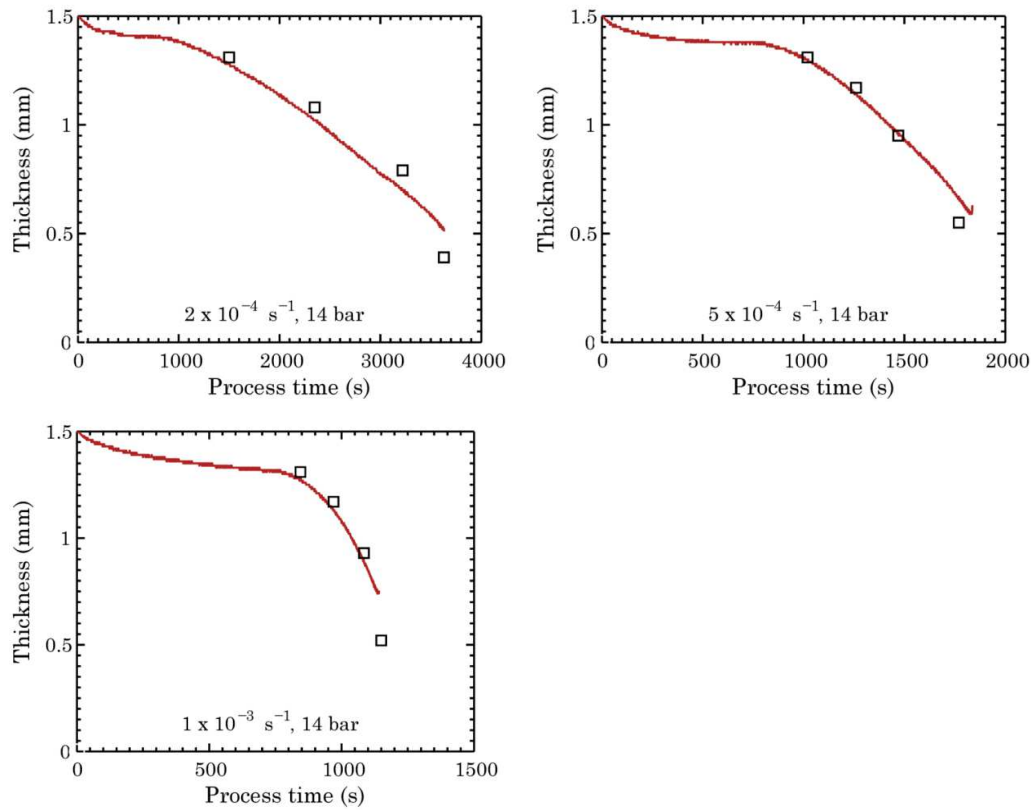


Figure 6.15.: Comparison of simulated and experimental thickness for 14 bar bulge-tests.

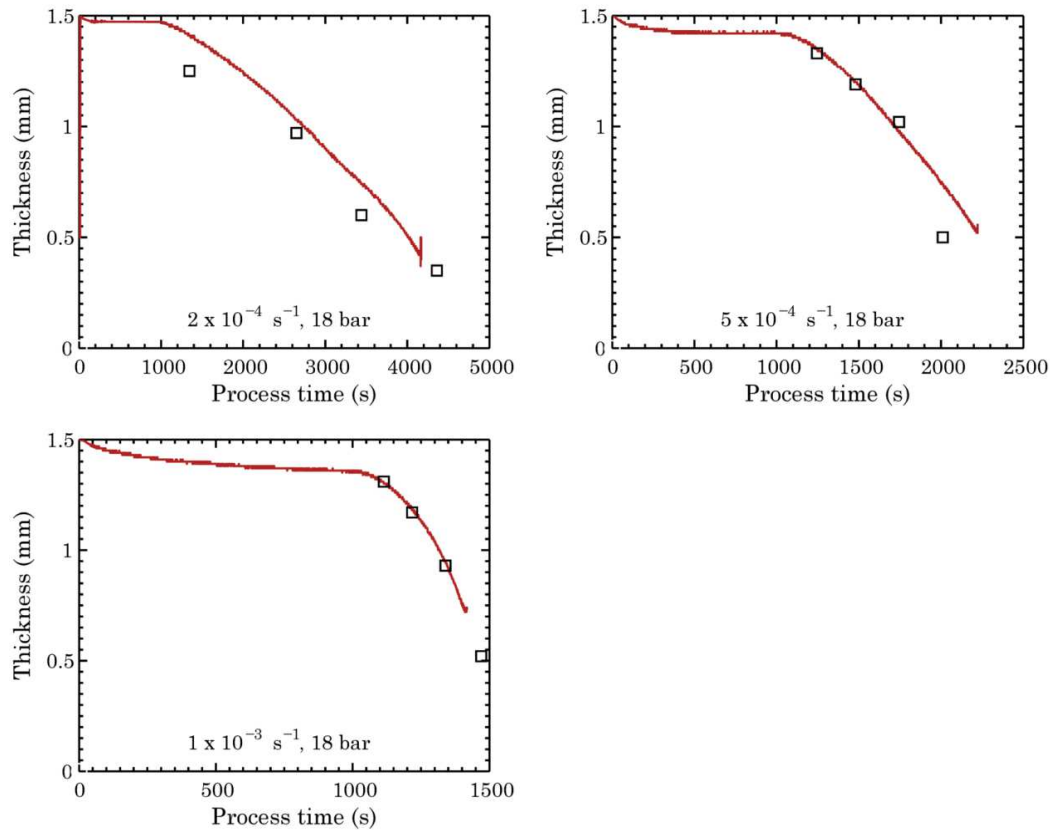


Figure 6.16.: Comparison of simulated and experimental thickness for 18 bar backpressure.

From a mechanical point of view, the material model shows a good agreement with the biaxial experimental results, even when damage is present in the material. However, a better analysis of damage behaviour is necessary to calibrate the softening of the material and the presence of failure. This will be more extensively analysed in next section. In general, all the tests that reached the failure have a minimum thickness of 0.5 mm, but the height of them are different. Looking at the figures of mechanical data (height and thickness results), it can be deduced that the change of strain rate implies mainly an improvement in terms of thickness profile homogeneity (strain rate sensitivity). On the contrary, the effect of the change in the backpressure seems to have only effect in the cavitation fraction.

6.4.3 Cavitation behaviour

The cavitation behaviour is an important effect that appears only in some alloys like Al-5083-SPF aluminium alloy. Having properly characterized damage model is even more important in superplastic forming, because the hydrostatic stress in the material is controllable due to the low stresses are inherent of superplasticity. Therefore, the backpressure effect will be more effective when the flow stresses are lower, consequently, when the strain rate is lower. Results can be seen in Figure 6.17 and Figure 6.18, where the blue dashed line stands for failure time of the experimental test.

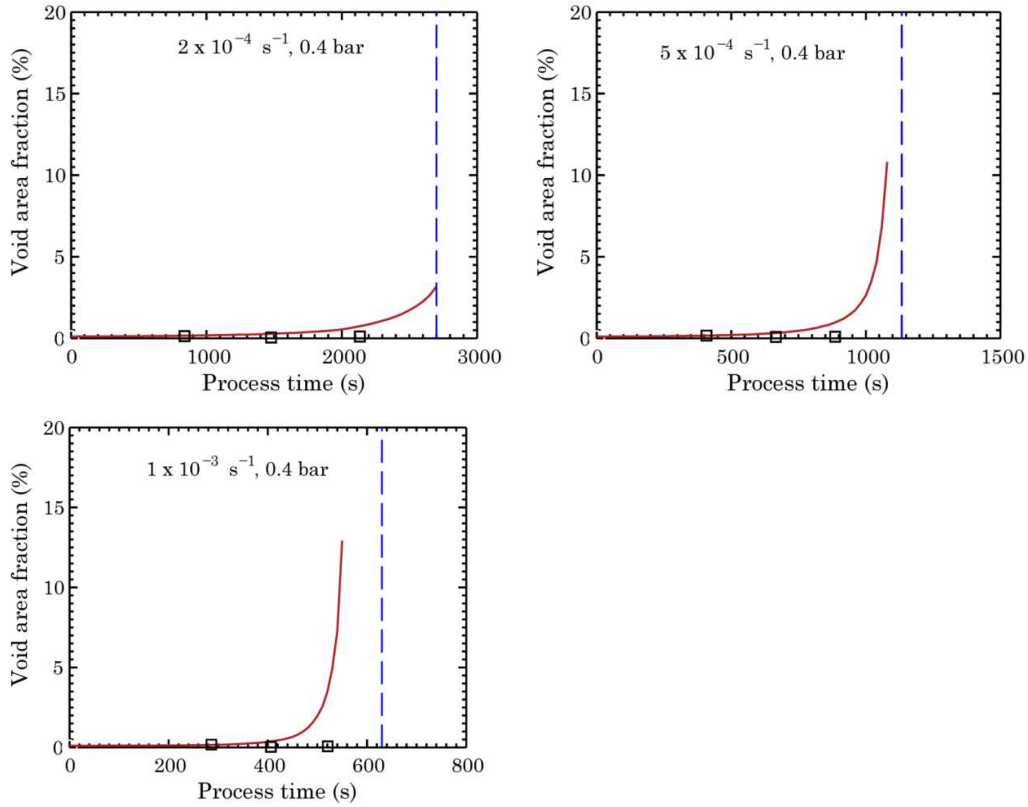


Figure 6.17.: Comparison of simulated and experimental cavitation for 0.4 bar tests

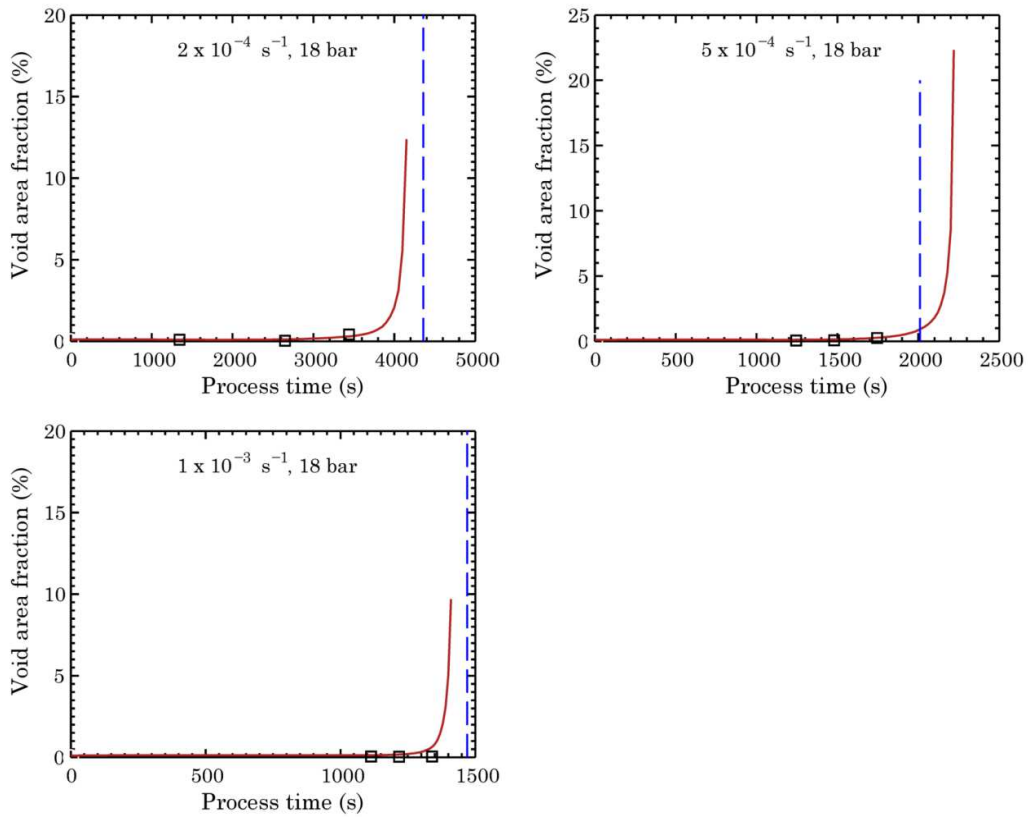


Figure 6.18.: Comparison of simulated and experimental cavitation for 18 bar tests

The effect of the backpressure have been proven with the achievement of higher bulge domes using the same pressure change strategies varying only the backpressure of the process (see *Figure 6.19*).

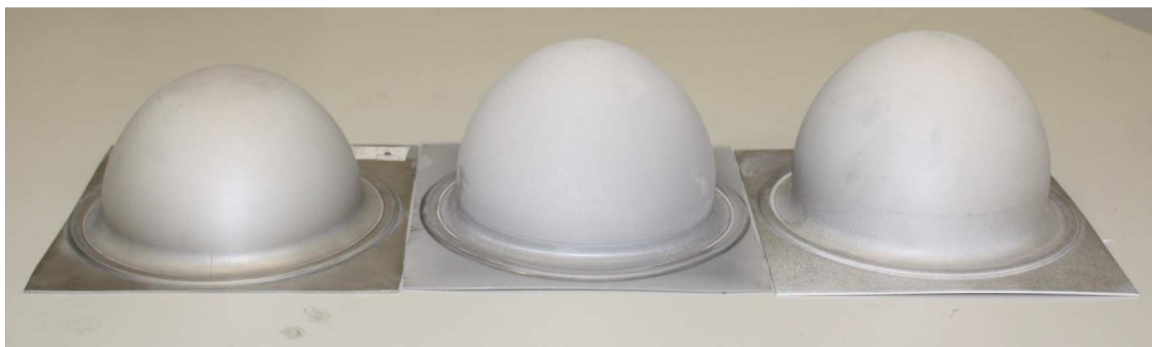


Figure 6.19.: Different bulge-test s obtained at backpressure of 0.4, 14 and 18 bar from the left to the right using the same $2 \times 10^{-4} \text{ s}^{-1}$ target strain rate forming history.

Nevertheless, the cavitation experimental results do not illustrate the same effect, and there is a clear inconsistency between the void area fraction values of numerical and experimental data.

The heterogeneity of the microstructural values, which are considered homogenous mechanism in the models for practical reasons, could lead to errors. A need for a comprehensive analysis with different techniques is highlighted in this work.

6.4.4 Grain size behaviour

The grain size growth behaviour results are illustrated in *Figure 6.20* and *Figure 6.21*. Similar to the cavitation fraction results, there is an inconsistency between the experimental and numerical results. Nevertheless, some results show no growth rate or even values lower than the initial grain size. This effect can be due to the grain size distribution is more heterogeneous than was expected..

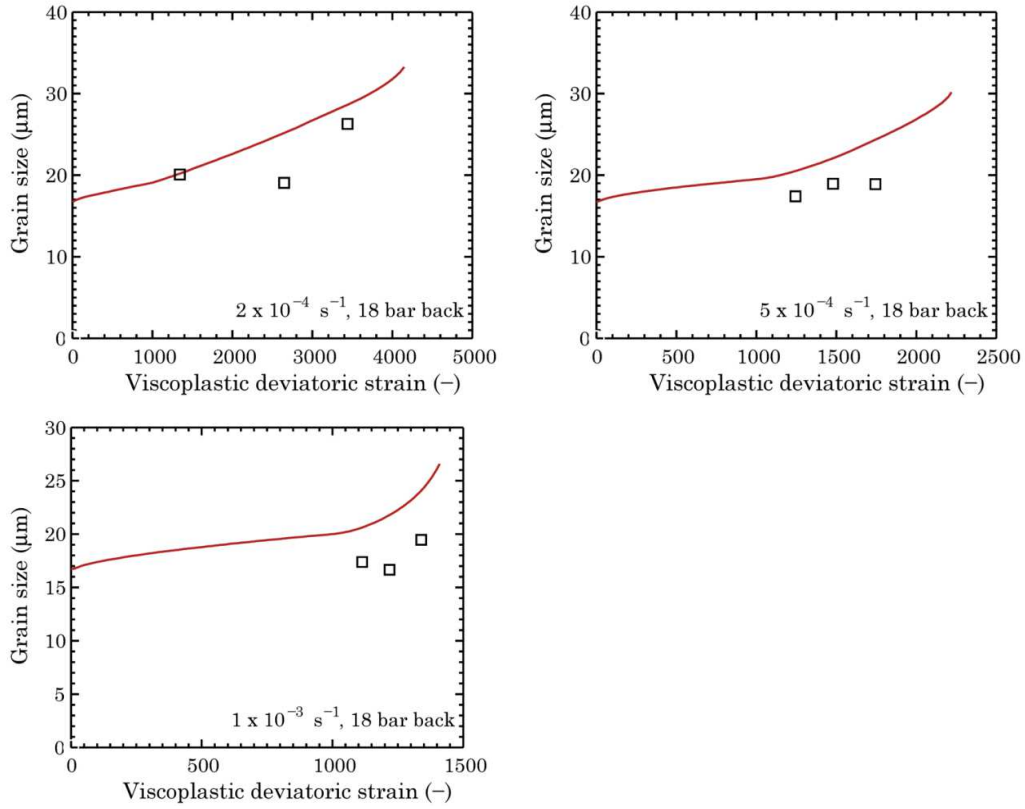


Figure 6.20.: . Comparison of simulated and experimental grain size for 0.4 bar tests

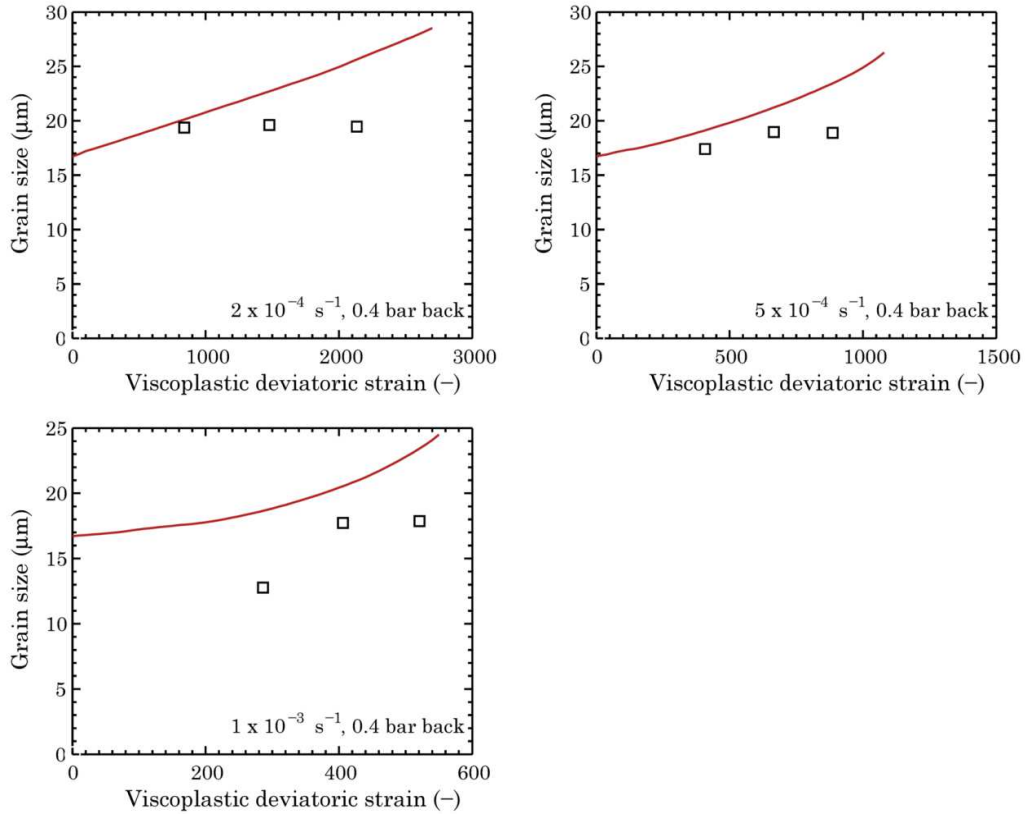


Figure 6.21.: . Comparison of simulated and experimental grain size for 18 bar tests

6.4.5 Simulation results: strain rate of the experiments

Once the model is validated, some simulated results that cannot be obtained experimentally can be observed. In this case, the strain rate of the experiments was analyzed. In the Figure 6.22, Figure 6.23 and Figure 6.24 can be seen model generated strain rate vs. process time curves. These figures show that there was no constant strain rate goal achieved.

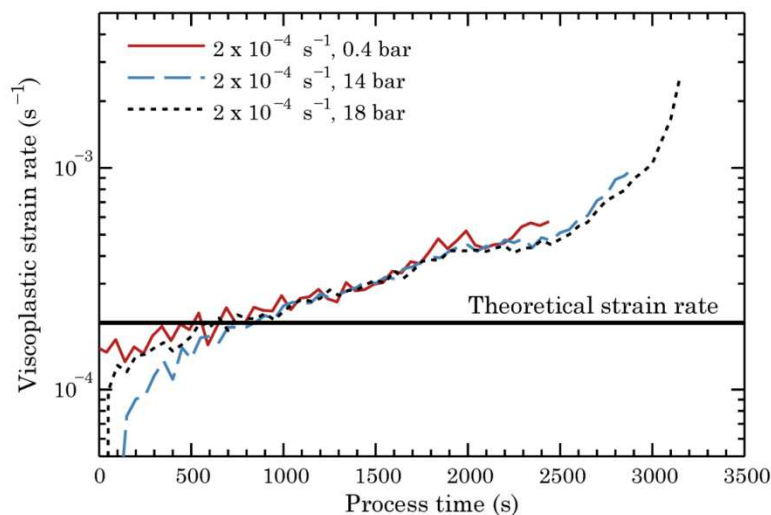


Figure 6.22.: Numerically obtained “true” strain rate values for theoretical $2 \times 10^{-4} \text{ s}^{-1}$ strain value in the pole of the dome.

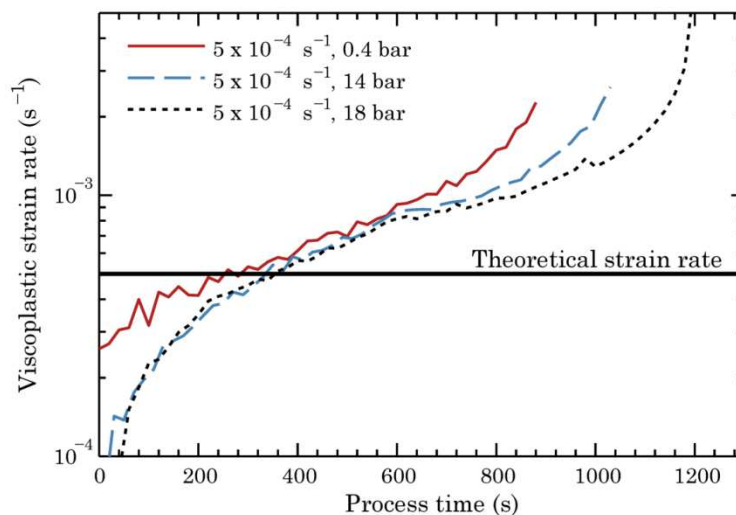


Figure 6.23.: Numerically obtained “true” strain rate values for theoretical $5 \times 10^{-4} \text{ s}^{-1}$ strain value in the pole of the dome.

Anyway, the strain rate change is lower when the strain rate is higher and vice versa achieving strain rate variance around the target one.

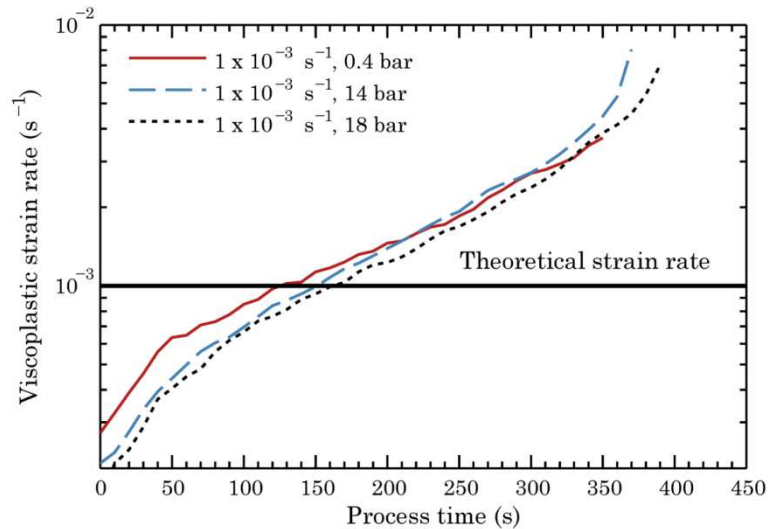


Figure 6.24.: Numerically obtained “true” strain rate values for theoretical $5 \times 10^{-4} \text{ s}^{-1}$ strain value in the pole of the dome.

6.5 New strategy validation

For investigating the applicability of the new strategy four different toroid-shape tests were formed in the SPF prototype presented before.

Experimentally, the four toroid-shape tests were:

- the first one at target constant strain rate of $2 \times 10^{-4} \text{ s}^{-1}$.
- the second at target constant strain rate of $2 \times 10^{-4} \text{ s}^{-1}$ and a backpressure of 1.8 MPa.
- the third at target constant strain rate of $6 \times 10^{-4} \text{ s}^{-1}$ and a backpressure of 1.8 MPa.
- the fourth at target variable strain rate value that follows the maximum m value curve presented before and a backpressure of 1.8 MPa.

Figure 5.22 from Chapter 5 shows the predicted pressure difference profiles that were achieved with the programmed user subroutine. The numerical results showed in this section were calculated using the experimentally measured pressure-time curves, as it was made with the bulge-test results.

6.5.1 Experimental results of toroid-shape part

The obtained experimental parts can be seen in Figure 6.25.



Figure 6.25.: Four different tests carried out at different conditions of (a) at constant strain rate of 2×10^{-4} (b) at constant strain rate of 2×10^{-4} and a backpressure of 1.8 MPa, (c) at variable strain rate value that follows the maximum m value curve presented before and a backpressure of 1.8 MPa and (d) at constant strain rate of 6×10^{-4} and a backpressure of 1.8 MPa.

As predicted by the simulations, better results are shown for the tests that employ backpressure, although this backpressure increases the frictional forces between the sheet and the die. All the experiments carried out without backpressure (only one presented here) reached the total failure of the material before the part was completely formed.

The thickness of the tests was measured using a Mitutoyo coordinate measuring machine. As can be seen in Figure 6.27, the measurement was made in a cutting section. The comparison shows that there is same localized thinning in the area of a radius of 20 mm from the centre of the part.

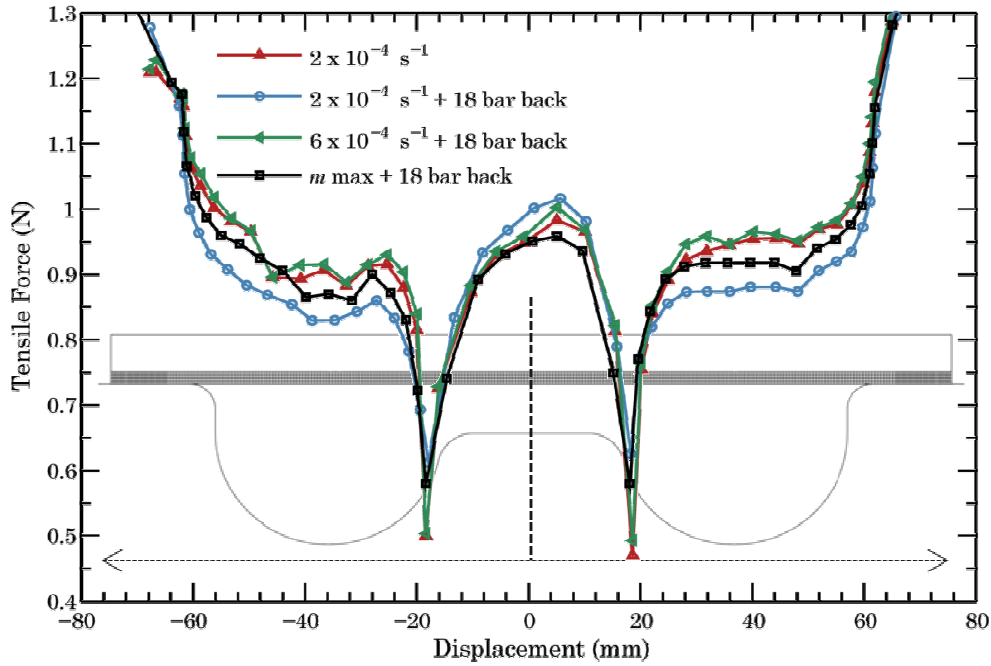


Figure 6.26.: Results of the thickness profile of the toroid-shape test for different conditions of at constant strain rate of 2×10^{-4} at constant strain rate of 2×10^{-4} and a backpressure of 1.8 MPa, 6×10^{-4} and a backpressure of 1.8 MPa and variable strain rate value that follows the maximum m value curve presented before and a backpressure of 1.8 MPa.

Furthermore, it seems to be clear that the maximum thinning appears at the $2 \times 10^{-4} \text{ s}^{-1}$ target strain rate and $6 \times 10^{-4} \text{ s}^{-1}$ target strain rate and backpressure case. On the other hand, the $2 \times 10^{-4} \text{ s}^{-1}$ target strain rate and backpressure and the maximum m value strategy and a backpressure of 1.8 MPa cases show the minimum localized thinning. Some information of the mentioned four tests is summarized in the Table 6.1. Apart from minimum thickness and thinning (minimum thickness / initial thickness), a thinning factor value appear, which is the ratio between the minimum thickness and the average thickness. Thinning factor is a parameter used to quantitatively express the level of deformation non-uniformity.

Table 6.1. Results of the four toroid-shape tests.

	$2 \times 10^{-4} \text{ s}^{-1}$	$2 \times 10^{-4} \text{ s}^{-1} + \text{back}$	$6 \times 10^{-4} \text{ s}^{-1} + \text{back}$	$m \text{ max} + \text{back}$
Fractured	Yes	No	Yes	No
Process time	3998 s	5524 s	2202 s	2601 s
Min thickness	0.47 mm	0.61 mm	0.48 mm	0.58 mm
Average thickness	0.97 mm	0.94 mm	0.97 mm	0.97 mm
Thinning	0.31	0.41	0.32	0.40
Thinning factor	0.48	0.64	0.48	0.62

Comparing the different data, the best results for thinning was the 2×10^{-4} + backpressure test. On the other hand, the thinning factor of the 2×10^{-4} + backpressure and m max + backpressure tests are very similar. In addition, the thinning factor of the 2×10^{-4} and 6×10^{-4} + backpressure tests is equal. In the first case the minimum thickness value achieved with the 2×10^{-4} + backpressure test is higher, but the average thickness is lower. On the contrary, in the second case, the minimum and average results were very similar obtaining same factor results.

It is essential to point out the process time differences, which is an important issue of this work. The first two tests were the longest, needing more than one and a half hour to finish a part at $2 \times 10^{-4} \text{ s}^{-1}$ target strain rate. Conversely, by m max approach the forming time was reduced to less than 45 minutes reducing the forming time a 50 %.

6.5.2 Numerical results and comparison with experimental data

To validate the model with die-sheet contact and more complex geometry than bulge-test, experimental and numerical data comparison of the four toroid shape tests was made. The results can be seen in the Figure 6.27, Figure 6.28, Figure 6.29 and Figure 6.30. The results show a good agreement even in the area of localized thinning.

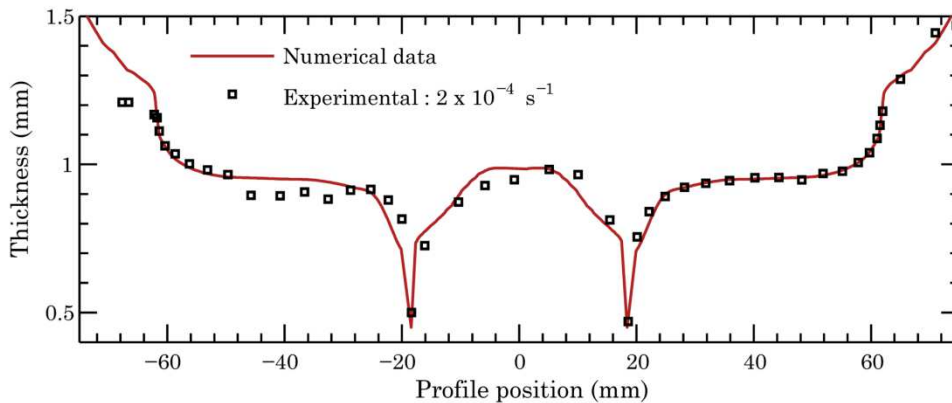


Figure 6.27.: Comparison of experimental and numerical results of the thickness profile of the toroid-shape test at target constant strain rate of $2 \times 10^{-4} \text{ s}^{-1}$.

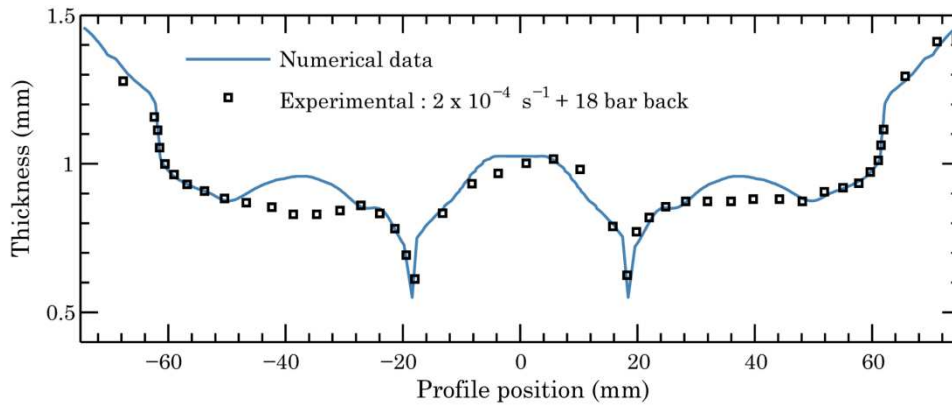


Figure 6.28.: Comparison of experimental and numerical results of the thickness profile of the toroid-shape test at target constant strain rate of $2 \times 10^{-4} \text{ s}^{-1}$ and backpressure of 18 bar.

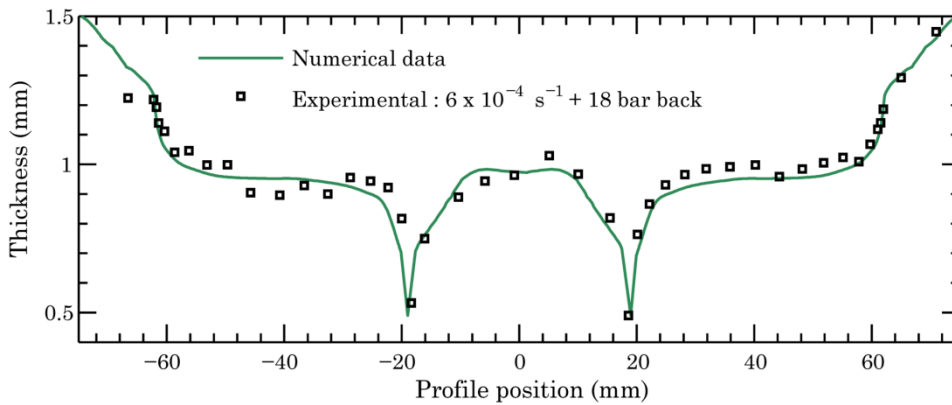


Figure 6.29.: Comparison of experimental and numerical results of the thickness profile of the toroid-shape test at target constant strain rate of $6 \times 10^{-4} \text{ s}^{-1}$ and backpressure of 18 bar.

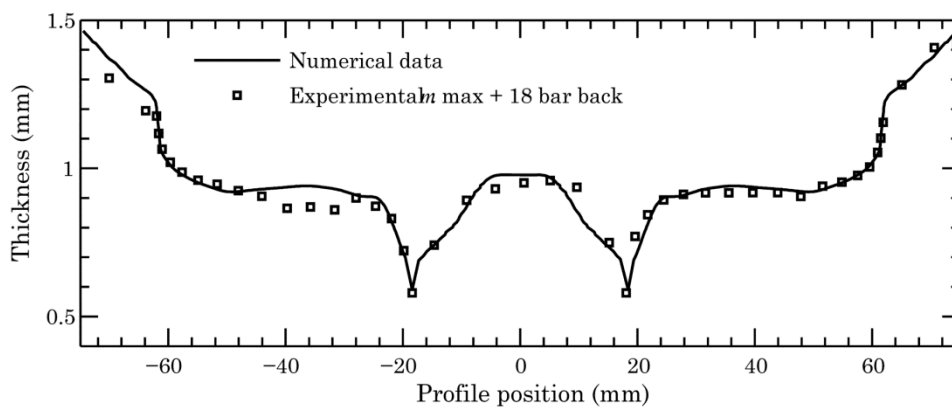


Figure 6.30.: Comparison of experimental and numerical results of the thickness profile of the toroid-shape test at target constant strain rate of maximum m strategy and backpressure of 18 bar.

To conclude, it has been shown that this strategy allows the achieving of toroid-shape parts for less forming time and similar thickness profiles.

6.6 Closure

A SPF facility was developed and manufactured to be able to form SPF titanium and aluminium alloys. This facility was designed to undergo temperatures up to 950 °C, being the heat insulation and the expansion the mayor temperature issues to tackle. In addition, a double inlet gas pressure facilities were adjusted to have backpressure capabilities for the materials that suffer from cavitation. The facility fulfilled the necessities to form Al-5083-SPF parts at target strain rates in the range of $2 \times 10^{-4} \text{ s}^{-1}$ and $1 \times 10^{-3} \text{ s}^{-1}$ with different backpressures.

Additionally, different bulge-test s at several target strain rate, backpressure and strain values were conducted. These tests showed there is a consistency between the tendencies extracted from bibliographical information and experimental ones.

Moreover, the bulge-test experimental results were compared to numerical ones, showing a good agreement in height and thickness in the pole of the dome of the parts for different strain values. In contrast, the cavitation behaviour and grain growth results do not show as good consistency, which may be due to a non-accurate measurement of the microstructural results. In addition, it must be highlighted that the concordance of the results is not very good when the total damage of the material is achieved. Anyway, it must be remembered that the constitutive equations and cavitation behaviour equations shown in Chapter 4 are not for describing the fracture of the material, only the first stages of the damage.

Using the same methodology, toroid-shape tests were conducted at different strategies and backpressure values. The comparison of the thickness profiles of the experimental and numerical results show the validity of the implemented SPF numerical model when contact between the sheet and the die is involved.

Furthermore, the experimental thickness profile results of toroid-shape geometry and the process time of each strategy validate the maximum m strategy presented in Chapter 5 for time optimization without losing quality of the part.

CONCLUSION AND FUTURE WORK

6.7 Conclusions

This section describes the conclusions of this research. The main objective of this work was to acquire knowledge on the superplasticity and superplastic forming of aluminium alloys, in order to optimize process-forming times and final parts characteristics for complex geometries. Five mayor stages to achieve this goal are distinguished:

Material characterization: Due to its great potential for weight savings in the transportation sector of applications, superplastic aluminium alloys were the main target material of this study. The Al-5083-SPF aluminium alloy was the focus in particular, where its superplastic behaviour was first characterised over a range of temperatures and strain rates using controlled constant strain rate tensile and strain rate jump tests. The results related the material's mechanical behaviour in terms of flow stress and strain rate sensitivity on one side, and microstructural parameters in terms of grain size and cavitation on the other side. The most remarkable conclusions are:

- The optimum testing temperature was found to be 500 ° C and the optimum controlled strain rate $2 \times 10^{-4} \text{ s}^{-1}$.
- At 500 °C and in the range between $2 \times 10^{-4} \text{ s}^{-1}$ $2 \times 10^{-3} \text{ s}^{-1}$ the strain rate sensitivity value is around 0.5.
- Increasing the controlled strain rate, the average grain size is higher for the same strain values.
- The cavitation area fraction increases increasing the controlled strain rate and strain.
- The specimen geometry showed to be significant for accurate superplastic uniaxial characterization.

Material modelling: A multiaxial constitutive model, based on the continuum theory of viscoplasticity, was developed to describe the behaviour of superplastic materials. The model describes a volumetric strain rate due to cavitations behaviour, accounts for internal variables and microstructural evolution, including grain growth and cavitation. Furthermore, the model is sensitive to the loading state of the material, being able to reproduce the benefits due to the use of backpressure technique. Using an inverse analysis technique, the model parameters were fitted to the characterized data, obtaining a precise superplastic damage behaviour equation for the material. In summary, the contributions of this study to the accurate constitutive models for SPF are:

- Modified Dunne's mechanism-base hyperbolic sine constitutive equations was shown to have the ability of describing a wide range of strain rates precisely, even when the cavitational damage is present.
- The continuCDM was demonstrated to be a valid method to describe the damage behaviour in superplastic materials.
- The constitutive model parameters were first calibrated for the Al-5083-SPF aluminium alloy using the results of mechanical testing, combined with additional microstructural examination in terms of grain growth and cavitation.
- The uniaxial tests geometrical and microstructural changes showed that can lead to an imprecise material characterization.
- The inverse analysis technique is essential tool to determine the accurate constitutive equations parameters when the damage behaviour of superplastic materials is described if there is no real, in situ strain determination procedure.

Process model implementation: A multiaxial SPF process model was implemented in order to simulate the tensile tests and the gas forming process using the aforementioned material constitutive equations. To optimize the process, different control strategies were implemented using user-subroutines. A new approach was presented to tackle the problems related to high forming times in superplastic forming operations through optimization. The calibrated model for the Al-5083-SPF aluminium alloy was combined with maximum strain rate strategy approach to generate the appropriate optimum loading path for the material.

- The effect of the use of backpressure is shown to have a significant influence in the numerical results.
- Smoothed volume control showed to be able to converge in valid pressure-time curves when damage started within the material.
- Experimental validation of the proposed optimization scheme was carried out by a semi industrial geometry and the results indicated significant reduction in

forming time without sacrificing the integrity and thickness uniformity of the part.

Gas forming experiments: The capabilities of the model were tested using a specially built bulge forming setup, by forming Al-5083-SPF aluminium alloy sheets into different shapes, based on pressure-time. The tests were carried out at different target strain rates, backpressure values, strain values and control strategies.

- The model was shown to have the ability to capture the behaviour of the material in all the cases to a very good extent, although a better analysis in the last stages of the damage behaviour is required from 5% cavitation value to total collapse of the material.
- The effect of the backpressure was proven to be effective to tackle the cavitation damage evolution.
- The combination of the maximum m strategy and backpressure have shown capabilities of significant reduction in forming time without sacrificing the integrity and thickness uniformity of the part in real geometrical part.

6.8 Future work

The present dissertation has demonstrated that using accurate constitutive models SPF forming times can be reduced optimally. However, further research work is suggested in order to complete the understanding of the process and improve the optimization of SPF.

A wider mechanical characterization of the material at different temperatures and controlled strain rates is suggested, in order to characterize the material more accurately and to obtain more precise constitutive equation parameters. This is interesting to study the extent of the capabilities of the Dunne's mechanism-based constitutive equations. Furthermore, the improvement of the mechanical data and the parameter determination will influence the maximum m strategies effectiveness.

A comprehensive understanding of the cavitation behaviour of the material in different loading conditions could be a key for a more accurate representation of the material behaviour in numerical models. The non-homogeneity of the voids distribution is likely to be the reason of limitation of the validity of equations used in this work to 5 % of cavitation area fraction.

The use of dedicated superplastic deformation cavitation evolution equations is determined to be interesting, since the theoretical equation used in this work are based in creep behaviour cavitation. As it was pointed out by Bae and Gosh [Bae01b] the cavity growth estimated for superplastic materials generally underestimates the actual one. In the

case of Al-5083-SPF, the cavity growth begins by matrix-particle debonding at grain boundaries and from preexisting voids, so the cavity distribution is different for creep and superplastic behaviours.

Furthermore, a failure model could be implemented in the numerical models, in order to have a reference of material total collapse prediction. This is not as important from an industrial point of view, but it is to have a better understanding of the cavitation behaviour. In this understanding should be include the behaviour of the voids when the material is at compression state. This would be interesting to investigate if it is possible to decrease the void volume fraction when the sheet is compressed against the die, as the cavitation behaviour equations presented in this work suggest.

A tribological analysis is likely to develop, as it is an important issue for the process optimization, and can have important effects depending on the die material. An analysis of the effect of the backpressure in the final thickness distribution is interesting too, as the thickness distribution of the sheet during the process could be controlled by changing the frictional force.

Regarding the experimental work, wider test variation is suggested. This variation could be accomplished in terms of part geometry, temperature, strain rate, higher than 18 bar backpressure etc. Different geometries are interesting to ensure the validity of the maximum m approach to other geometries.

PUBLISHED WORK AND OTHER SUBMISSIONS

Within the present thesis, different contributions in national and international scientific congresses and publications in international journals were presented:

International journals

[Ote12c] Otegi, N., Galdos, L., Hurtado, I., & Leen, S. (2012). Comparison study of two constitutive equations for Al-5083 superplastic aluminium alloy. *Materialwissenschaft Und Werkstofftechnik*, 43(9), 780-785.

[Ote12b] Otegi, N., Galdos, L., & Hurtado, I. (2012) Optimization of superplastic forming of aluminium Al-5083 alloy based on a Mechanism-Based hyperbolic equation. *Steel Research International*, special issue, 900-904.

International congresses

Esaform 2012 conference, Belfast: Otegi, N., Galdos, L., Hurtado, I., & Leen, S. (2011). Analysis of the capabilities of a hyperbolic constitutive equation for Al-5083 superplastic aluminium alloy. *AIP Conference Proceedings*, 1353. pp. 1574. [Ote11a]

Iddrg 2012 conference, Bilbao: Otegi, N., Galdos, L., & Hurtado, I. (2011). Optimization of superplastic forming of aluminium 5083Alloy based on a multiscale failure criterion. In proceeding of IDDRG 2011. [Ote11b]

Hydroforming of Sheets, Tubes and Profiles, Stuttgart: Galdos L., Otegi, N. & Saenz de Argandona E. (2012). Optimisation of superplastic forming of aluminium al- 5083 alloy based on a Mechanism-Based hyperbolic equation. In proceeding of Hydroforming of Sheets, Tubes and Profiles 2012. [Gal12]

Icsam 2012 conference, Albi: Otegi, N., Galdos, L., Hurtado, I., & Leen, S. (2013). New strategy for the prediction of the gas pressure profile of superplastic forming of al-5083 aluminium alloy. *Materials Science Forum*, 735(2013), 204-209. [Ote2013]

National congresses

MZT 2012, Arrasate-Mondragon: Otegi, N., Galdos, L., & Hurtado, I. (2012). Kabitazioa jasaten dute material superplastikoen deskribapena ekuazio hiperbolikoen bitartez. In *proceedings of Materialen Zientzia eta Teknologiaren I. Kongresua*. [Ote12a]

REFERENCES

- [Aba08] Simulia.(2008). ABAQUS V6.9 Documentation.
- [Ara12] <http://www.artnet.com/Magazine/reviews/manson/manson5-25-05.asp>. (2012).
- [Ash73] Ashby, M., & Verrall, R. (1973). Diffusion-accommodated flow and superplasticity. *Acta Metallurgica*, 21(2), 149-163.
- [Ast03] ASTM E21 – 03. (2003). Standard Test Methods for Elevated Temperature Tension Tests of Metallic Materials.
- [Ast06] ASTM E2448 - 06. (2006). Standard Test Method for Determining the Superplastic Properties of Metallic Sheet Materials
- [Ave66] Avery, D., & Backofen, W. (1966). A structural basis for superplasticity. *ASM Trans Quart*, 59(2), 356-359.
- [Bac64] Backofen, W., Turner, I., & Avery, D. (1964). Superplasticity in an al-zn alloy. *Transactions of the ASM*, 57, 980-990.
- [Bae00] Bae, D., & Ghosh, A. (2000). Grain size and temperature dependence of superplastic deformation in an Al-Mg alloy under isostructural condition. *Acta Materialia*, 48(6), 1207-1224.
- [Bae02a] Bae, D., & Ghosh, A. (2002). Cavity growth during superplastic flow in an Al-Mg alloy: I. experimental study. *Acta Materialia*, 50(5), 993-1009.
- [Bae02b] Bae, D., & Ghosh, A. (2002). Cavity growth in a superplastic Al-Mg alloy: II. an improved plasticity based model. *Acta Materialia*, 50(5), 1011-1029.

[Bam83] Bampton, C., Mahoney, M., Hamilton, C., Ghosh, A., & Raj, R. (1983). Control of superplastic cavitation by hydrostatic pressure. *Metallurgical and Materials Transactions A*, 14(8), 1583-1591.

[Ban05] Banabic, D., Vulcan, M., & Siegert, K. (2005). Bulge-test ing under constant and variable strain rates of superplastic aluminium alloys. *CIRP Annals-Manufacturing Technology*, 54(1), 205-208.

[Bar99] Barnes, A. (1999). Superplastic aluminum forming-expanding its techno-economic niche. *Materials Science Forum*, , 304. pp. 785-796.

[Bar07] Barnes, A. J. (2007). Superplastic forming 40 years and still growing. *Journal of Materials Engineering and Performance*, 16(4), 440-454.

[Bee78] Beere, W., & Rutter, E. (1978). Stresses and deformation at grain boundaries [and discussion]. *Philosophical Transactions of the Royal Society of London. Series A, Mathematical and Physical Sciences*, 288(1350), 177-196.

[Bon90] Bonet, J., Wood, R., & Wargadipura, A. (1990). Numerical simulation of the superplastic forming of thin sheet components using the finite element method. *International Journal for Numerical Methods in Engineering*, 30(8), 1719-1737.

[Cha02] Chandra, N. (2002). Constitutive behavior of superplastic materials. *International Journal of Non-Linear Mechanics*, 37(3), 461-484.

[Cha05] Chandra, N., Khraisheh, M. K., & Kalu, P. N. (2005). Effect of state of stress on the cavitation behavior of al 5083 superplastic material. *Materials Science Forum*, , 475. pp. 2931-2936.

[Che96] Chen, Z., & Thomson, P. (1996). Friction against superplastic aluminium alloys. *Wear*, 201(1), 227-232.

[Che04] Chen, Z., & Thomson, P. (2004). A study of post-form static and fatigue properties of superplastic 7475-SPF and 5083-SPF aluminium alloys. *Journal of Materials Processing Technology*, 148(2), 204-219.

[Che05] Chezán, A., & De Hosson, J. T. M. (2005). Superplastic behavior of coarse-grained aluminum alloys. *Materials Science and Engineering: A*, 410, 120-123.

- [Cho86] Chokshi, A. H. (1986). The development of cavity growth maps for superplastic materials. *Journal of Materials Science*, 21(6), 2073-2082.
- [Cho93] Chokshi, A. H., & Mukherjee, A. K. (1993). The influence of hydrostatic pressure on grain boundary sliding in superplasticity: Implications for cavitation. *Materials Science and Engineering: A*, 171(1), 47-54.
- [Coc80] Cocks, A., & Ashby, M. (1980). Intergranular fracture during power-law creep under multiaxial stresses. *Metal Science*, 14(8-9), 8-9.
- [Coc82] Cocks, A., & Ashby, M. (1982). On creep fracture by void growth. *Progress in Materials Science*, 27(3), 189-244.
- [Col95] Cole, G., & Sherman, A. (1995). Light weight materials for automotive applications. *Materials Characterization*, 35(1), 3-9.
- [Cur01] Curtis, R., Garriga-Majo, D., Juszczak, A., Soo, S., Pagliaria, D., & Walter, J. (2001). Dental implant superstructures by superplastic forming. *Materials Science Forum*, , 357. pp. 47-52.
- [Din95] Ding, X., Zbib, H., Hamilton, C., & Bayoumi, A. (1995). On the optimization of superplastic blow-forming processes. *Journal of Materials Engineering and Performance*, 4(4), 474-485.
- [Din97] Ding, X., Zbib, H., Hamilton, C., & Bayoumi, A. (1997). On the stability of biaxial stretching with application to the optimization of superplastic blow-forming. *Journal of Engineering Materials and Technology*, 119(1), 26-31.
- [Dru57] Drucker, D. C. (1957). A definition of stable inelastic material.
- [Fur12] <http://www.furukawa-sky.co.jp/english/products/processed/alnovi.htm>, 2012
- [Gal12] Galdos L., Otegi, N. & Saenz de Argandona E. (2012). Optimisation of superplastic forming of aluminium al- 5083 alloy based on a Mechanism-Based hyperbolic equation. In proceeding of Hydroforming of Sheets, Tubes and Profiles 2012.
- [Gre72] Green, R. (1972). A plasticity theory for porous solids. *International Journal of Mechanical Sciences*, 14(4), 215-224.

[Gur75] Gurson, A. (1975). Plastic flow and fracture behavior of ductile materials incorporating void nucleation, growth and coalescence. PhD Diss, Brown University,

[Ham01] Hambli, R., & Potiron, A. (2001). Comparison between 2D and 3D numerical modeling of superplastic forming processes. *Computer Methods in Applied Mechanics and Engineering*, 190(37), 4871-4880.

[Har67] Hart, E. (1967). Theory of the tensile test. *Acta Metallurgica*, 15(2), 351-355.

[Hoj08] Hojjati, M., Zoorabadi, M., & Hosseinipour, S. (2008). Optimization of superplastic hydroforming process of aluminium alloy 5083. *Journal of Materials Processing Technology*, 205(1), 482-488.

[Iso07] BS ISO 20032:2007. (2007). Method for evaluation of tensile properties of metallic superplastic materials

[Jai91] Jain, M., Chaturvedi, M., Richards, N., & Goel, N. (1991). Strain rate sensitivity effects with forming characteristics of superplastic Ti-6Al-4V. *Materials Science and Engineering: A*, 138(2), 205-211.

[Jam97] Jambor, A., & Beyer, M. (1997). New cars: new materials. *Materials & Design*, 18(4), 203-209.

[Jar10] Jarrar, F. S., Hector Jr, L. G., Khraisheh, M. K., & Bower, A. F. (2010). New approach to gas pressure profile prediction for high temperature AA5083 sheet forming. *Journal of Materials Processing Technology*, 210(6), 825-834.

[Jis02] JIS H7501:2002. (2002). Method for evaluation of tensile properties of metallic superplastic materials

[Kai02] Kaibyshev, O. A. (2002). Fundamental aspects of superplastic deformation. *Materials Science and Engineering: A*, 324(1), 96-102.

[Kel04] Kelly, R., Leen, S. B., Pashby, I., & Kennedy, A. R. (2004). The measurement of friction for superplastic forming of ti-6Al-4V. *Materials Science Forum*, , 447. pp. 111-116.

[Kha96] Khaleel, M., Johnson, K., Lavender, C., Smith, M., & Hamilton, C. (1996). Specimen geometry effect on the accuracy of constitutive relations in a superplastic 5083 aluminum alloy. *Scripta Materialia*, 34(9)

- [Kha98] Khaleel, M., Johnson, K., Hamilton, C., & Smith, M. (1998). Deformation modeling of superplastic AA-5083. *International Journal of Plasticity*, 14(10), 1133-1154.
- [Kha01] Khaleel, M., Zbib, H., & Nyberg, E. (2001). Constitutive modeling of deformation and damage in superplastic materials. *International Journal of Plasticity*, 17(3), 277-296.
- [Khr06] Khraisheh, M., Abu-Farha, F., Nazzal, M., & Weinmann, K. (2006). Combined mechanics-materials based optimization of superplastic forming of magnesium AZ31 alloy. *CIRP Annals-Manufacturing Technology*, 55(1), 233-236.
- [Kim01] Kim, B. N., Hiraga, K., Morita, K., & Sakka, Y. (2001). A high-strain-rate superplastic ceramic. *Nature*, 413(6853), 288-291.
- [Kim97] Kim, T., & Dunne, F. (1997). Determination of superplastic constitutive equations and strain rate sensitivities for aerospace alloys. *Proceedings of the Institution of Mechanical Engineers, Part G: Journal of Aerospace Engineering*, 211(6), 367.
- [Kra04] Krallics, G., & Lenard, J. (2004). An examination of the accumulative roll-bonding process. *Journal of Materials Processing Technology*, 152(2), 154-161.
- [Kul05] Kulas, M. A., Green, W. P., Taleff, E. M., Krajewski, P. E., & McNelley, T. R. (2005). Deformation mechanisms in superplastic AA5083 materials. *Metallurgical and Materials Transactions A*, 36(5), 1249-1261.
- [Kul06] Kulas, M. A., Green, W. P., Taleff, E. M., Krajewski, P. E., & McNelley, T. R. (2006). Failure mechanisms in superplastic AA5083 materials. *Metallurgical and Materials Transactions A*, 37(3), 645-655.
- [Lan02] Langdon, T. G. (2002). Creep at low stresses: An evaluation of diffusion creep and harper-dorn creep as viable creep mechanisms. *Metallurgical and Materials Transactions A*, 33(2), 249-259.
- [Lem05] Lemaitre, J., & Desmorat, R. (2005). *Engineering damage mechanics: Ductile, creep, fatigue and brittle failures* Springer.
- [Li,04] Li, G., Tan, M., & Liew, K. (2004). Three-dimensional modeling and simulation of superplastic forming. *Journal of Materials Processing Technology*, 150(1), 76-83.

[Lin01] Lin, J., & Dunne, F. (2001). Modelling grain growth evolution and necking in superplastic blow-forming. *International Journal of Mechanical Sciences*, 43(3), 595-609.

[Lin02] Lin, J., Cheong, B., & Yao, X. (2002). Universal multi-objective function for optimising superplastic-damage constitutive equations. *Journal of Materials Processing Technology*, 125, 199-205.

[Lin05] Lin, J., & Dean, T. (2005). Modelling of microstructure evolution in hot forming using unified constitutive equations. *Journal of Materials Processing Technology*, 167(2), 354-362.

[Luc04] Luckey, S., & Friedman, P. (2004). Aspects of element formulation and strain rate control in the numerical modeling of superplastic forming. *Advances in Superplasticity and Superplastic Forming as Held at the 2004 TMS Annual Meeting*, pp. 371-380.

[Mar10] MSC. (2010). Marc documentation. V. 2010.

[Mer10] Mercedes-Benz. (2010). <http://www.mercedes-amg.com/>

[Moh01] Mohamed, F. A. (2001). The role of boundaries during superplastic deformation. *Surface and Interface Analysis*, 31(7), 532-546.

[Moh02] Mohamed, F. A. (2002). The role of impurities during creep and superplasticity at very low stresses. *Metallurgical and Materials Transactions A*, 33(2), 261-278.

[Naz04] Nazzal, M. A., Khraisheh, M. K., & Darras, B. M. (2004). Finite element modeling and optimization of superplastic forming using variable strain rate approach. *Journal of Materials Engineering and Performance*, 13(6), 691-699.

[Nie05] Nieh, T., Wadsworth, J., & Sherby, O. D. (2005). *Superplasticity in metals and ceramics* Cambridge University Press.

[Osa97] Osada, K. (1997). Commercial applications of superplastic forming. *Journal of Materials Processing Technology*, 68(3), 241-245.

[Ote11a] Otegi, N., Galdos, L., Hurtado, I., & Leen, S. (2011). Analysis of the capabilities of a hyperbolic constitutive equation for Al-5083 superplastic aluminium alloy. *AIP Conference Proceedings*, 1353. pp. 1574.

[Ote11b] Otegi, N., Galdos, L., & Hurtado, I. (2011). Optimization of superplastic forming of aluminium 5083Alloy based on a multiscale failure criterion. In proceeding of IDDRG 2011

[Ote12a] Otegi, N., Galdos, L., & Hurtado, I. (2012). Kabitazioa jasaten dute material superplastikoen deskribapena ekuazio hiperbolikoen bitartez. In proceedings of Materialen Zientzia eta Teknologiaren I. Kongresua.

[Ote12b] Otegi, N., Galdos, L., & Hurtado, I. (2012) Optimization of superplastic forming of aluminium Al-5083 alloy based on a Mechanism-Based hyperbolic equation. Steel Research International, special issue, 900-904

[Ote12c] Otegi, N., Galdos, L., Hurtado, I., & Leen, S. (2012). Comparison study of two constitutive equations for Al-5083 superplastic aluminium alloy. Materialwissenschaft Und Werkstofftechnik, 43(9), 780-785.

[Ote13] Otegi, N., Galdos, L., Hurtado, I., & Leen, S. (2013). New strategy for the prediction of the gas pressure profile of superplastic forming of al-5083 aluminium alloy. Materials Science Forum, 735(2013), 204-209.

[Pac67] Packer, C. M., & Sherby, O. D. (1967). An interpretation of the superplasticity phenomenon in two-phase alloys. ASM Trans Quart, 60(1), 21-28.

[Pad01] Padmanabhan, K. A., Vasin, R., & Enikeev, F. (2001). Superplastic flow: Phenomenology and mechanics Springer.

[Pan09] Panicker, R., Chokshi, A., Mishra, R., Verma, R., & Krajewski, P. (2009). Microstructural evolution and grain boundary sliding in a superplastic magnesium AZ31 alloy. Acta Materialia, 57(13), 3683-3693.

[Pea34] Pearson, C. (1934). The viscous properties of extruded eutectic alloys of lead-tin and bismuth-tin. J.Inst.Metals, 54(1), 111-124.

[Per84] Perzyna, P. (1984). Constitutive modeling of dissipative solids for postcritical behavior and fracture. J.Eng.Mater.Technol.(Trans.ASME), 106(4), 410-419.

[Pil85] Pilling, J. (1985). Effect of coalescence on cavity growth during superplastic deformation. Materials Science and Technology, 1(6), 461-465.

[Pil91] Pilling, J. (1991). Cavitation and cavity suppression during multiaxial deformation of superplastic materials. *Superplasticity in Advanced Materials*, , 181-190.

[Pil86] Pilling, J., & Ridley, N. (1986). Effect of hydrostatic pressure on cavitation in superplastic aluminium alloys. *Acta Metallurgica*, 34(4), 669-679.

[Pil89] Pilling, J., & Ridley, N. (1989). Superplasticity in crystalline solids.

[Pye81] Pye, A. (1981). Superplastic forming of aluminium alloys. *Materials & Design*, 2(6), 304-309.

[Reg98] Regenauer-Lieb, K. (1998). Dilatant plasticity applied to alpine collision: Ductile void growth in the intraplate area beneath the eifel volcanic field. *Journal of Geodynamics*, 27(1), 1-21.

[Ric69] Rice, J., & Tracey, D. M. (1969). On the ductile enlargement of voids in triaxial stress fields—*Journal of the Mechanics and Physics of Solids*, 17(3), 201-217.

[Rid05] Ridley, N., Bate, P., & Zhang, B. (2005). Material modelling data for superplastic forming optimisation. *Materials Science and Engineering: A*, 410, 100-104.

[Rou87] Rousselier, G. (1987). Ductile fracture models and their potential in local approach of fracture. *Nuclear Engineering and Design*, 105(1), 97-111.

[Rua88] Ruano, O., & Sherby, O. (1988). On constitutive equations for various diffusion-controlled creep mechanisms. *Revue De Physique Appliquée*, 23(4), 625-637.

[Sal01] Salishchev, G., Galejev, R., Valiakhmetov, O., Safiullin, R., Lutfullin, R. Y., Senkov, O., et al. (2001). Development of Ti-6Al-4V sheet with low temperature superplastic properties. *Journal of Materials Processing Technology*, 116(2), 265-268.

[Sal03] Salvo, L., Cloetens, P., Maire, E., Zabler, S., Blandin, J., Buffière, J. Y., et al. (2003). X-ray micro-tomography an attractive characterisation technique in materials science. *Nuclear Instruments and Methods in Physics Research Section B: Beam Interactions with Materials and Atoms*, 200, 273-286.

[San99] Sanders, D. (1999). Superplastic forming manufacturing technology moves towards the twenty-first century. *Materials Science Forum*, , 304. pp. 805-812.

- [San01] Sanders, D. (2001). The current state-of-the-art and the future in airframe manufacturing using superplastic forming technologies. *Materials Science Forum*, , 357. pp. 17-22.
- [Sem98] Semiatin, S., Seetharaman, V., Ghosh, A., Shell, E., Simon, M., & Fagin, P. (1998). Cavitation during hot tension testing of Ti-6Al-4V. *Materials Science and Engineering: A*, 256(1), 92-110.
- [Shi76] Shima, S., & Oyane, M. (1976). Plasticity theory for porous metals. *International Journal of Mechanical Sciences*, 18(6), 285-291.
- [Sni10] Snippe, Q., & Meinders, T. (2010). Mechanical experiments on the superplastic material ALNOVI-1, including leak information. *Materials Science and Engineering: A*, 528(3), 950-960.
- [Sni11] Snippe, Q. H. C. (2011). Design and optimization of vertex detector foils by superplastic forming University of Twente.
- [Soe06] Soer, W., Chezan, A., & De Hosson, J. T. M. (2006). Deformation and reconstruction mechanisms in coarse-grained superplastic Al-Mg alloys. *Acta Materialia*, 54(14), 3827-3833.
- [Sto01] Stolyarov, V. V., Zhu, Y. T., Alexandrov, I. V., Lowe, T. C., & Valiev, R. Z. (2001). Influence of ECAP routes on the microstructure and properties of pure ti. *Materials Science and Engineering: A*, 299(1), 59-67.
- [Sto83] Stowell, M. (1983). Failure of superplastic alloys. *Metal Science*, 17(1), 1-11.
- [Sto84] Stowell, M., Livesey, D., & Ridley, N. (1984). Cavity coalescence in superplastic deformation. *Acta Metallurgica*, 32(1), 35-42.
- [Sup10] <http://www.superform-aluminium.com/>. (2010).
- [Usp95] Gas control for superplastic forming, US Patent No: 5,419,170. (1995).
- [Val83] Valiev, R., & Kaibyshev, O. (1983). On the quantitative evaluation of superplastic flow mechanisms. *Acta Metallurgica*, 31(12), 2121-2128.

[Ver96] Verma, R., Friedman, P., Ghosh, A., Kim, S., & Kim, C. (1996). Characterization of superplastic deformation behavior of a fine grain 5083 al alloy sheet. *Metallurgical and Materials Transactions A*, 27(7), 1889-1898.

[Ver95] Verma, R., Ghosh, A., Kim, S., & Kim, C. (1995). Grain refinement and superplasticity in 5083 al. *Materials Science and Engineering: A*, 191(1), 143-150.

[Wat02] Watanabe, H., Mukai, T., Ishikawa, K., & Higashi, K. (2002). Low temperature superplasticity of a fine-grained ZK60 magnesium alloy processed by equal-channel-angular extrusion. *Scripta Materialia*, 46(12), 851-856.

[Woo96] Wood, R. D., & Bonet, J. (1996). Review of the numerical analysis of superplastic forming. *Journal of Materials Processing Technology*, 60(1-4), 45-53.

[Zho96] Zhou, M., & Dunne, F. P. E. (1996). Mechanisms-based constitutive equations for the superplastic behaviour of a titanium alloy. *The Journal of Strain Analysis for Engineering Design*, 31(3), 187-196.

[Zhu00] Zhu, Y. T., & Lowe, T. C. (2000). Observations and issues on mechanisms of grain refinement during ECAP process. *Materials Science and Engineering: A*, 291(1), 46-53.